University of Birmingham

School of Biosciences

Investigating the Synthetic Lethal Effects of Poly (ADP-Ribose) Polymerase and Histone Deacetylase Inhibition in Progressive B-Cell Chronic Lymphocytic Leukaemia Deficient in the ATM Pathway

and

Optimisation of Multiple Marker Imaging of Immunological Tissue Using Confocal Laser Scanning Fluorescence Microscopy

A research project report submitted by

David Michael Cartwright

as part of the requirement for the

degree of MRes in Molecular and Cellular Biology

Prologue

This document contains two separate six-month research projects completed for the degree of MRes in Molecular and Cellular Biology. The first project was concerned with the development of targeted therapies for progressive, treatment-resistant forms of B-cell chronic lymphocytic leukaemia (B-CLL) that exhibit functional loss of the Ataxia-telangiectasia mutated (ATM) gene. B-CLL is currently incurable, and available palliative treatments are relatively toxic to patients, the majority of which fall within an aging demographic. ATM loss is linked to highly aggressive forms, and results in defective homologous recombination and therefore a diminished capacity for the efficient repair of DNA double-strand breaks. While this promotes genomic instability and ultimately cancer, it also leaves the cell vulnerable to the accumulation of catastrophic DNA damage levels if other routes of DNA repair are inhibited. The aim of the project was to therefore investigate the effectiveness of novel, less toxic therapeutic compounds that exploit this mechanism of synthetic lethality - specifically, poly (ADP-ribose) polymerase and histone deacetylase inhibitors.

The second project report details an optimisation study contributing to the development of a histopathological tissue imaging method. The method utilises indirect immunofluorescence and confocal laser-scanning microscopy (CLSM) to enable the simultaneous visualisation of multiple biomarkers within tissue cryosections. The development of such a method is beneficial to histology and histopathology, as it provides a reliable method of multiple antigen visualisation, allowing for the analysis of spatial and temporal relationships between molecules, the cell types that express them and the tissue components comprised of such cells. Specifically, staining and imaging protocols were optimised for use on reactive lymph node cryosections, for the simultaneous visualisation of the B-lymphocyte surface markers CD19, κ- and λ- immunoglobulin light chain antigens. Older generation fluorophores were replaced with newer, more photostable and generally brighter Alexa fluorophores, increasing the viability and applicability of the method for both diagnostic and experimental histopathology.

The main theme running across the two projects is that of research into haematological malignancies, particularly B-CLL. Whilst the first is directly involved in the development of targeted cancer therapy, the tissue imaging method optimised in the second can be further developed for spatial immunophenotyping of specific cancer biomarkers within diseased immunological tissues. This is of use to biomedical research for the development of targeted cancer therapies based on the specific molecular mechanisms of disease, as well as from a clinical perspective for establishing disease diagnoses and prognoses based on the molecular profile of individual leukaemias and lymphatic lymphomas. The conclusions drawn from both projects will hopefully contribute towards research into haematological malignancies and benefit cancer research as a whole.

Table of Contents - Project 1

Table of Contents - Project 2

Table of Figures - Project 1

Appendix Material

Table of Figures - Project 2

Appendix Material

Acknowledgements

I would like to thank the following people for their invaluable patience and support throughout my time at the University of Birmingham, and generally making the whole experience more enjoyable:

Project 1

Angelo Agathanggelou
Gulshanara Ahmed
Ceri Oldreive
Tracey Perry
Ania Skowronska
Tania Stankovic
Victoria Weston

Project 2

Jane Birtwistle
Chris Bunce
Laura Cronin
Rachel Hayden
Farhat Khanim
Josh Rappoport
Rob Shaw

University of Birmingham

School of Biosciences

Investigating the Synthetic Lethal Effects of Poly (ADP-Ribose) Polymerase and Histone Deacetylase Inhibition in Progressive B-Cell Chronic Lymphocytic Leukaemia Deficient in the ATM Pathway

A research project report submitted by

David Michael Cartwright

as part of the requirement for the

degree of MRes in Molecular and Cellular Biology

This project was carried out at: Howell Building, University of Birmingham

Under the supervision of: Prof. Tatjana Stankovic **Date:** 11th March 2012

Abstract

Progressive B-Cell Chronic Lymphocytic Leukaemia (B-CLL) represents a clinical problem due to its aggressive disease course and poor survival rate. Many progressive B-CLL forms are characterised by a loss of the ataxia telangiectasia mutated (ATM) and/or *TP53* tumour suppressor and DNA damage repair genes, the incidence of which is associated with resistance to therapies that rely on DNA-damage induced apoptosis. The loss of these genes, particularly ATM, results in defective homologous recombination (HR). Previous studies have found that Poly (ADP-ribose) polymerase inhibitors (PARPis) impose the requirement of HR and selectively sensitise ATM deficient cells to killing. This study assessed the potential of combining histone deacetylase inhibitors (HDACis) to synergise with PARP inhibitors and increase this selective killing effect. Conversely, CII and *TP53* mutant MEC-1 isogenic B-CLL cell lines that were treated with ATM shRNA did not exhibit significant sensitivity to PARP inhibition, nor show convincing evidence of selective PARPi/HDACi synergy. *TP53* mutant cells showed no sensitivity to PARP inhibition regardless of ATM status. *TP53* mutant cells exhibited increased proliferation at low HDACi doses, although lower doses of HDAC inhibitor was more cytotoxic to p53 mutant MEC-1 cells overall, and also to ATM wild type cells in both cell lines. However, complete ATM knockdown was not achieved in CII cells and HR was not found to be seriously compromised. Thus, further detailed studies and alternative assay methods are required before any conclusions can be drawn on the synergic potential of PARP and HDAC inhibitors in the treatment of HR-deficient progressive B-CLL.

List of Abbreviations

ATM	ataxia telangiectasia mutated
ATR	ataxia telangiectasia and Rad3 related
B-CLL	B-cell chronic lymphocytic leukaemia
BER	base excision repair
CDK	cyclin dependent kinase
CI	combination index
DAPI	4',6-diamidino-2-phenylindole
DDR	DNA damage response
DMSO	dimethyl sulfoxide
DNA-PKcs	DNA - dependent protein kinase catalytic subunit
DSB	double strand break
GFP	green fluorescent protein
HAT	histone acetyltransferase
HDAC(i)	histone deacetylase (inhibitor)
HR	homologous recombination
IR	ionising radiation
KD	knockdown
NER	nucleotide excision repair
NHEJ	non-homologous end joining
PARP(i)	poly (ADP-ribose) polymerase (inhibitor)
PCR	polymerase chain reaction
PI3K	phosphatidylinositol 3-kinase
PTM	post-translational modification
ROS	reactive oxygen species
RT	room temperature
SAHA	suberoylanilide hydroxamic acid
shRNA	small hairpin RNA
SNP	single nucleotide polymorphism
SSA	single-strand annealing
SSB	single strand break
VPA	valproic acid
WT	wild type

1.0 Introduction

1.1 B-Cell Chronic Lymphocytic Leukaemia

B-Cell Chronic Lymphocytic Leukaemia (B-CLL) is the most common haematological malignancy in the Western world, with the majority of patients over 60 years of age and males outnumbering females 2:1 (Damle et al., 1999). The pathology itself is caused by the relentless accumulation of redundant monoclonal B cells that morphologically resemble small mature lymphocytes (Hamblin et al., 1999). B-CLL tumour cells have characteristic immunophenotypes, typically being positive for CD5, CD19 and CD23 markers but negative for surface CD22 and FMC7 (Hamblin et al., 1999). B-CLL tumour cells express 10-fold lower amounts of surface Ig than mature B cells, the isotypes normally being IgM or a combination of IgM and IgD. Very reduced levels of IgM are also secreted, highlighting their functional redundancy (Friedman et al., 1992). B-CLL disease progression is the most heterogeneous of all leukaemias (Cramer and Hallek, 2011). B-CLL remains at present incurable, and current treatments induce transitory remission rather than achieve total eradication of the disease (Chiorazzi et al., 2005; Damle et al., 1999). Some disease forms are relatively stable and require little or no treatment, while others are highly aggressive and have a poor clinical outcome, known as progressive CLL (Austen et al., 2007; Weston et al., 2010).

As a result of this clinical heterogeneity, there has been an emphasis on identifying unique characteristics that allow foresight of the clinical course of individual B-CLL patients. A “naive” tumour cell phenotype, characterised by unmutated IgVH genes, is a poor prognostic indicator (Damle et al., 1999; Hamblin et al., 1999), as is expression of the CD38 surface marker (Damle et al., 1999; Pittner et al., 2005). ZAP-70 is a tyrosine kinase that is exclusively expressed in T and natural killer (NK) cells, but aberrantly expressed by B cells in some forms of B-CLL, greatly reducing life expectancy and clinical outcome (Hamblin et al., 1999; Ure et al., 2009). Expression of the anti-apoptotic gene Mcl-1 may also indicate progressive B-CLL (Pepper et al., 2008). Cytogenetic abnormalities are also often present, and are also important indicators of severity. 11q and 17p deletions are indicators of very poor clinical prognosis and highly aggressive disease courses, as these are the sites of the DNA damage response and cell cycle regulator genes Ataxia telangiectasia mutated (ATM, fig. 1) and p53 respectively (Austen et al., 2005; Dohner et al., 1995; Stankovic et al., 2002b).

1.2 ATM and p53

Defective ATM expression results in progressive B-CLL because of the function and nature of the gene (fig. 1). ATM belongs to the phosphatidylinositol 3-kinase-related kinase (PIKK) superfamily, which also includes ataxia telangiectasia and RAD3-related (ATR), DNA-dependent protein kinase catalytic subunit (DNA-PKcs) and mammalian target of rapomycin (mTOR) (Zhou et al., 2006). The gene is located on chromosome 11q23-24, and its numerous roles involve cell cycle regulation, control of telomere length and DNA processing, though its main function is that of a DNA damage sensor and DNA damage response (DDR) integrator, particularly concerning DNA double-strand breaks (DSBs). The protein product is 350kDa in size, and possesses a C-terminal PI3-kinase domain. ATM phosphorylates downstream proteins to relay DNA damage signals, and recruits DNA repair proteins to sites of DNA damage (Austen et al., 2005; Lavin and Khanna, 1999; Savitsky et al., 1995; Stankovic et al., 2002a; Starczynski et al., 2003; Weston et al., 2010). Biallelic loss of the ATM gene is solely

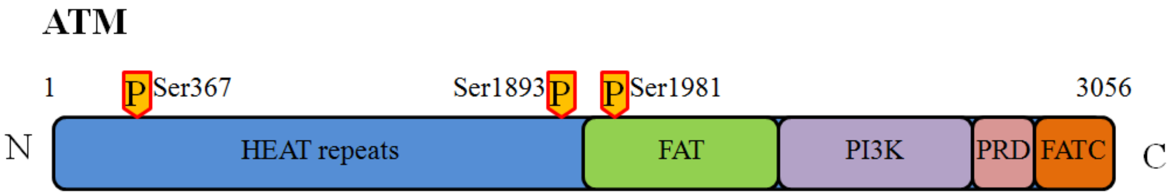

Figure 1 – Functional diagram of ATM, a 350kDa protein containing 3056 amino acids. Pictured are the five main functional domains and autophosphorylation sites. The HEAT repeats bind directly to the C terminal of NBS1, a member of the MRN DSB repair complex. The FAT domain interacts with the catalytic-site containing PI3K domain and stabilises the C-terminal region of the ATM protein, while the PRD and FATC domains regulate the kinase activity of the PI3K region.

responsible for the rare autosomal recessive inherited condition ataxia telangiectasia (A-T), the defining symptoms of which include an unsteady gait (ataxia) and visibly dilated blood vessels in the eye conjunctiva and facial region (telangiectases) (Savitsky et al., 1995; Taylor et al., 1975).

In accordance with the role of ATM in mediating the DSB response, A-T sufferers exhibit an increased sensitivity to ionising radiation (IR) and predisposition to lymphoreticular malignancies (Taylor et al., 1975). ATM-deficient cells also exhibit inherent chromosomal instability and delayed p53 activation/cell cycle arrest in response to DNA damage (Savitsky et al., 1995). This therefore explains how sporadic ATM mutations/11q deletions may promote progressive B-CLL through unrepaired DNA and subsequent chromosomal instability (Stankovic et al., 2002b). ATM is involved with the same DNA damage response pathway as p53, though the roles are not completely congruent – ATM deficiency results in increased sensitivity to IR, whilst p53 loss confers radioresistance (Alvi et al., 2005; Savitsky et al., 1995; Stankovic et al., 2002b).

1.3 Mechanisms of ATM loss

As well as 11q deleted forms of ATM-null B-CLL, ATM is the single most frequently mutated gene in B-CLL (Stankovic et al., 2002b). The reasons for why ATM dysfunction is such a common occurrence in progressive B-CLL are widely unknown. ATM is downregulated during lymphocyte germinal development and V(D)J recombination, a period during which physiological DNA DSBs must occur (Starczynski et al., 2003), although ATM dysfunction is linked with, but not exclusive to, unmutated IgVH gene disease forms (Stankovic et al., 2002b). Also, unlike A-T which is caused by the inheritance of homozygous ATM defective alleles, it is not thought that an inherited dysfunctional ATM allele bestows a predisposition to B-CLL disease onset. It is, however, likely that sporadic loss-of-function mutations will occur in the one remaining allele if B-CLL arises, and thus the possession of a defective ATM allele predisposes B-CLL patients to progressive forms of the disease (Skowronska et al., 2012). Whatever the genetic basis of ATM dysfunction, the clinical effect is certain - ATM mutations and/ or 11q deletions lead to rapid clonal expansion of ATM null tumour cells (Austen et al., 2007), thereby reducing progression-free survival rates as well as overall patient survival (Austen et al., 2007; Weston et al., 2010).

1.4 Current treatments for ATM-deficient progressive B-CLL

Commonly used progressive B-CLL treatments involve combinations of DNA-damage inducing nucleoside analogues and alkylating agents, leading to the subsequent induction of apoptosis via p53/ATM pathways (Austen et al., 2005; Austen et al., 2007; Maddocks and Lin, 2009; Pettitt, 2003). However, ATM mutant or 11qdel B-CLL forms are deficient in these pathways and thus exhibit resistance to these approaches (Weston et al., 2010). Indeed, p53 mutant B-CLL tumours exhibit little or no apoptotic response *in vitro*, whilst ATM mutant tumours exhibit a markedly reduced response (Stankovic et al., 2002b; Stankovic et al., 2004). Recently, the addition of the CD20-targeting chimeric monoclonal antibody rituximab to fludarabine and cyclophosphamide front-line regimens paired with second line alemtuzumab and flavopiridol has had some clinical success (Weston et al., 2010). A positive response to the CDK inhibitor R-roscovitine (CYC202) has also been observed, which appeared to resensitise p53/ATM pathway-deficient B-CLL tumours to DNA-damage/apoptosis inducing treatments (Alvi et al., 2005). However, these approaches still rely on traditional DNA damaging treatments and chemotherapeutics which broadly target rapidly dividing cells, resulting in clinical complications such as toxicity and immunosuppression (Weston et al., 2010). Thus, treatments are required that are not only more effective against ATM defective tumours, but also more specific to neoplastic cells and less toxic to patients, especially because most progressive B-CLL sufferers are above 60 and therefore less tolerant of adverse side effects. Because of the function of the ATM gene, a promising novel approach in treating ATM-deficient B-CLL is to exploit the concept of synthetic lethality in DNA repair pathways. To understand why this may be the case, some common mechanisms of DNA repair are introduced.

1.5 The DNA damage response, cancer and synthetic lethality as a novel therapeutic strategy

The DNA damage response (DDR) is a complex cellular process. There are five main DNA damage response mechanisms known, which can be divided into single strand break (SSB) repair and double strand break (DSB) repair. DSBs are most serious and lead to genomic and chromosomal instability, and can lead to apoptosis if left unrepaired (Shaheen et al., 2011). DSBs can be repaired via the more accurate homologous recombination (HR) mechanism, which utilises homologous chromatid sequences as templates to synthesise DNA across a DSB. HR occurs in the synthesis/gap 2/mitosis (S/G2/M) cell cycle stages. The other main DSB repair mechanism is

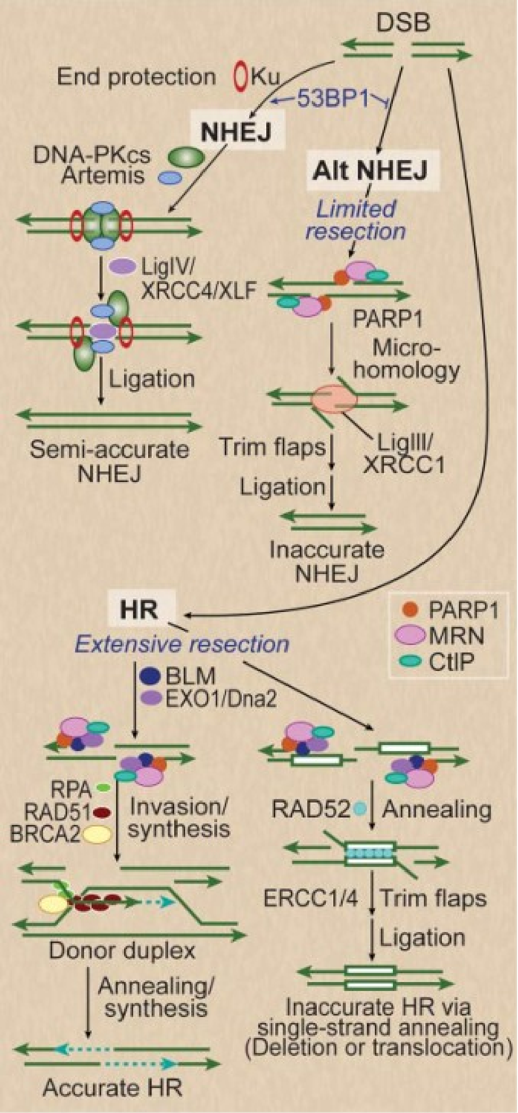

Figure 2 - DSB repair mechanisms, HR, and NHEJ, and their two sub-pathways. Some molecular mediators of each process are also pictured (Shaheen et al., 2011).

non-homologous end joining (NHEJ), which involves the direct ligation of free ends of the DSB, and is much more prone to error (Shaheen et al., 2011). NHEJ occurs in the G0-G1 phases of the cell cycle. Both of these methods have two sub-pathways (fig. 2).

The DDR is a potentially targetable mechanism for novel cancer therapeutics. The term "synthetic lethality" is defined by two genes in a relationship whereby the dysfunction of one gene is not detrimental to cell survival, but the loss of both genes simultaneously results in cell death (Helleday et al., 2008; Shaheen et al., 2011). This concept is the basis that such novel therapeutics that target the DDR are based around. Cancer itself is a disease of aberrant DNA repair mechanisms, as unrepaired DNA leads to genomic instability and subsequent malignancies (Shaheen et al., 2011). However, cancer cells still require other DNA repair mechanisms to remain functional in order for them to survive. For this reason, cancer cells that are defective in particular DNA repair mechanisms may become dependent on other still-functioning sub-pathways. By disrupting these remaining pathways via the inhibition of essential mediators, the cancer cell is unable to repair its genome and is destroyed through catastrophic accumulation of irreparable DNA damage (Audeh et al., 2010; Chiarugi, 2012; Shaheen et al., 2011; Weston et al., 2010; Yap et al., 2011). Other healthy cells without the DDR mutations would repair the damage and remain unaffected, and therefore this approach should be less toxic than standard DNA damage inducing agents (Weston et al., 2010).

The heavy involvement of ATM in the DNA damage response means that cancers deficient in ATM are good targets for these synthetic lethal approaches. ATM is the principal integrator of the DDR for DSBs, and directly phosphorylates HR mediators such as BRCA, Nbs-1 and Rad51 upon detection of DNA damage (Cortez et al., 1999; Starczynski et al., 2003). ATM is also a mediator of NHEJ responses and has been shown to function alongside the NHEJ mediators Artemis and DNA-PKcs (fig. 2), although ATM is not a core component unlike in

HR (Riballo et al., 2004). Collectively, ATM-mutant B-CLL tumours may be vulnerable to therapies targeting redundant DNA repair pathways independent of ATM (Weston et al., 2010). One such mediator of these sub-pathways are the poly (ADP-ribose) polymerases (PARPs).

1.6 Synthetic lethality in practice: PARP inhibition

The PARP family consists of 18 enzymes. PARPs catalyse the poly(ADP-ribosyl)ation of proteins, a process whereby ADP-ribose polymers are formed from donor NAD+ molecules and attached to proteins via ester bonding with glutamic acids, aspartic acids or lysine residues (Woodhouse and Dianov, 2008). Poly(ADP – ribosyl)ation is a ubiquitous cellular process, and two members of the PARP family, PARP1 and PARP2, are known to play active roles in DNA repair. PARP1 shows significant overlap and is active in both DSB and SSB repair. For DSBs, PARP1 aids exposure of ssDNA by promoting DNA end resection via EXO1 and BLM, thus assisting HR (fig. 2). PARP1 also promotes the less accurate alternative NHEJ pathway (Wang et al., 2006) (fig. 2). For SSB repair, PARP1 is a mediator of the base excision repair (BER) mechanism (Shaheen et al., 2011). These roles in the DDR therefore make PARP1 an attractive target for synthetic lethal cancer therapy approaches, as

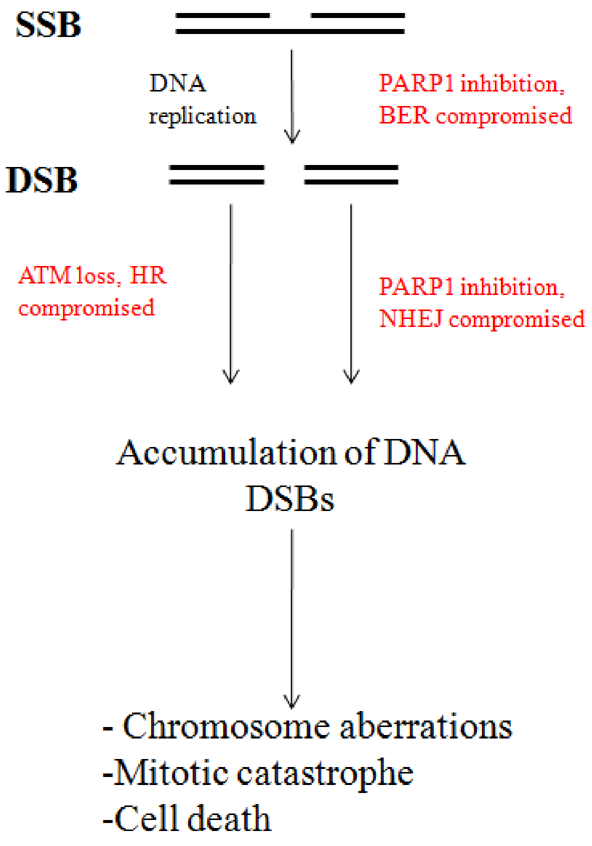

Figure 3 - Proposed mechanism of synthetic lethality when PARP1 is inhibited in an ATM deficient tumour undergoing deregulated replication.

they mediate DDR mechanisms that HR deficient cancers may rely on.

PARP inhibitors (PARPis) have already proven to be an effective strategy in cancers such as BRCA-deficient breast and ovarian cancer and ATM deficient B-CLL (Audeh et al., 2010; Fong et al., 2010; Weston et al., 2010). BRCA1 and BRCA2 are major mediators of HR, and BRCA requires phosphorylation via ATM to function, hence in these cancers HR is compromised (Cortez et al., 1999). Thus, ATM and BRCA deficient cells are dependent on PARP1-mediated DNA DSB repair processes such as alternative NHEJ and single-strand annealing (SSA, fig.2), and PARP1 inhibition also removes these options. BER is also compromised without PARP1 function, meaning that SSBs go unrepaired and are converted to DSBs during DNA replication. ATM deficient cells cannot repair these DSBs via HR, the result of which is the accumulation of DSBs and mitotic catastrophe (Weston et al., 2010) (fig. 3). Importantly, the highly proliferative nature of ATM deficient tumours contributes to the killing mechanism because the increased frequency of DNA replication leads to more and more unrepaired DSBs (Weston et al., 2010).

From a clinical perspective, olaparib (AZD2281) is one of the most commonly used PARP inhibitors, and is credited with being fairly well tolerated and having high oral bioavailability (Audeh et al., 2010). Side effects are generally manageable and include fatigue, nausea and lymphocytopenia (Vasiliou et al., 2009). Olaparib can be used as a single agent or in conjunction with cytotoxic drugs, DNA damage inducers such as platinum-based compounds, or radiotherapy (Vasiliou et al., 2009). Initial clinical trials of olaparib on BRCA1 and 2 compromised breast and ovarian cancers have yielded positive results (Audeh et al., 2010; Fong et al., 2010). Previous *in vitro* studies have also highlighted the effectiveness of Olaparib in the specific killing of ATM-deficient B-CLL tumour cells (Weston et al., 2010). Olaparib is currently undergoing clinical trials in B-CLL for patients that are not responding to conventional treatment. It is also undergoing clinical trials for the treatment of T-prolymphocytic leukaemia (T-PLL) and mantle cell lymphoma (MCL), haematological malignancies in which ATM dysfunction is also common (Weston et al., 2010). ATM-deficient B-CLL patients are currently participating in phase II trials with olaparib (Pratt, 2011).

1.7 PARPi resistance

Although PARPi therapy has been generally well received, there have recently been numerous reports of resistance to PARPis, posing a potential clinical problem to PARPi monotherapy. For example, in BRCA$^{-/-}$ and p53$^{-/-}$ mammary adenocarcinomas transplanted into mice, olaparib was initially shown to have potent anti-tumour effects, but resulted in eventual tumour growth relapse during treatment as well as after discontinuation (Rottenberg et al., 2008). Interestingly, a contributor to this resistance was found to be due to the PARPi-induced upregulation of Abcb1a/b P-glycoprotein efflux pump genes, which remove xenobiotics from cells and are often a problem in chemotherapeutic resistance (Wurzer et al., 2000). It has also been reported that PARP1 itself may ribosylate and inhibit members of the ABC transporter family such as P-glycoprotein pumps, and thus the inhibition of PARP1 may actually contribute to the extrusion of the inhibitor compound (Dumitriu et al., 2004). In addition, there have been reports of HR mechanisms being restored in PARPi-treated BRCA1 or -2 deficient cells, suggesting that the increased genomic instability stemming from inhibition of PARP1 could induce restorative mutations in BRCA genes (Edwards et al., 2008). These observations suggest that PARPi monotherapy may not be an effective long term strategy.

These phenomena have not yet been observed in ATM-deficient B-CLL, however, and the induction of synthetic lethality via PARPi is still a promising option. The concept of using

PARPis as sensitising agents to radiotherapy and traditional DNA damage inducing chemotherapeutic methods, such as platinum salts, is a strategy that some groups have explored (Rottenberg et al., 2008). The toxicity of these compounds is still a problem, however, especially because the majority of progressive B-CLL sufferers are elderly. The optimum chemotherapeutic compounds to use in combination with PARPi are also yet to be resolved (Yap et al., 2011). One method of increasing the tumour-killing effectiveness of PARPis and possibly counteracting these observations of PARPi resistance could be to administer PARPis alongside other novel and less toxic DNA-damage response targeting compounds, to further increase the synthetic lethal effects of DDR inhibition on HR deficient tumours. One potential molecular target is the histone deacetylase (HDAC) family, which, amongst numerous other roles, are implicated heavily in the DDR.

1.8 HDAC functions

HDACs are antagonistic to histone acetyltransferases (HATs), which transfer the acetyl group from acetyl CoA to lysine residues on proteins, forming ε-N-acetyl lysines (fig. 4). This process, termed acetylation, is essential for many cell processes. The most prominent of these processes is the regulation of chromatin dynamics. HATs acetylate conserved lysines on the N-terminal tails of histones H3 and H4, as well as H2A and H2B to a lesser extent (Federico and Bagella, 2011). This confers an open nucleosomal structure, termed euchromatin, which is more accessible to transcriptional machinery and thus more conducible to gene transcription. HDACs oppose this action, and deacetylate histones to revert chromatin back to a more condensed form, heterochromatin (fig. 4). Thus, HDACs are negative regulators of gene expression (Federico and Bagella, 2011).

18 mammalian HDACs are known, which fall into 4 groups. Class I HDACs are all nuclear and ubiquitously expressed. Class II HDACs are thought to shuttle between the nucleus and

cytoplasm and are tissue specific. Class III HDACs include the NAD$^+$-dependent sirtuin HDACs, while class IV contains only one HDAC, HDAC11 (Federico and Bagella, 2011). Some HDACs, such as the Class I HDACs HDAC 1 and HDAC2, have been found to be overexpressed in many cancers. Similarly, HDAC ablation often results in a loss of proliferation and/or apoptosis induction highlighting their tumorigenic properties (Jurkin et al., 2011).

As HDACs are mainly negative gene regulators due to the effects on chromatin, HDAC inhibition results in widespread gene upregulation (fig. 4), which can have anti-cancer effects. Aberrantly silenced tumour suppressor genes may be upregulated, such as p21^{WAF1}, p27^{KIP} and p16^{ink4a} (Marks et al., 2000; Richon et al., 2000). HDAC inhibitors may also cause the upregulation of pro-apoptotic factors, such as Bim and TRAIL (Nebbioso et al., 2005; Tan et al., 2005) or result in repression of survival factors such as survivin (Chowdhury et al., 2011).

However, acetylation is not only restricted to histones and chromatin dynamics. Thus, HDACs have a wide range of other targets, including oncogenic transcription factors and tumour suppressors that are involved with progression of certain cancers. Some examples include p53 (Gu and Roeder, 1997), E2F (Martinez-Balbas et al., 2000), c-Myc (Patel et al., 2004) and NF-κB (Chen et al., 2001). It is therefore no surprise that HDAC activity is often altered in cancer. HDACs have also been directly linked with the function of oncogenic translocation products in lymphomas and leukaemias, such as PML-RARα in acute promyelocytic leukaemia (APL) (Matsushita et al., 2006).

Collectively, it is clear that HDACs are important in cancer progression for many reasons. However, the role of HDACs in the DDR is of particular interest to this study, because HDACs are therefore potential targets for synthetic lethal strategies in the treatment of B-CLL (Robert et al., 2011).

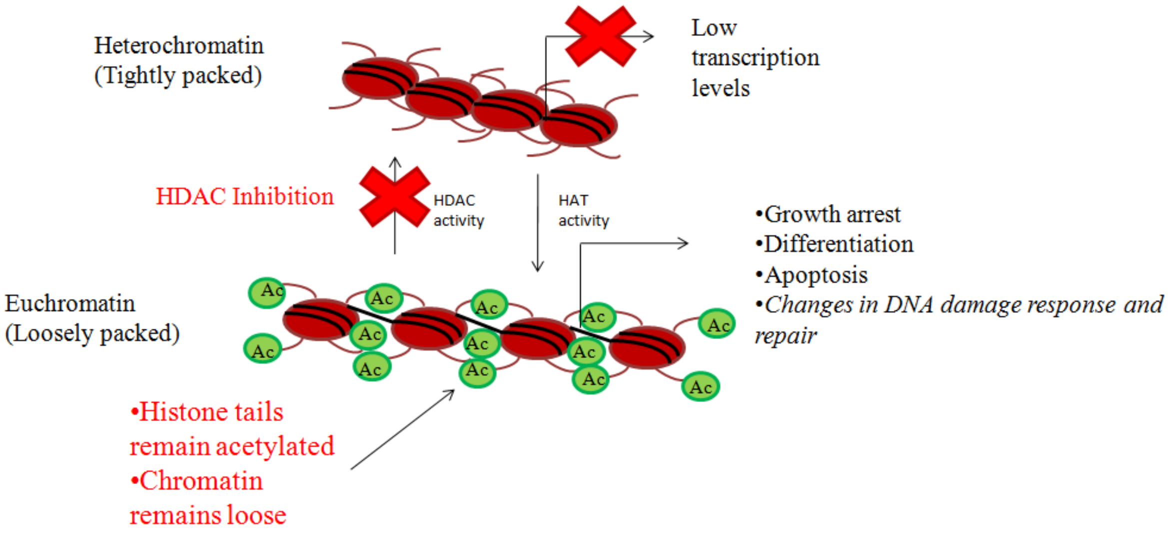

Figure 4 - A basic representation of the effects of HDAC inhibition on chromatin dynamics and a summary of some resulting cellular responses.

1.9 HDACs in DNA repair

In the event of DNA damage, histones undergo many post-translational modifications (PTMs) that impact on the DNA repair process itself or the chromatin restoration step, acetylation being one of the most important forms (Corpet and Almouzni, 2009). Lysines H3K9 (Tjeertes et al., 2009) and H3K56 (Miller et al., 2010; Yuan et al., 2009) are deacetylated in the event of DNA damage, and result in genomic instability in yeast and mammals if not deacetylated by HDACs in the event of DNA DSBs (Yuan et al., 2009). The precise mechanisms by which the acetylation status of these histones affects DNA damage responses are largely unknown, but H3K56 is close to the DNA entry/exit point of the nucleosome core and this acetylation may affect nucleosomal stability (Groth et al., 2007). HDACs, chromatin dynamics and ATM have also been directly linked in the DDR. For example, the ATM-Chk2 pathway may be required for completion of DNA repair, H3K56 re-acetylation and cell-cycle resumption after ultraviolet (UV)-induced DNA damage (Battu et al., 2011). UV damage usually results in SSBs repaired by nucleotide excision repair (NER), mediated by the ATR-Chk1 pathway, highlighting the high levels of crosstalk of DDR mediators (Battu et al., 2011). There is also evidence to suggest that in the event of HDAC inhibition, ATM can act as a transcription modulator and upregulate expression of anti-apoptotic genes such as MCL-1 (Jang et al., 2010), thus HDACis may be more effective on ATM deficient tumours.

HDACs are also involved in HR. The idea of HDAC involvement in HR is counterintuitive, because euchromatic DSBs are far more conducible to HR than heterochromatic DSBs (Chiolo et al., 2011). Thus, HDACs are more likely to play direct roles in HR rather than regulating chromatin dynamics. Indeed, this has been observed in yeast, whereby the recombination protein Sae2 is acetylated and degraded when HDACs are inhibited (Robert et al., 2011). HDAC1 and -2 are mediators of DSB repair, particularly acting on NHEJ effector proteins (Miller et al., 2010).

HDACis have also been found to actively induce cell killing through autophagy, due to the induction of reactive oxygen species (ROS) and subsequent DNA damage (Fu et al., 2010; Robert et al., 2011). This tumour-suppressive action is independent of apoptosis, and has been shown to be effective in several resistant forms of cancer. This is therefore an attractive mechanism to explore in treatment-resistant B-CLL forms.

Collectively, the roles of HDACs in the DDR are clearly very complex and convoluted. However, regardless of the underlying mechanism, it is clear that HDACs are important in the DNA damage response, and HDAC inhibitors are therefore a viable therapeutic strategy in the treatment of ATM-deficient B-CLL.

1.10 HDAC inhibitor classes

HDAC inhibitors can be divided into four distinct structural classes. These are the small molecular weight carboxylates; hydroxamic acids; benzamides and cyclic peptides. Some inhibitors target only specific HDACs or classes of HDACs, while others target a wider range, termed pan-HDAC inhibitors. All currently known HDAC inhibitors target the zinc molecule present within the active site of Class I, II and IV HDACs (Federico and Bagella, 2011). It has been observed that H3K9 and H3K56 remain broadly acetylated in the event of DNA damage when each of these classes are inhibited, whilst only mild acetylation remains with class III sirtuin HDACis (Tjeertes et al., 2009). This suggests that class III HDACs may not contribute as much as other classes to HDAC DNA damage responses. Conversely, another study reported that H3K56 acetylation increased when SIRT1, a class III HDAC, was inhibited, thus the mechanism remains unclear (Yuan et al., 2009). Many HDACis have been approved for clinical trials, and most have yielded positive results with relatively mild toxicity (Ellis and Pili, 2010; Federico and Bagella, 2011). There have been reports of HDACi related cardiotoxicity, but the most common effects include fatigue, transient thrombocytopenia and relatively mild gastrointestinal complications such as nausea, vomiting and diarrhoea (Federico and Bagella, 2011). Monotherapeutic approaches with HDACis have shown fair anti-tumour activity, but like PARP inhibitors, the true potential for HDACis probably lies in combination with other therapies (Ellis and Pili, 2010).

1.11 Aims

Like PARP inhibition, the involvement of HDACs in the DNA damage response opens possibilities of using HDAC inhibitors as radiosensitisers or chemosensitisers (Camphausen and Tofilon, 2007; Miller et al., 2010; Robert et al., 2011). It has already been shown that PARP and HDAC inhibitors synergise to upregulate DNA damage-induced apoptosis in the HCT116 colon cancer cell line (Adimoolam et al., 2007). However, in the absence of

ATM/p53 mediated apoptosis in DNA damage, PARP inhibitors induce cytotoxicity through unrepaired DNA damage, and it is highly possible that HDACis can increase this effect (Weston et al., 2010).

As previously discussed, PARP1 and HDACs mediate various DDR responses, and there is much ambiguity and crosstalk between the individual DDR mechanisms and their corresponding molecular pathways. In the absence of ATM and thus efficient HR, ATM-null B-CLL tumours may place a higher dependency on PARP/HDACs for coordinating DNA repair responses. As also discussed, the novel therapeutic potential of PARP and HDAC inhibition alone in HR-compromised cancers has been extensively reported. As the DNA damage response is such a complex and convoluted network, using both PARP and HDAC inhibitors in combination may result in synergy and heighten the synthetic lethal effect on ATM-deficient B-CLL tumours, because further DDR mediators that HR deficient cells may fall back on are inhibited. The recently reported abilities of HDACis to induce DNA damage and autophagic tumour killing independent of apoptosis are also promising. Based on these speculations, it was therefore hypothesised that treatment with PARP inhibitors would render ATM-deficient B-CLL tumours preferentially sensitive to further treatment with HDAC inhibitors, producing a synergistic tumour-killing effect more potent than PARP inhibition or HDAC inhibition alone. Indeed, some evidence for this has already been observed, but not confirmed (Weston et al., 2010).

The primary aim of this project was to further investigate the therapeutic potential for the use of HDAC inhibitors alongside PARP inhibitors in the treatment of ATM-deficient progressive B-CLL. A side aim was to also assess the effects of the drugs on p53 mutant cells of differing ATM status. The study objectives were to:

- identify ATM mutants in a cohort of 28 B-CLL patients

- assess the tumour killing effectiveness of PARP and HDAC inhibitors *in vitro*
- investigate the synergic potential of PARPi/HDACi combined therapy in ATM and/or p53 deficient B-CLL tumour cell killing and the mechanisms by which this synergy is driven.

2.0 Materials and Methods

2.1 B-CLL patient tumour sample preparation

Human peripheral blood samples were obtained from B-CLL patients from Birmingham and Bournemouth hospitals. To extract tumour cells, the samples were made up to a volume of 30 ml with RPMI 1640 cell culture media with glutamine (Invitrogen) and pipetted onto 20 ml lymphoprep (Axis-Shield) in falcon tubes. The samples were then centrifuged at 1,600 RPM for 30 minutes with deceleration brake disabled (Beckman Coulter Allegra X-12 Centrifuge). The B-CLL tumour cells were extracted and washed in RPMI 1640 media, and stored at -160^{o}C in 90% foetal calf serum (FCS, Sigma) with 10% dimethyl sulfoxide (DMSO, Sigma) at a density of $5x10^{7}$ cells/ml.

2.2 Genomic DNA extraction

B-CLL tumour cell samples as prepared above were thawed at RT and washed in 20 ml RPMI 1640 media (Invitrogen) and washed twice in 20 ml dulbecco's phosphate-buffered saline (DPBS). DNA was extracted to manufacturers protocol using a Flexigene DNA kit 250 (QIAgen), resulting in genomic DNA samples resuspended in 200 µl FG3 Buffer (QIAgen).

2.3 DNA purification

Sodium acetate (20 µl at 3 M) and 400 µl pure ethanol (PAA) was added to the DNA samples and the DNA left to precipitate for 1 hour at -80 ^{o}C. The solution was span at 13,000 RPM for 30 minutes at 4 ^{o}C, the DNA pellet washed in 500 µl 70% ethanol and resuspended in FG3 buffer (QIAgen). DNA concentration and purity was measured via spectrophotometry (Implen Nanophotometer) and diluted to final concentrations of 10 ng/µl in FG3 buffer (QIAgen).

2.4 LightScanner mutation analysis (Hi-Res Melting)

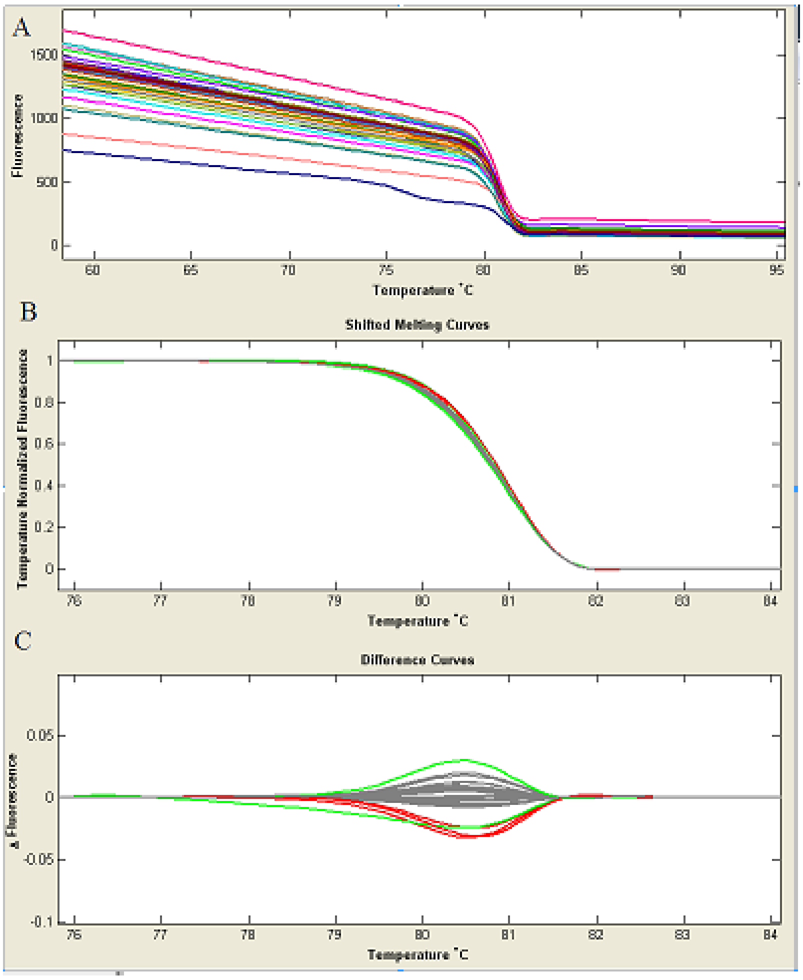

Figure 5 – Hi-Res Melting analysis. **A**. Melting Curves of individual samples for ATM exon 10. **B**. Normalised fluorescence levels. **C**. Isolating potential sequence variants via level of deviance relative to the standard curve. Green curves represent potential sequence variants while red curves represent a potential group of similar sequence variants.

Hi-Res melting, using LightScanner and Call-IT software (Idaho Technologies), is a novel high-throughput technique whereby many samples can be analysed for potential DNA sequence changes simultaneously. The process involves polymerase chain reaction (PCR) being simultaneously carried out on both forward and reverse strands of an exon of interest, in the presence of a fluorescent dye, LCgreen (Idaho Technologies), that intercalates between bases in double-helix DNA molecules. The dye is inactive when free, but fluoresces when intercalated with DNA in a closed double helix conformation, which occurs as a result of spontaneous annealing of forward and reverse strands. Fluorescence levels can be quantified to give a measure of PCR product amount. By incrementally increasing the temperature of the DNA molecule to the point at which double strand DNA (dsDNA) will dissociate into single strand DNA (ssDNA), also resulting in dissociation of the dye, a DNA melting curve profile can be obtained by comparing relative fluorescence levels against temperature. The simultaneous heating of exons of multiple patients allows for the direct comparison of individual DNA melting profiles against each other and a known wild-type (WT) profile (fig. 5). Differential melting curve characteristics denotes a change in the kinetic properties of the DNA molecule and therefore potential mutant samples. Homoduplexes (dsDNA with matching maternal and paternal strands) have different melting profiles to heteroduplexes (mismatched strands indicating mutation), allowing detection of heterozygous mutations, such as single nucleotide polymorphisms (SNPs). Samples with highly variant curves were sequenced via the Sanger method to confirm the presence of any potential mutations, and the nature of the mutation.

Individual DNA samples (2 µl at 10 ng/µl) were pipetted into individual wells of an opaque 96 well plate (4titude Framestar 96), for a final amount of 20 ng DNA. To each well containing DNA, the following reagents were added:

Reagent	**Volume**
HotShot Diamond PCR Mastermix (Clent Life Sciences)	5 µl
LCGreen gene scanning reagent (Idaho Technologies)	1 µl
Sterile distilled H_2O	2.8 µl
Forward Primer (Alta Bioscience)	0.1 µl
Reverse Primer (Alta Bioscience)	0.1 µl

HotShot diamond PCR Mastermix contains an optimum mixture of $MgCl_2$, PCR reaction buffer, dNTPs and Taq polymerase for the PCR reaction. This was performed for each ATM exon, and the primers used were at a concentration of 250 ng/µl throughout the study. Mineral oil (10 µl, Sigma) was added to overlay the reaction and PCR was performed to the following parameters (G-Storm GS1 Thermal Cycler, table over page):

Step	**Temperature**	**Time**
1. Initial Denaturation	95 °C	2 min
2. Denaturation	94 °C	30 sec
3. Annealing	X °C	30 sec
4. Homo/Heteroduplex Formation	94 °C	30 sec
5. Final Hold	25 °C	∞

X denotes the annealing temperature that differed according to the optimum primer annealing temperatures (see table S1 for information). Steps 2-3 were repeated 45 times.

2.5 Primer annealing temperature optimisation

DNA (2 µl at 10 ng/µl) was added to individual wells of a 96-well plate (VWR). The same volumes of reagents as above were added to the DNA, and PCR was carried out using the same above parameters excluding the annealing temperature; annealing temperature gradients of 53-61 °C and 60-68 °C were set up (G-Storm GS1 Thermal Cycler, TECNE TC-512), so that the annealing temperatures would incrementally increase lengthways across 96-well plates. By setting up multiple PCR reactions for each exon all along the temperature gradient, the optimum annealing temperature could be obtained by analysing the products from each different annealing temperature. The successes of the PCR reactions were measured by the presence of a melting curve using a LightScanner (Fig 6A). Gel electrophoresis was also performed to check for product (fig. 6B). PCR product (10 µl) with 3 µl loading buffer was ran on a 2% agarose gel with Tris/borate/EDTA (TBE) buffer. DNA was stained with SYBR safe (Invitrogen), which intercalates between DNA bases and is excited by UV light. DNA bands were visualised using a UV lightbox (Syngene G-box). The annealing temperature that produced the largest amount of DNA product whilst not producing any non-specific product was deemed to be the optimum annealing temperature for each primer. However, certain primers proved difficult to optimise (fig. 6). For "unclean" PCR reactions that contained non-specific product, higher annealing temperatures were attempted. For those that produced little or no product and/or amplified a particularly large exon fragment, a wider range of annealing temperatures was attempted, and the annealing time was increased from 30s to 1m 30s. The number of PCR cycles was also increased from 45 to 60 for such samples.

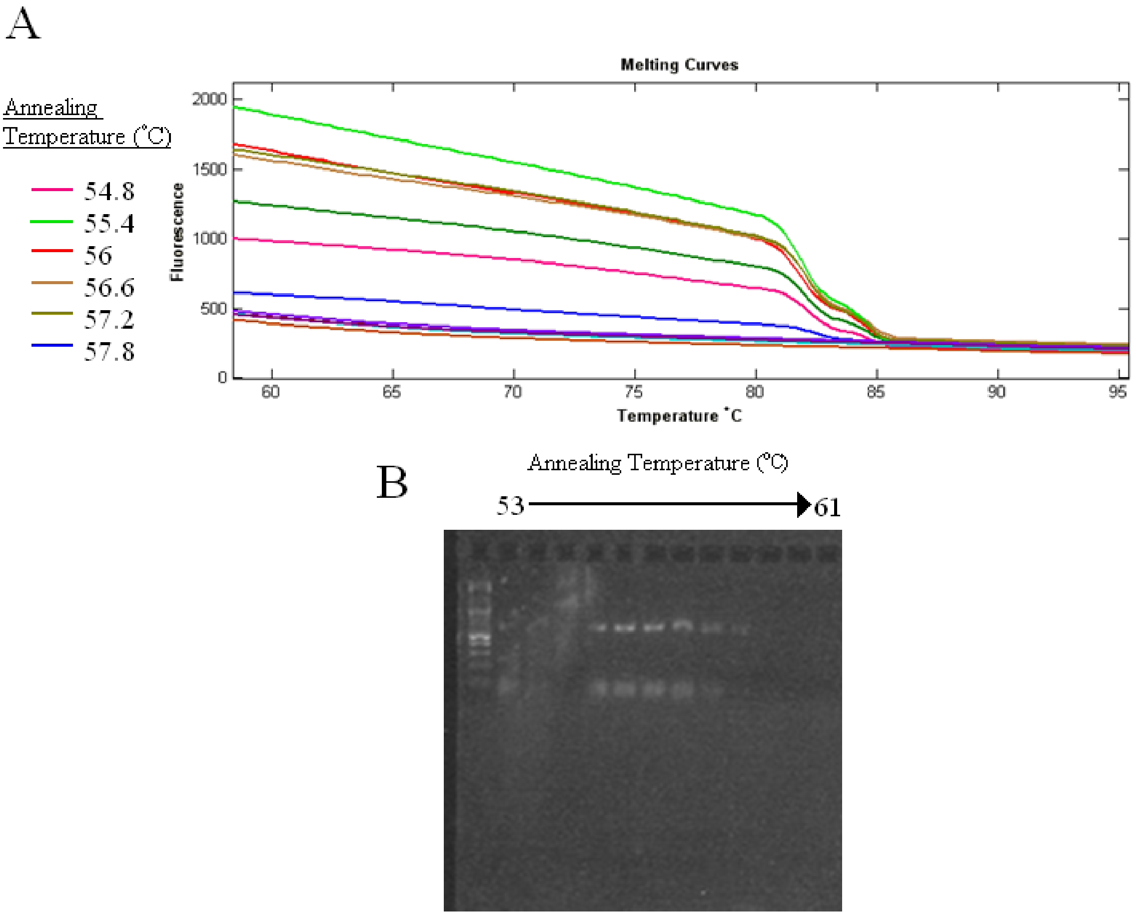

Figure 6 – Example of the primer optimisation technique, depicting ATM exon 26. **A**. Melting curves revealing the level of PCR product present at particular annealing temperatures. Note that there are two individual melts per curve rather than one smooth melt, indicating the presence of undesired PCR product. **B**. Agarose gel showing product levels/annealing temperature. Note that at these annealing temperatures the primers were producing two bands in each lane, confirming the presence of non-specific product. Exon 26 therefore required further optimisation.

2.6 Sequencing Analysis

Exons of interest were amplified using the Sanger method. The method involves the sequencing PCR reaction being carried out in the presence of both regular deoxynucleotides (dNTPs) and fluorescently labelled dideoxynucleotides (ddNTPs). Chain elongation proceeds until a ddNTP is inserted by DNA polymerase rather than a regular dNTP, which halts elongation. By chance, this will eventually occur for every base in the exon, producing DNA fragments of varying length ending with a fluorescently labelled nucleotide. The DNA is therefore sequenced based on the ascending order of size of DNA fragments, identified by the migration lengths on a capillary tube matrix, and detecting via laser which fluorescent nucleotide is present on each DNA molecule variant.

Individual DNA samples (2 µl at 10 ng/µl) were loaded onto 96-well plates. To each well containing DNA, the following reagents were added:

Reagent	**Volume**
TrueStart Buffer (Fermentas)	2.5 µl
$MgCl_2$ (Fermentas)	2 µl
dNTPs (Invitrogen)	0.2 µl
Sterile distilled H_2O	17 µl
TrueStart Taq polymerase (Fermentas)	0.3 µl
Forward Primer	0.5 µl
Reverse Primer	0.5 µl

PCR was then carried out to the following parameters (Applied Biosystems GeneAmp PCR System 9700, table over page):

Step	Temperature	Time
1. Initial Denaturation	95 ^{o}C	4 min
2. Denaturation	95 ^{o}C	30 sec
3. Annealing	X ^{o}C	30 sec
4. Extension	72 ^{o}C	45 sec
5. Final Extension	72 ^{o}C	7 min

X denotes the annealing temperature that differed according to the optimum primer annealing temperatures. Steps 2-4 were repeated 37 times. To purify the amplified exon regions, 2 µl ExoSap (Affymetrix) was added to wells of a fresh 96-well plate, to which 2.5 µl PCR product was added. This was then heated to 37 ^{o}C for 15 minutes and 80 ^{o}C for a further 15 minutes. The following reagents were added to the DNA/ExoSap product:

BigDye buffer (Applied Biosystems)	3.5 µl
BigDye reagent (Applied Biosystems)	1 µl
Forward or reverse Primer	0.3 µl
Sterile distilled H_2O	14.7 µl

BigDye contains the optimum mixture of dNTPs, fluorescently labelled dideoxynucleotides and DNA polymerase for the reaction. PCR was then carried out to the following parameters (table over page):

Step	Temperature	Time
1	96 °C	2 min
2	96 °C	10 sec
3	50 °C	5 sec
4	60 °C	4 min

Steps 2-4 were repeated 25 times. Pure ethanol (50 µl) with 4% sodium acetate was added to the PCR products and incubated at room temperature for 45 minutes. The plate was then span at 1500 g for 20 minutes and the supernatant removed. Ethanol (70%, 100 µl) was then added to the wells and the plate span at 1500 g for 12 minutes. The supernatant was removed and the DNA left to air dry at room temperature for 1 h. 10 µl HiDi Formamide (Applied Biosystems) was added to each well and the plate heated to 99°C for 5 minutes before rapid cooling on ice. The DNA/HiDi formamide solution was transferred to a 96-well sequencing plate (Applied Biosystems) and the DNA sequenced (Applied Biosystems/ Hitachi 3130XL 16 Capillary DNA Sequencer). Mutant exon sequences were identified by comparison with confirmed WT sequences obtained by the same method. For further confidence, such sequences were also compared for sequence similarity against the online human genomic database using the National Center for Biotechnology Information Basic Local Alignment Search Tool (NCBI BLAST, National Library of Medicine, USA).

2.7 Cell culture and cytotoxicity assays

Human B-CLL CII and MEC-1 isogenic cell lines were previously stably transfected with ATM shRNA. Green fluorescent protein (GFP) shRNA was also stably transfected into both cell lines as a negative control (Table S3). Cells were maintained in RPMI 1640 media with added glutamine (Invitrogen), containing 10% foetal calf serum (PAA) and 0.5% Penstrep (Invitrogen). Triplicate assays were performed in 96-well tissue culture plates (Corning).

Cells were seeded at a density of $1x10^5$/200 µl. All drugs were resuspended in DMSO. Olaparib (AstraZeneca) was added to wells at concentrations of 1 µM, 3 µM and 10 µM along with untreated control wells. The cells were incubated at 37 °C and 5% CO_2 for 48h before the addition of the following concentrations and types of HDACi to untreated cells and the varying concentrations of olaparib:

Drug	**CII**	**Mec-1**
Valproic Acid (VPA, Sigma)	1, 2.5, 5, 10 mM	1, 2, 3, 4 mM
Vorinostat (suberoylanilide hydroxamic acid - SAHA, Sigma)	1, 2.5, 5, 10 µM	1, 2.5, 3.5, 5 µM
Belinostat (PXD-101, Sigma)	1, 2, 3, 4 µM	1, 2, 3, 4 µM

The cells were incubated for a further 120 hours. After incubation, the cells were equilibrated to room temperature for 30 minutes. Cell TiterGlo (Promega) was used to assay for viable cells, which gives a quantifiable luminescent signal based on the levels of ATP present. The amount of ATP linearly correlates closely with the amount of viable cells present. 50 µl Cell TiterGlo was added to the wells, which were placed on an orbital shaker at 100 RPM for 10 min to induce cell lysis. The luminescence levels were analysed (Wallac Victor^2 1420 Multilabel Counter) and the surviving fractions quantified relative to the luminescence levels of the untreated controls.

2.8 Western Blotting

Both ATM and GFP knockdown (KD) CII and MEC-1 cells were lysed with 100 ml UTB buffer containing 9 M Urea, 150 mM β-mercaptoethanol and 50 mM Tris. A 6% polyacrylamide gel was prepared with the following reagents (table over page):

Reagent	Volume
Sterile distilled H_2O	27.4 ml
1M Tris/ 1M Bicine Buffer	4 ml
30% Acrylamide (BioRad)	8 ml
10% sodium dodecyl sulfate (SDS)	400 µl
Tetramethylethylenediamine (TEMED, Sigma)	80 µl
10% Ammonium persulfate (APS)	200 µl

Running buffer was composed of dH2O with 10% 1 M Tris/1 M Bicine Buffer and 0.1% SDS. 15 µl cell lysate was loaded with 5 µl loading buffer, composed of 30% glycerol, 10% SDS, 0.02% bromphenol blue and 2% 2-mercaptoethanol in dH_2O. The gel was ran at 25 mA for 5 hours. The transfer buffer contained 5600 ml sterile distilled H_2O, 1400 ml methanol (Sigma), 203 g Glycine (Sigma) and 40.6 g Tris (Sigma), and the gel was transferred onto nitrocellulose membrane at 200mA for 16 hours. Proteins were visualised on the nitrocellulose membrane with ponceau stain, comprised of 1 l dH_2O, 10 g Ponceau S and 30 g trichloroacetic acid. Membranes were washed in Tris-buffered saline - Tween (TBS-T) 3 times for 5 minutes and blocked for 2 hours in 5% dried milk/TBS-T. Washes were repeated and the membranes probed for total ATM using monoclonal mouse antibody (Calbiochem, 1:250) and total SMC-1 using polyclonal antibody (Bethyl, 1:5000), a downstream target of ATM, as a loading control. Primary antibodies were diluted in 5% bovine serum albumin (BSA) in TBS-T. Washes were repeated and the membranes incubated with secondary horseradish peroxidise (HRP)-conjugated antibody for 1 hour. Mouse α ATM (Dako) was diluted 1:1000 and rabbit α SMC-1 (Bethyl) at 1:3000 in 5% dried milk/TBS-T. ECR reagent was prepared immediately prior to use by mixing substrate (Millipore) and hydrogen peroxide (Dako) in a 1:1 ratio.

2.9 Visualisation of Rad-51 intra-nuclear foci by immunofluorescence staining

CII cell lines with stable GFP and ATM knockdown were treated with 3 µM vorinostat and DMSO as a negative control, and were irradiated with 2 Gy of ionising radiation (IR). The cells were then placed into ice-cold extraction buffer for 5 minutes. The extraction buffer was comprised of:

Reagent	**Volume (250ml total in dH_2O)**
10mM piperazine-N,N′-bis(2-ethanesulfonic acid) (PIPES)	0.81 g
300mM sucrose	25.67 g
20mM NaCl	1 ml of 5 M stock
3mM $MgCl_2$	6 ml of 500 mM stock
0.5% Triton X-100	1.25 ml

The cells were then fixed with 3.6% paraformaldehyde in PBS at timepoints of 0, 1, 8 and 24 hours after radiation exposure for 10 minutes. The cells were washed in DPBS 3 times for 5 minutes and blocked using 10% FCS in DPBS for 12 hours. Individual samples were stained with the following antibodies (Table over page):

1^o Antibody	2^o Antibody
Mouse monoclonal α γH2AX (Millipore, 1:1000)	α Mouse Alexa 488 (Invitrogen, 1:400)
Rabbit α Rad51 (Santa Cruz Biotechnology, 1:50)	α Rabbit Alexa 488 (Invitrogen, 1:400)

A488 was used for both samples because different cell samples were stained for RAD51 and γH2AX. Antibodies were diluted in 1% FCS in DPBS, and incubated for 1 hour at RT. Samples were stained in suspension with 1^o antibody, washed three times in DPBS for 5 minutes then stained in suspension with 2^o antibody.

2.10 Slide preparation, mounting and microscopy

Microscope slides were washed in 70% ethanol/1% HCl for 1 hour and washed 3 times for 20 minutes in dH2O before being left to dry overnight at 37°C. 20 µl poly-L-Lysine (Sigma) was carefully spread onto each well and left to dry for 20 minutes at RT. Slides were washed with dH_2O for 5 seconds and left to dry at 37 °C for 20 minutes. Cell suspension was added to wells of the slides and left to adhere for 45 minutes in dark conditions, then aspirated off and the slides left to dry for 10 minutes at RT in dark conditions. VECTAshield (20 µl) with 4',6-diamidino-2-phenylindole (DAPI, Vector Laboratories) was added to the wells before a glass coverslip was placed over the slide and left to dry for 20 minutes in dark conditions. Rad51 and γH2AX foci analysis was carried out using a Nikon Eclipse E600 Fluorescence Microscope and a 60x Plan Fluor objective. Images were captured and rendered using Hamamatsu C4742-95 Digital Camera and Volocity 3D Image Analysis software. Images of RAD51 and γH2AX staining were exposed for 2.5 seconds.

2.11 Data Analysis

Student’s two-tailed T tests were carried out on the means of three triplicate assays for each cell line differing in HDAC inhibitor treatment and ATM status. The effects of both drugs alone were compared with both in combination. Each dose combination was also compared between WT GFP knockdown control cells and ATM knockdown cells. Drug synergy was assessed by obtaining Combination Index (CI values) for each drug dose using CalcuSyn (Biosoft) software. Student’s 2-tailed T tests were also used to compare Rad51 positivity between untreated or 3 μM vorinostat treated cells as well as ATM knockdown and WT GFP knockdown control cells.

3.0 Results

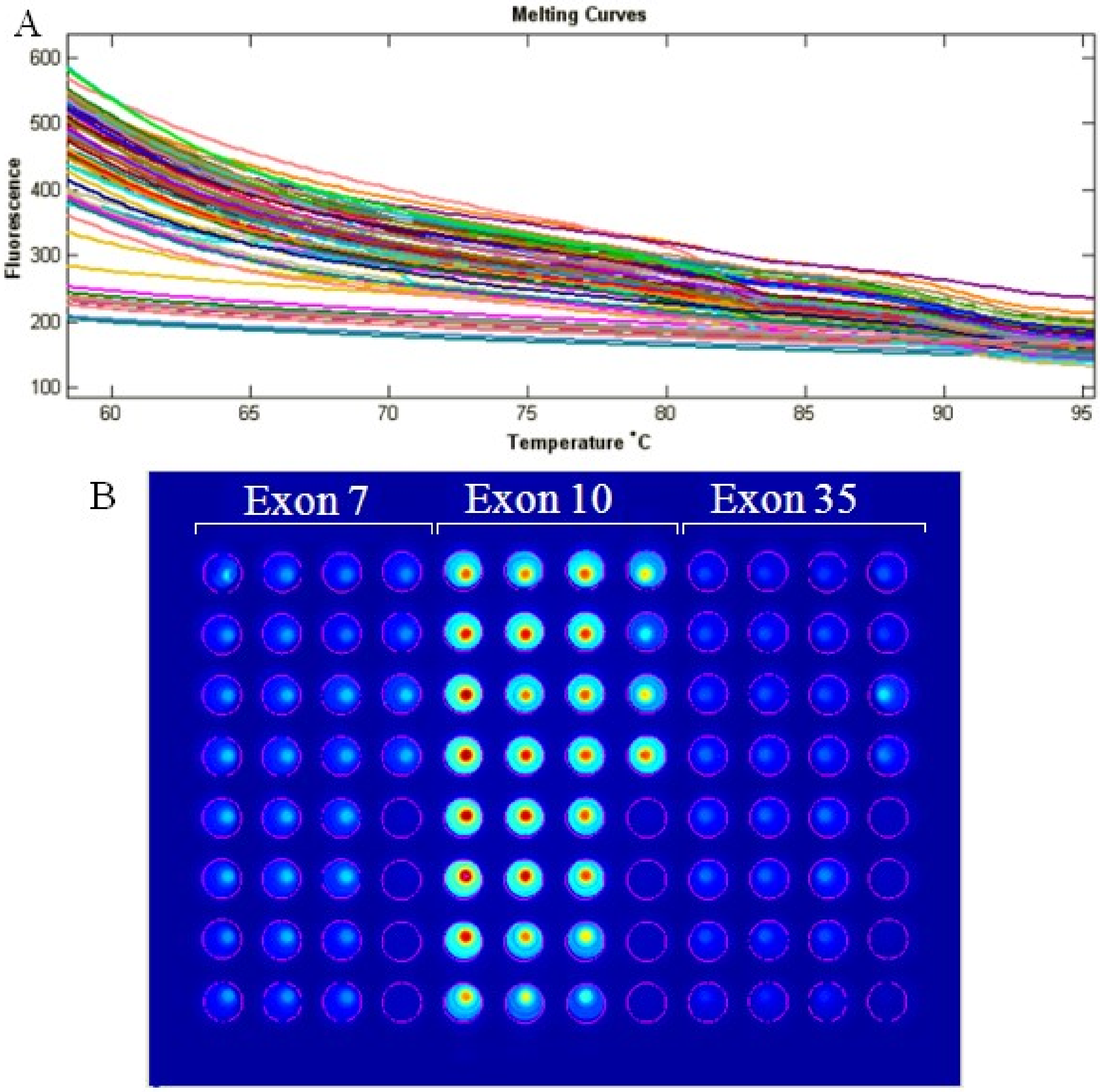

Figure 7 – Initial Hi-Res Melting problems. **A**. Example of failed melting curves that were originally observed due to lack of product. **B**. A map of the 96-well plate showing relative fluorescence levels and therefore product levels. Blue/green = low fluorescence; yellow/red = high fluorescence. The example provided shows three exons with identical optimum annealing temperatures amplified on the same 96-well plate. Exon 10 was being amplified successfully, while exon 7 and 35 failed to produce any product.

3.1 Detection of ATM null B-CLL tumours

Initially, a cohort of 28 B-CLL patient tumours was first screened for potential ATM mutations using Hi-Res Melting. Initial PCR reactions were unsuccessful (fig. 7A), and to rectify this, the purity of the DNA samples was increased and the consistency of DNA sample concentration was confirmed at 10 ng/µl (see section 2.3). All PCR reagents were replaced excluding primers, but the same reaction volumes were maintained because these had been previously optimised and were known to be correct. This resulted in some improvement, but there was a consistent pattern of single exons producing product while others did not (fig. 7 B). It was therefore suspected that either the primers were not functioning properly or that the optimum primer annealing temperatures were incorrect. Thus, a revised set of primers for all ATM exons was ordered and annealing temperature optimisation was carried out on primers with amended sequences (see section 2.5/table S1). The optimum annealing temperatures for several new primers was established (table S1).

However, some primers proved to be difficult to optimise in the time available. Hi-Res melting mutational analysis was therefore resumed using the new primers and the new optimum annealing temperatures that had been confirmed, but many of these PCR reactions were still consistently failing. It was decided that curve variants of the exons that had worked would be sequenced, with the intention of sequencing samples with variant curves to assess if any mutations were indeed present (fig. 8A).

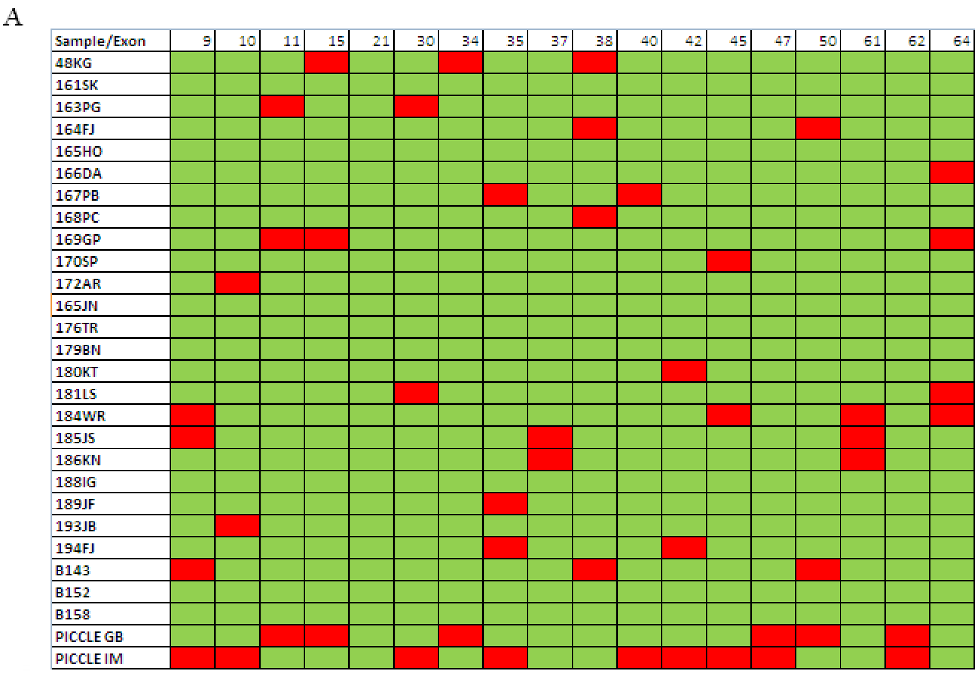

A

Sample/Exon	9	10	11	15	21	30	34	35	37	38	40	42	45	47	50	61	62	64
48KG	🟩	🟩	🟩	🟥	🟩	🟩	🟥	🟩	🟩	🟥	🟩	🟩	🟩	🟩	🟩	🟩	🟩	🟩
161SK	🟩	🟩	🟩	🟩	🟩	🟩	🟩	🟩	🟩	🟩	🟩	🟩	🟩	🟩	🟩	🟩	🟩	🟩
163PG	🟩	🟩	🟥	🟩	🟩	🟥	🟩	🟩	🟩	🟩	🟩	🟩	🟩	🟩	🟩	🟩	🟩	🟩
164FJ	🟩	🟩	🟩	🟩	🟩	🟩	🟩	🟩	🟩	🟥	🟩	🟩	🟩	🟩	🟥	🟩	🟩	🟩
165HO	🟩	🟩	🟩	🟩	🟩	🟩	🟩	🟩	🟩	🟩	🟩	🟩	🟩	🟩	🟩	🟩	🟩	🟩
166DA	🟩	🟩	🟩	🟩	🟩	🟩	🟩	🟩	🟩	🟩	🟩	🟩	🟩	🟩	🟩	🟩	🟩	🟥
167PB	🟩	🟩	🟩	🟩	🟩	🟩	🟩	🟥	🟩	🟩	🟥	🟩	🟩	🟩	🟩	🟩	🟩	🟩
168PC	🟩	🟩	🟩	🟩	🟩	🟩	🟩	🟩	🟩	🟥	🟩	🟩	🟩	🟩	🟩	🟩	🟩	🟩
169GP	🟩	🟩	🟥	🟥	🟩	🟩	🟩	🟩	🟩	🟩	🟩	🟩	🟩	🟩	🟩	🟩	🟩	🟥
170SP	🟩	🟩	🟩	🟩	🟩	🟩	🟩	🟩	🟩	🟩	🟩	🟩	🟥	🟩	🟩	🟩	🟩	🟩
172AR	🟩	🟥	🟩	🟩	🟩	🟩	🟩	🟩	🟩	🟩	🟩	🟩	🟩	🟩	🟩	🟩	🟩	🟩
165JN	🟩	🟩	🟩	🟩	🟩	🟩	🟩	🟩	🟩	🟩	🟩	🟩	🟩	🟩	🟩	🟩	🟩	🟩
176TR	🟩	🟩	🟩	🟩	🟩	🟩	🟩	🟩	🟩	🟩	🟩	🟩	🟩	🟩	🟩	🟩	🟩	🟩
179BN	🟩	🟩	🟩	🟩	🟩	🟩	🟩	🟩	🟩	🟩	🟩	🟩	🟩	🟩	🟩	🟩	🟩	🟩
180KT	🟩	🟩	🟩	🟩	🟩	🟩	🟩	🟩	🟩	🟩	🟩	🟥	🟩	🟩	🟩	🟩	🟩	🟩
181LS	🟩	🟩	🟩	🟩	🟩	🟥	🟩	🟩	🟩	🟩	🟩	🟩	🟩	🟩	🟩	🟩	🟩	🟥
184WR	🟥	🟩	🟩	🟩	🟩	🟩	🟩	🟩	🟩	🟩	🟩	🟩	🟥	🟩	🟩	🟥	🟩	🟥
185JS	🟥	🟩	🟩	🟩	🟩	🟩	🟩	🟩	🟥	🟩	🟩	🟩	🟩	🟩	🟩	🟥	🟩	🟩
186KN	🟩	🟩	🟩	🟩	🟩	🟩	🟩	🟩	🟥	🟩	🟩	🟩	🟩	🟩	🟩	🟥	🟩	🟩
188IG	🟩	🟩	🟩	🟩	🟩	🟩	🟩	🟩	🟩	🟩	🟩	🟩	🟩	🟩	🟩	🟩	🟩	🟩
189JF	🟩	🟩	🟩	🟩	🟩	🟩	🟩	🟥	🟩	🟩	🟩	🟩	🟩	🟩	🟩	🟩	🟩	🟩
193JB	🟩	🟥	🟩	🟩	🟩	🟩	🟩	🟩	🟩	🟩	🟩	🟩	🟩	🟩	🟩	🟩	🟩	🟩
194FJ	🟩	🟩	🟩	🟩	🟩	🟩	🟩	🟥	🟩	🟩	🟩	🟥	🟩	🟩	🟩	🟩	🟩	🟩
B143	🟥	🟩	🟩	🟩	🟩	🟩	🟩	🟩	🟩	🟥	🟩	🟩	🟩	🟩	🟥	🟩	🟩	🟩
B152	🟩	🟩	🟩	🟩	🟩	🟩	🟩	🟩	🟩	🟩	🟩	🟩	🟩	🟩	🟩	🟩	🟩	🟩
B158	🟩	🟩	🟩	🟩	🟩	🟩	🟩	🟩	🟩	🟩	🟩	🟩	🟩	🟩	🟩	🟩	🟩	🟩
PICCLE GB	🟩	🟩	🟥	🟥	🟩	🟩	🟥	🟩	🟩	🟩	🟩	🟩	🟩	🟥	🟥	🟩	🟥	🟩
PICCLE IM	🟥	🟥	🟩	🟩	🟩	🟥	🟩	🟥	🟩	🟩	🟥	🟥	🟥	🟥	🟩	🟩	🟥	🟩

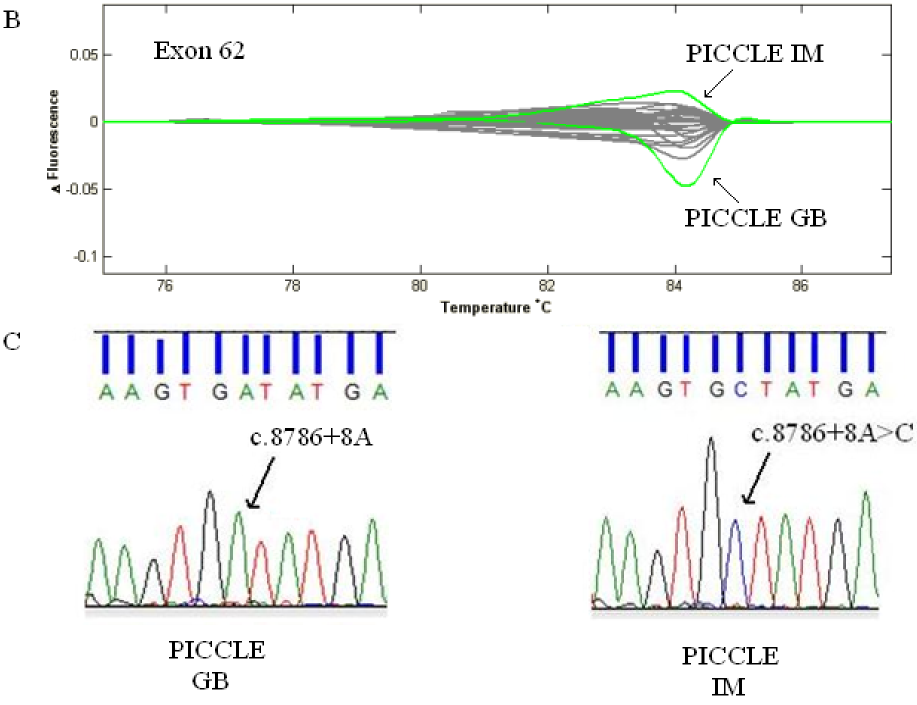

Figure 8 – Hi-Res Melting results. **A**. Table illustrating exons successfully analysed using H-Res Melting. Green indicates a normal melting curve; red indicates a variant curve that was sequenced to check for mutation. **B**. Graph depicting changes in melting curves of exon 62, with the variant curves of PICCLE GB and PICCLE IM tumours indicated (green). **C**. The homozygous SNP detected in the DNA fragment amplified by exon 62 primers of PICCLE IM compared with the WT sequence of PICCLE GB.

3.2 ATM exon sequencing

ATM exon samples that were flagged as potential mutants via Hi-Res melting were next sequenced (fig. 8 A, B). Surprisingly, only one sequence change was identified. A homozygous single nucleotide polymorphism (SNP) was identified in the PICCLE IM sample at c.8786+8A>C (Fig. 8 B, C), a non-coding intronic change. The change was located 8 nucleotides downstream of exon 62, which potentially could have been influential on ATM function because exon 62 lies within the C-terminal section of ATM, which contains the PI3 kinase domain along with its regulatory domains (fig.1). Mutations so close to exons often cause splicing problems. Interestingly, this particular SNP had been found to be relatively common in incidences of childhood T-lineage acute lymphoblastic leukaemia (T-ALL), and had been previously investigated by other groups (Gumy-Pause et al., 2006; Meier et al., 2006). However, these papers reported that no ATM mRNA splicing defects could be confirmed using reverse transcriptase (RT) PCR or DNA sequencing. It was therefore concluded that this SNP did not have an effect on the function of ATM, and it was decided to stop searching for ATM mutant patients and establish whether PARP inhibitors could sensitise B-CLL tumour cell lines, CII and MEC-1, to HDAC inhibitors.

3.3 Cytotoxic effects of combined PARPi/HDACi treatment – validations and assay optimisation

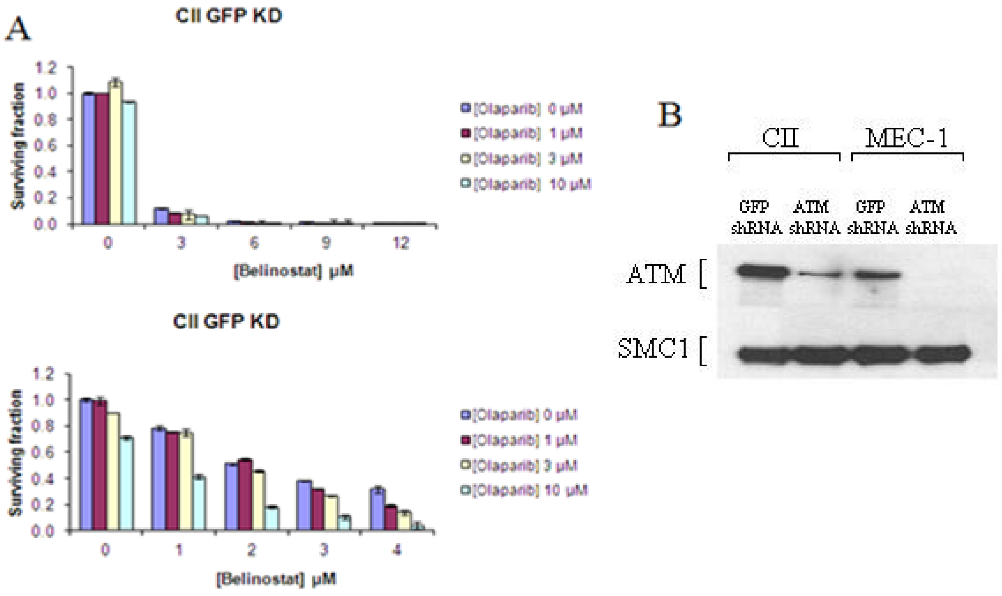

Figure 9 – Dose response optimisations and knockdown validation western blot. **A**. Example of HDACi dose optimisation. The top graph indicates the first concentrations of belinostat that were used on WT CII cells, and the resulting response. At concentrations above 6 µM all cells were killed, and the doses were lowered to produce an appropriate response as seen in the lower graph. This procedure was necessary for all HDAC inhibitors tested in both cell lines. **B**. Western blot to validate loss of ATM protein in cells treated with ATM shRNA. SMC1, a downstream effector of ATM, was used as a loading control.

The effectiveness of ATM knockdowns in CII and MEC-1 cells were verified via western blot. No ATM band could be observed in MEC-1 cells treated with ATM shRNA indicating a highly efficient knockdown. Residual ATM protein expression was detected in ATM shRNA treated CII cells, however, although the band observed was markedly fainter than GFP shRNA treated WT control cells (fig. 9B).

PARP and HDAC inhibition on CII and MEC-1 isogenic B-CLL cell lines were next analysed (See table S2 for cell line details). Previously studied concentrations of 1, 3 and 10µM were used because these values had previously produced an effect, but the doses of all three HDAC inhibitors had to be optimised on both CII and MEC-1 cells to obtain a viable dose response curve (fig. 9A). This process involved obtaining a starting figure from previous studies that had used the compound in cytotoxicity assays and further optimising the dose for the B-CLL cell lines. It was also noted that the concentrations of olaparib used were not inducing high levels of cytotoxicity. However, the concentrations of olaparib were not altered for a number of reasons. Firstly, previous studies had confirmed that 10 µM olaparib was a high enough concentration to inhibit all PARP1 activity in similar assays with B-CLL cell lines (Weston et al., 2010). Secondly, concentrations of olaparib above 10 µM are likely to induce off-target effects on cells not related to the role of PARP1 in the DDR. Poly(ADP-ribosyl)ation is a widespread cellular process, and high doses of PARP inhibitor are increasingly likely to disrupt this function to a point at which many other cellular processes other than the DDR are affected (Weston et al., 2010). Finally, the aim of the study was to investigate synergy between PARPis and HDACis rather than the effects of olaparib alone, and olaparib having a low effect may have caused any HDACi synergism to be more apparent.

3.4 Olaparib in combination with valproic acid

The first HDAC inhibitor that was assessed was valproic acid (VPA), as it had previously been shown to synergise with olaparib (Weston et al., 2010). VPA is a small molecular weight carboxylate compound, and inhibits the catalytic activity of class I and II HDACs, although more specifically class I (Lagace and Nachtigal, 2004). VPA has undergone promising trials in cervical cancer patients as well as acute myeloid leukaemia (AML) and myelodysplastic syndrome (MDS) both as monotherapy and in combination with other chemotherapeutics (Federico and Bagella, 2011).

Firstly, both ATM WT (GFP KD control) and ATM KD CII cells responded fairly similarly to olaparib and VPA alone. Both WT and ATM KD CII cells did not respond strongly to olaparib treatment, and ATM deficient cells were not significantly more sensitive to olaparib (fig. 10A). At 10 μM, the surviving fraction of WT cells was 0.69, and 0.8 in ATM deficient cells. Both WT and ATM deficient cells responded to VPA alone, with a surviving fraction of 0.16 and 0.19 respectively when 10 mM VPA was administered. Generally, higher doses of VPA resulted in lower surviving fractions, although, 2.5 mM VPA alone was observed to increase the proliferative capacity of ATM deficient cells. Surprisingly, CII WT cells appeared more sensitive to the same doses of VPA than ATM deficient cells, and consistently showed a lower surviving fraction than ATM KD cells for the same corresponding dose of VPA (fig. 10A). This observation was statistically significant for 5 mM and 10 mM VPA in combination with any olaparib dose ($P<0.05$).

The combination of olaparib with VPA had an additive cytotoxic effect on the surviving fractions as the dose of each drug was increased for both WT and ATM deficient cells. Generally, VPA combined with olaparib had a pronounced killing effect compared with olaparib alone in both WT and ATM deficient cells, a trend that was observed throughout the CII cell lines as olaparib had such a minimal effect. Interestingly in this case, compared to WT cells, ATM KD cells had more incidences whereby VPA in combination with olaparib had a significant killing effect compared with VPA alone – for example, all three doses of olaparib had a cumulative effect on the effectiveness of 5 mM VPA. However, lower doses did not produce such significant effects (fig. 10A).

To quantify any potential drug synergy, the data was then analysed using CalcuSyn. In WT cells, 1 and 3 μM olaparib were synergistic with 1mM VPA, and all doses of olaparib were synergistic with 10 mM VPA (fig. 10B). A different picture for ATM deficient cells was observed; generally, lower doses of VPA were more synergistic with lower doses of olaparib while 10 mM VPA was mildly antagonistic (fig. 10B). This was interesting because ATM deficient cells were synergising at lower doses where off-target effects were less likely to be occurring. However, there was little difference in surviving fraction between WT and ATM deficient cells in these lower doses, and the observed synergy may have been a result of the HDAC inhibitor alone not affecting ATM deficient cells as much as WT cells. Thus, WT cells were generally more sensitive to HDAC inhibitors overall and the differences in surviving fraction between the WT and ATM cells were not very great. It was therefore difficult to conclude that PARP and HDAC inhibitors synergised more in ATM knockdown cells.

The p53-mutant MEC-1 cells reacted in surprising ways to the drugs. Firstly they were more sensitive to VPA in general and lower concentrations had to be used than with CII cells (fig. 10A). In both ATM WT and ATM KD cells olaparib alone seemed to have an overall positive effect on cell proliferation. The same phenomenon was observed with 1 and 2 mM VPA, both alone and in combination with 1, 3 and 10 µM olaparib (fig. 10A). Higher concentrations of olaparib actually resulted in a higher proliferative effect in combination with 1, 2 and 3 mM VPA in ATM deficient cells, while the effect was especially pronounced in WT cells at 1 mM VPA. In WT cells, killing effects were observed with 3 and 4 mM VPA alone and in combination with olaparib, but no significant additive effect was observed with higher concentrations of olaparib. However, in ATM deficient cells, only 4 mM VPA resulted in any significant killing, and it was also observed that ATM deficient cells seemed to be more resistant to VPA than WT cells as seen in CIIs. Due to these unexpected observations, and that the CalcuSyn program requires an olaparib dose response curve, synergism values for olaparib and VPA treatment in MEC-1 cells could not be obtained.

From this evidence, it was difficult to conclude that ATM deficient cells were more sensitive to the combination of olaparib and VPA. The data for the p53 mutant MEC-1 cells was also inconclusive due to a lack of synergism data. However, it was clear that lower doses of

HDAC inhibitor had an increased proliferative effect on the MEC-1 cells, and that MEC-1 cells were generally more sensitive to HDAC inhibitor meaning that lower doses had to be used. Also, it was clear that WT cells were more sensitive to HDAC inhibitors than ATM deficient cells independent of p53 status. To verify these observations, the combined effectiveness of olaparib with a different HDAC inhibitor, vorinostat, was assessed.

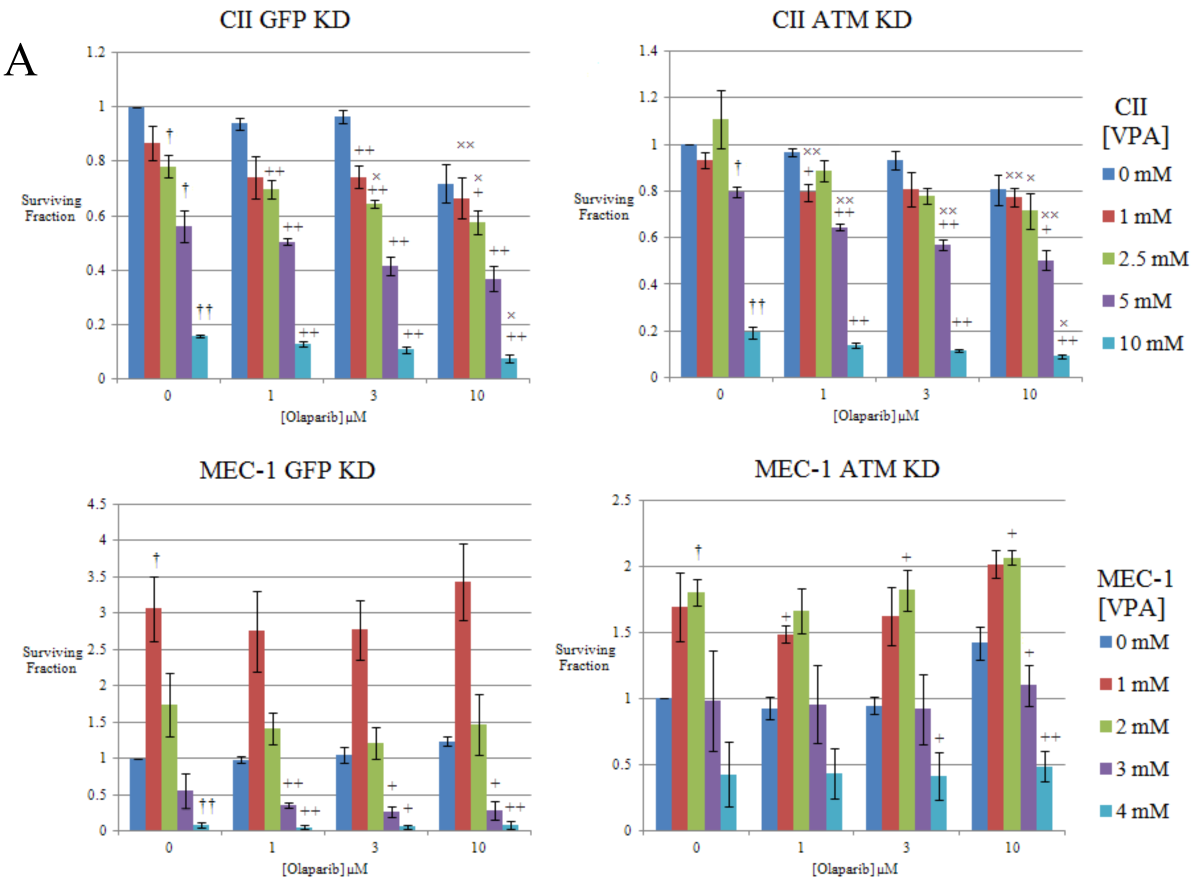

B

Olaparib + VPA							
Cell Line	**[VPA] mM**	**Combination Index**			**Synergism**		
		[Olaparib] µM			**[Olaparib] µM**		
		1	**3**	**10**	**1**	**3**	**10**
CII GFP KD	1	0.553	0.764	1.207	++	+	-
	2.5	1.076	1.065	1.408	+/-	+/-	-
	5	1.179	1.055	1.238	-	+/-	-
	10	0.657	0.619	0.605	++	++	++
CII ATM KD	1	0.228	0.436	0.881	+++	++	+
	2.5	0.579	0.593	0.896	++	++	+
	5	0.715	0.743	0.840	+	+	+
	10	1.152	1.142	1.124	-	-	-

Figure 10 - The effects of olaparib and VPA on CII and MEC-1 isogenic B-CLL cell lines. **A**. Dose response analysis for olaparib + valproic acid treatment responses of ATM WT (GFP KD control) and ATM KD CII and MEC-1 Cell lines.† = olaparib/HDAC inhibitor dose statistically significant relative to untreated control ($P < 0.05$, †† = $P < 0.01$). + = combined olaparib and HDAC inhibitor dose statistically significant relative to olaparib dose alone ($P < 0.05$, ++ = $P < 0.01$). × = combined olaparib and VPA dose statistically significant relative to VPA dose alone ($P < 0.05$, ×× = $P < 0.01$). n = 3, error bars represent standard error of the mean. **B**. Synergism ratings for each combined dose of olaparib + valproic acid in CII cell line. +++ = strongest synergy, ± = very minor synergy/antagonism, --- = strongest antagonism.

3.5 Olaparib in combination with vorinostat

The small molecule pan-HDAC inhibitor vorinostat (Federico and Bagella, 2011) was next assessed for synergy with the PARPi olaparib in ATM deficient B-CLL tumour cell lines. Vorinostat was used because it has undergone phase II clinical trials and been approved for treatment of refractory cutaneous T-cell lymphoma (CTCL) in the US (Marks and Breslow, 2007).

Again in CII cells, olaparib had a minimal and similar effect on both WT and ATM KD cell lines (fig. 11A). As expected, increasing doses of vorinostat resulted in decreasing surviving fractions in WT cells. However, once again ATM deficient cells were less affected by the same doses of HDAC inhibitor than WT cells – concentrations of 5 and 10 μM vorinostat at any combination produced significantly lower surviving fractions in WT cells ($P<0.05$). In ATM deficient cells, vorinostat alone actually had a greater cytotoxic effect at 1μM than at concentrations of 2.5 and 5 μM (fig. 11A). 10 μM vorinostat resulted in more substantial killing, reducing the surviving fraction to 0.5, but this was high compared to 0.14 as observed in WT cells treated with 10 μM vorinostat.

The combination of olaparib with vorinostat produced some interesting trends. In both WT and ATM deficient cells, 1 μM and 3 μM olaparib did not produce a statistically significant effect on the efficacy of vorinostat at concentrations of 1 and 2.5 μM compared to vorinostat alone, while 5 μM vorinostat produced a statistically significant but overall minor effect with these olaparib doses in WT cells but not ATM deficient cells (fig. 11A). At 2.5 μM, the surviving fraction in WT cells was even higher in combination with 1 and 3 μM olaparib, and this was also observed in ATM deficient cells with 1 μM olaparib. 10 μM olaparib caused an obvious additive effect in both cells of differing ATM status.

The synergism data for CII cells suggested that WT cells were more synergistic at higher levels of vorinostat, although mild synergism was observed in 1 μM olaparib combined with 1μM vorinostat (fig. 11B). This was also observed in ATM deficient cells, but 1 and 3 μM olaparib were also shown to be highly synergistic with 1 μM vorinostat, although strangely 1μM was antagonistic. 2.5 μM vorinostat with 1 and 3 μM olaparib was seen to be antagonistic in ATM deficient cells, reflecting the observation that the surviving fraction of cells treated with 2.5 μM vorinostat increased when combined with 1 μM olaparib relative to vorinostat alone. In general, both WT and ATM deficient cells showed olaparib/vorinostat synergy at many doses. Thus as with VPA, it was difficult to conclude that ATM deficient cells were more sensitive to combined treatment of olaparib and vorinostat, and it was even more evident in this case that WT cells were more sensitive to vorinostat than ATM deficient cells.

Similarly to the previous experiments with VPA, the p53 mutant MEC-1 cells were more sensitive to vorinostat and reduced doses had to be used. Again, olaparib did not exhibit a killing effect on MEC-1 cells and actually resulted in higher proliferation with increasing olaparib doses in both WT and ATM deficient cells. Thus again, it was not possible to obtain synergy ratings for olaparib and vorinostat in MEC-1 cells. As observed with VPA, low levels of vorinostat (1 μM, and 2 μM to a lesser extent in ATM deficient cells) unexpectedly resulted in a substantial increase in proliferation regardless of ATM status. At concentrations above 1 μM, vorinostat induced very high levels of killing in ATM WT cells, while contrastingly in ATM deficient cells only 3.5 μM and 5 μM resulting in any significant cytotoxicity. Due to this aberrant and unexpected behaviour of the MEC-1 cells, it was not possible to optimise the correct HDAC dose to provide reliable dose responses in both cells of differing ATM status.

Similar cytotoxicity patterns across CII and MEC-1 cells were observed with vorinostat as were also observed with VPA. It was not possible to conclude that olaparib and vorinostat resulted in more synergy in CII ATM knockdown cells. Again, p53-mutant cells showed an increased proliferative effect at low doses of HDAC inhibitor, and also were more sensitive in general thus requiring a lower dose range. In both cell lines, WT cells were clearly more sensitive overall to HDAC inhibition. The next step was to assess the effects of olaparib and a third HDAC inhibitor, belinostat.

A

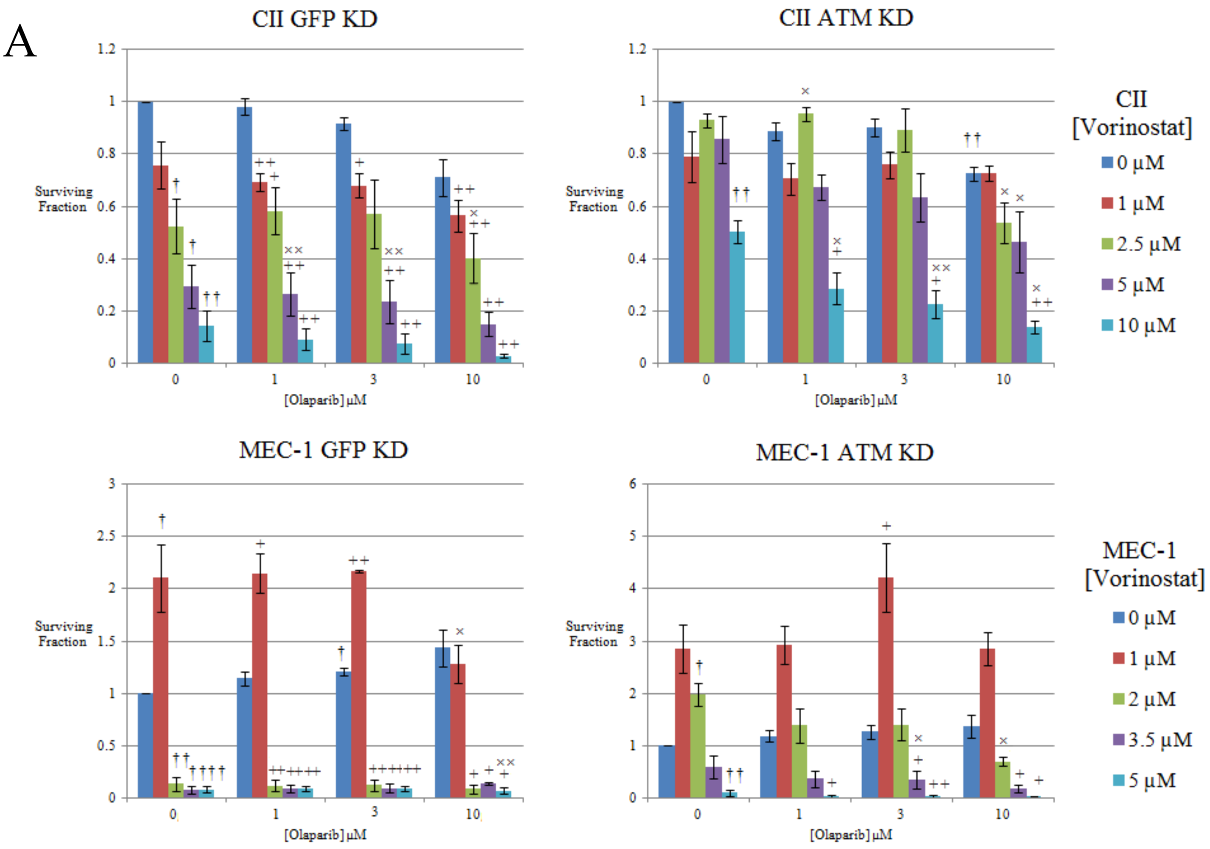

B

Olaparib + Vorinostat							
Cell Line	**[Vorinostat] µM**	**Combination Index**			**Synergism**		
		[Olaparib] µM			**[Olaparib] µM**		
		1	**3**	**10**	**1**	**3**	**10**
CII GFP KD	1	0.827	0.978	1.084	+	+/-	+/-
	2.5	1.332	1.416	1.090	-	+/-	+/-
	5	0.899	0.870	0.647	+	+	++
	10	0.665	0.617	0.301	++	++	++
CII ATM KD	1	0.235	0.535	1.205	+++	++	-
	2.5	1.787	1.601	0.719	--	--	+
	5	0.745	0.808	0.764	+	+	+
	10	0.581	0.498	0.415	++	++	++

Figure 11 - The effects of olaparib and vorinostat on CII and MEC-1 isogenic B-CLL cell lines **A**. Dose response analysis for olaparib + vorinostat treatment responses of ATM WT (GFP KD control) and ATM KD CII and MEC-1 Cell lines.† = olaparib/vorinostat inhibitor dose statistically significant relative to untreated control ($P < 0.05$, †† = $P < 0.01$). + = combined olaparib + vorinostat inhibitor dose statistically significant relative to olaparib dose alone ($P < 0.05$, ++ = $P < 0.01$). × = combined olaparib + vorinostat dose statistically significant relative to vorinostat dose alone ($P < 0.05$, ×× = $P < 0.01$). n = 3, error bars represent standard error of the mean. **B**. Synergism ratings for each combined dose of olaparib + vorinostat in CII cell line. +++ = strongest synergy, ± = very minor synergy/antagonism, --- = strongest antagonism.

3.6 Olaparib combined with belinostat

The final HDAC inhibitor that was analysed was belinostat, another small molecule pan-HDAC inhibitor also primarily targeting class I and II HDACs (Federico and Bagella, 2011). Belinostat has also been approved for and undergone clinical trials for the treatment of several haematological malignancies and solid tumours, showing good patient tolerance and promising anticancer activity (Federico and Bagella, 2011).

Both CII cell types responded to olaparib alone minimally across 1 and 3 μM, but a larger drop in surviving fraction was this time observed in WT cells from 3 to 10 μM, from 0.96 to 0.88 in ATM deficient cells and 0.94 to 0.69 in the control cells (fig. 12A). It was again very difficult to optimise the dose of belinostat for CII cells, due to the large differences in dose response observed between cells of differing ATM status - again, the viability of WT cells was compromised more than ATM deficient cells. 3 and 4 μM belinostat resulted in significantly reduced surviving fractions in WT cells compared to ATM cells ($P<0.05$).

Combining belinostat with olaparib did not result in any statistically significant changes relative to belinostat alone in WT cells, and more pronounced losses in surviving fraction with all doses of belinostat were observed with 10μM olaparib than the lower doses (fig.12A). In ATM deficient cells, lower doses of HDAC inhibitor did not produce dramatic additive effects with 1 and 3 μM olaparib, but higher doses of 3 and 4 μM belinostat had a more pronounced additive effect. With 10 μM olaparib, all concentrations of belinostat resulted in visibly reduced surviving fractions in comparison to belinostat alone, which was also seen in the WT cells. Again, the dose responses were similar in pattern across both cells of differing ATM status, with the exception that ATM KD cells were far more resistant to HDACi induced cytotoxicity. CalcuSyn was again used to analyse the data and establish any possible synergy that was occurring.

Synergism values indicated that in WT cells, 10 μM olaparib synergised with all doses of belinostat, and all doses of olaparib were synergistic with 4 μM belinostat (fig. 12B). 3 μM belinostat with 3 μM olaparib was also synergistic. In ATM deficient cells, 1, 2 and 3 μM belinostat was synergistic with 10 μM olaparib and 3 μM belinostat was synergistic with all olaparib doses. However, lower doses of olaparib combined with belinostat were highly antagonistic, reflected in the fact that 1 and 2 μM doses of belinostat actually increased the surviving fraction relative to the untreated control, or treated with 1 and 3 μM olaparib (fig. 12B). This was encountered because the HDACi induced killing effects between WT and ATM deficient cells were so different, and it was very difficult to obtain viable dose responses with the same doses on cells of differing treatment. As with the other HDAC inhibitors, there was little evidence for increased synergy between olaparib and belinostat in ATM deficient cells.

The p53-mutant MEC-1 cells responded to the drugs similarly to previous experiments, and thus it was very difficult to use the data to gain insight into drug synergy. Regardless of ATM status, olaparib once again had an overall positive effect across 10μM and it was again therefore not possible to calculate accurate synergism values due to the constraints of the CalcuSyn program (fig. 12A). Low doses of belinostat (1 μM) again resulted in increased proliferation in both cells, which was reduced with the addition of olaparib. WT cells were more susceptible to belinostat doses above 1μM than ATM deficient cells, in which additive killing could be observed as the doses of olaparib and belinostat increased, but the fact that the control cells were almost completely killed by doses higher than 1 μM meant that no sound conclusions could be drawn from the dose response data in MEC-1 cells.

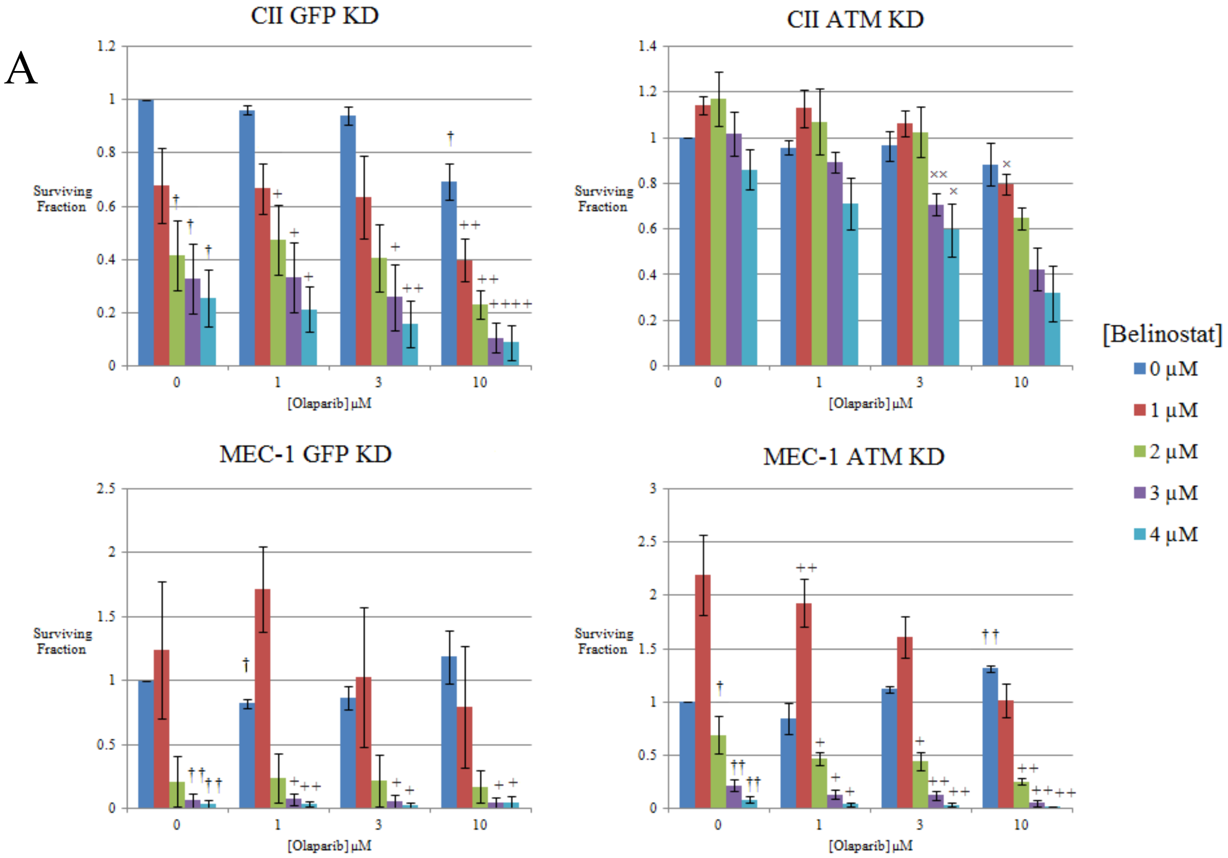

B

Olaparib + Belinostat							
Cell Line	**[Belinostat] µM**	**Combination Index**			**Synergism**		
		[Olaparib] µM			**[Olaparib] µM**		
		1	**3**	**10**	**1**	**3**	**10**
CII GFP KD	1	1.804	1.068	0.680	+/-	+/-	++
	2	1.097	0.929	0.575	+/-	+/-	++
	3	1.031	0.820	0.397	+/-	+	++
	4	0.848	0.670	0.430	+	++	++
CII ATM KD	1	$1.8x10^6$	$5.3x10^6$	0.76	---	---	+
	2	$1.8x10^6$	$5.3x10^6$	0.74	---	---	+
	3	0.864	0.837	0.818	+	+	+
	4	1.017	1.036	1.018	+/-	+/-	+/-

Figure 12 - The effects of olaparib and belinostat on CII and MEC-1 isogenic B-CLL cell lines **A**. Dose response analysis for ATM WT (GFP KD control) and ATM knockdown CII and MEC-1 cells.† = olaparib/belinostat inhibitor dose statistically significant relative to untreated control ($P < 0.05$, †† = $P < 0.01$). + = combined olaparib + belinostat inhibitor dose statistically significant relative to olaparib dose alone ($P < 0.05$, ++ = $P < 0.01$). × = combined olaparib + belinostat dose statistically significant relative to vorinostat dose alone ($P < 0.05$, ×× = $P < 0.01$). n = 3, error bars represent standard error of the mean. **B**. Synergism ratings for each combined dose of olaparib + belinostat in CII cell line. +++ = strongest synergy, ± = very minor synergy/antagonism, --- = strongest antagonism.

3.7 Common observations

Several common themes were observed across all cytotoxicity experiments with different HDAC inhibitors. Firstly, the concentrations of olaparib used did not have a significant cytotoxic effect on ATM deficient cells as previously observed. Olaparib had a marginal effect at 10 µM in CII cells, while in p53 mutant MEC-1 cells an increased proliferative effect was often observed rather than any cytotoxic effects at all, an effect that prevailed regardless of ATM status. The concentrations of olaparib used were kept constant, however, for reasons previously detailed.

It was also observed that HDACis had a more pronounced effect on WT cells than ATM deficient cells, with this effect having statistical significance at higher doses of HDAC inhibitor in CII cells. The same was observed in the p53 mutant MEC-1 cells although this was not statistically significant. MEC-1 cells also exhibited large increases in proliferation at very low doses of HDACi, but were significantly more sensitive to HDACis than CII cells overall - the surviving fraction rapidly dropped as the HDACi dose increased past the dose that induced proliferation. PARPis and HDACis were often shown to synergise in ATM deficient cells at various combinations of different concentrations of each drug. However, the same was often observed in WT cells, and coupled with the fact that WT cells were more sensitive to HDACis than ATM KD cells, it could not be comprehensively concluded that ATM defective B-CLL is selectively sensitised to HDACis by PARPis.

3.8 Mechanisms behind observations

To offer insight into the results observed in these experiments, the next step of the project was to establish if ATM dependent HR mechanisms were indeed compromised in cells treated with ATM shRNA. The effect of HDAC inhibition on these mechanisms was also analysed. To achieve this, both WT and ATM knockdown CII cells were exposed to ionising radiation

(IR) and immunostained for Rad51 foci formation. Rad51 is a DNA repair protein that is involved primarily with HR. In the event of DNA DSBs, Rad51 colocalises with and forms foci at the sites of the damage and modulates the recombinational repair of the breaks through homology sequence searching and strand invasion (Shaheen et al., 2011). Rad51 recruitment is dependent upon phosphorylation via the non-receptor tyrosine kinase c-abl in an ATM and DNA-PKcs dependent manner (Yuan et al., 2003). Thus, by quantifying the levels of Rad51-positive cells of differing shRNA and HDACi treatment, the presence of active HR can be assayed for and some insight may be gained as to why the cells reacted to PARPi and HDACi so unexpectedly. If HR was still active in ATM deficient cells, they would not be vulnerable to PARP inhibition as observed in previous experiments (Weston et al., 2010) because the unrepaired SSBs that turn to DSBs upon DNA replication would be repaired.

For this experiment, CII cells were used. This was because they produced the most legitimate dose response curves. Also, it was decided that p53 WT cells would be used for simplicity, as due to time constraints it was unlikely that Rad51 foci induction in both cell lines could be analysed. 3 µM of the pan-HDAC inhibitor vorinostat was used to treat the cells because reliable dose responses were shown in CII cells treated with vorinostat, and 3 µM was deemed a high enough dose to have an effect whilst also keeping any off-target effects to a minimum.

3.9 The effects of ATM knockdown and HDAC inhibition on HR

Firstly, as a positive control for cell labelling and the presence of DSBs, cells were stained for the DNA damage marker γH2AX. γH2AX is the phosphorylated form of histone H2AX, and is a rapidly induced biomarker of DNA DSBs. ATM is a principal mediator of γH2AX foci formation along with ATR and DNA-PKcs, but loss of ATM results in delayed resolution of γH2AX foci rather than a lack of γH2AX altogether (Wang et al., 2005). Immediately after irradiation very few γH2AX positive (5 or more foci) cells were observed, but at 1 hour post irradiation all samples, including ATM knockdown cells, showed 90-100% γH2AX positivity allowing for confidence that the staining protocol was effective and 2 Grays of IR was enough to reliably inflict DNA DSBs on the cells sampled (fig. 13A).

After the staining control was confirmed, the levels of Rad51 positive cells were assessed for each sample to quantify the relative levels of HR DSB repair in GFP shRNA (ATM WT), ATM shRNA and/or HDACi treated cells. Cells were analysed at 0, 1, 8 and 24 hours post IR treatment. Cells were classed as Rad51 positive if the cell contained five or more intra-nuclear Rad51 positive foci (fig. 13B).

Generally, Rad51 positive cells were shown to increase in proportion as the time after IR exposure lengthened (fig. 13C). For cells not treated with HDACi, the proportion of Rad51 positive ATM KD cells was significantly lower across 1 h, 8 h, and 24 h timepoints than in WT untreated cells (fig. 13C). The most striking reductions were observed 1 hour after IR, where the proportion of Rad51 positive cells in ATM KD cells was only 9.4% compared to 42.2% observed in WT cells. There was also a reduction at 8 hours post IR, from 50.7% in WT cells to 31.8% in ATM KD cells, while at 24 hours post irradiation 55% in WT cells were positive compared to 43.5% in ATM KD cells (fig. 13C). These data suggest that ATM knockdown results in diminished Rad51 foci formation, particularly at 1 hour after the occurrence of DSBs. There was still a relatively high proportion of Rad51 positive cells by 24 hours, however, suggesting that HR was not fully compromised.

Although 3 μM vorinostat appeared to result in marginally lower proportions of Rad51 positive cells across all timepoints in ATM deficient cells, this observation was not statistically significant. In WT cells however, a significant reduction was observed in HDACi treated cells at 0 and 1 hour after irradiation. At 0 hours post IR 10.1% of untreated WT cells were Rad51 positive, while 3.41% were observed in WT cells treated with vorinostat, and at 1h post IR the difference was 42.2% compared with 23.9%. These data support the idea that HDACs have some involvement in HR, particularly in the early onset of Rad51 foci. Again, however, a significant proportion of cells were still Rad51 positive at later time points in all samples, regardless of shRNA or HDAC inhibitor treatment.

In conclusion, the information obtained in these experiments indicates that HR was not fully compromised in cells treated with ATM shRNA, which agrees with the observation that residual ATM protein was detected in CII cells (fig. 9B). Significant reductions are observed only in early timepoints, and while an overall reduction in Rad51 positive cells was observed in ATM shRNA and/or vorinostat treated cells, the extent of reduction was not enough to indicate severely impaired HR mechanisms. These revelations also may explain why ATM knockdown cells were not increasingly sensitive to PARP and/or HDAC inhibition.

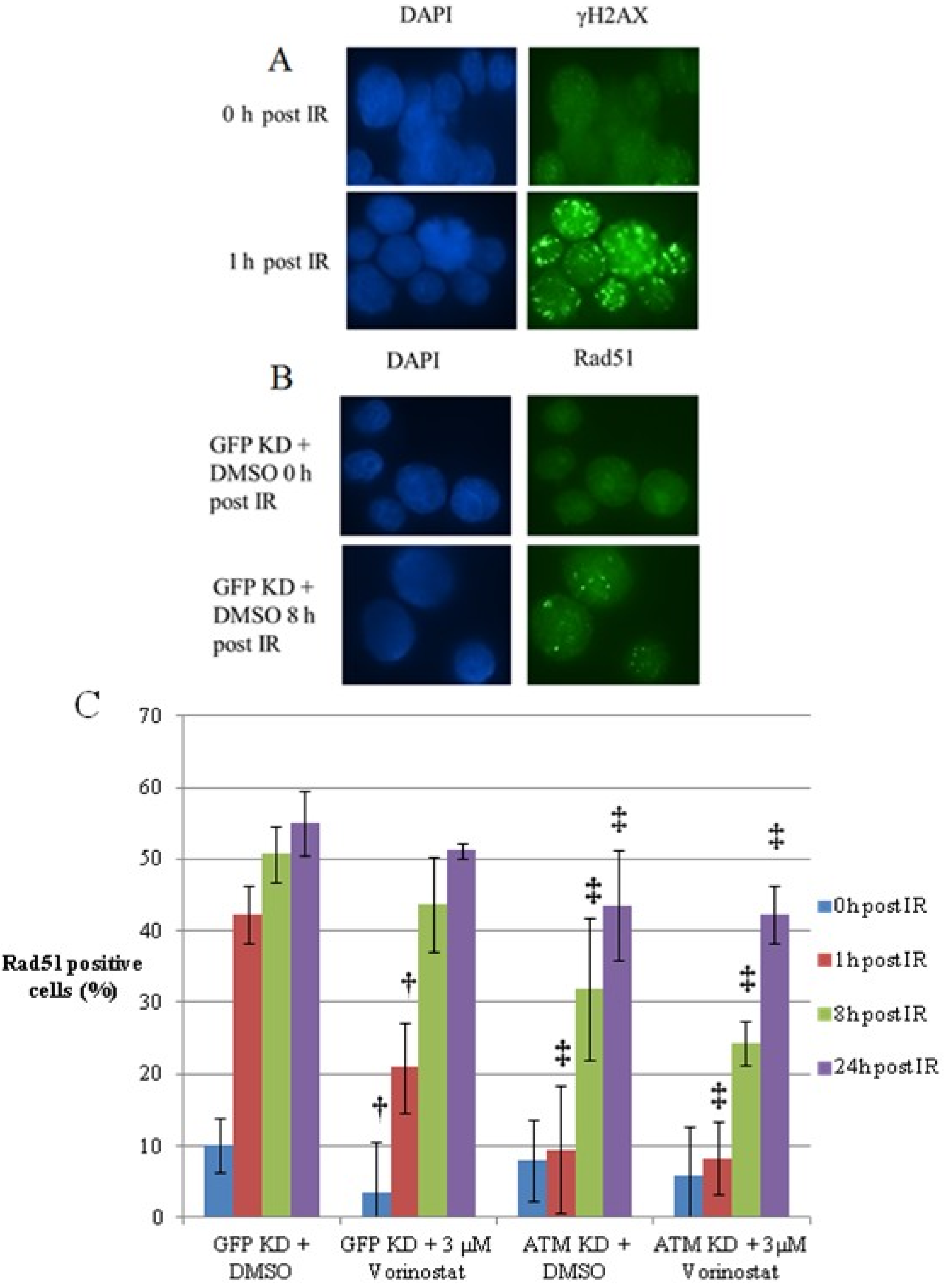

Figure 13 – The effects of ATM knockdown and HDAC inhibition on homologous recombination in CII cells. **A**. Example images of γH2AX staining for 0 and 1h post IR treatment. Strong γH2AX foci formation was observed at 1h post IR in samples indicating the presence of DSBs throughout cell sample populations. **B**. Example images of Rad51 negative (GFP KD + DMSO 0h post IR) and Rad51 positive (GFP KD + DMSO 8h post IR) cell nuclei. Note that RAD51 foci were morphologically smaller and fainter than γH2AX foci. **C**. Graph representing relative percentages of RAD51 positive cells across different IR timepoints in cell samples with varying ATM status and HDACi treatment. †= vorinostat treatment statistically significant compared to untreated cells of same timepoint (P=<0.01), ‡ = ATM deficient cells statistically significant relative to WT cells of same treatment and timepoint (P<0.01). Error bars represent the standard deviation of the mean.

4.0 Discussion

4.1 Hi-Res Melting as a mutation detection strategy

The study employed a novel method for detecting DNA sequence alterations, called Hi-Res Melting (see section 2.4). The method was advantageous to this study because it allowed rapid, high-throughput analysis of patient samples. Considerably more patient samples could be assessed for mutations in the time available in comparison to if each sample had been sequenced via the Sanger method. However, one downside of the method is that it only infers the possible presence of DNA sequence changes. The confirmation of any mutations present, and access to information concerning the nature and characteristics of any sequence changes, still requires the "flagged" samples to then be sequenced using traditional methods. Another potential downside is that there is a very small yet ever-present possibility that certain mutant samples may be erroneously classified as WT – some mutations may not cause changes in the DNA melting profile that are clear enough for the sample to be flagged as a potential variant. The identification of these variants is also very subjective and depends on the individual analysing the melting curve data, another potential error source. To be completely confident that all mutants had been detected in a cohort, all samples would still have to be sequenced via traditional methods. However, Hi-Res Melting is a highly cost-effective and time saving method for occasions where this is not feasible, such as if a cohort contains a very large number of samples.

In the context of this study, Hi-Res melting enabled the detection of the homozygous c.8786+8 A>C SNP in the PICCLE IM patient sample. Because this mutation was not reported to cause any splicing defects (Gumy-Pause et al., 2006; Meier et al., 2006), it was unlikely to have been detected through western blot analysis of the ATM protein product, or analysis of ATM mRNA via reverse transcriptase PCR (RT-PCR). There were, however, many false positives that appeared to have variant melting curves, but upon sequencing were revealed to be WT (fig. 8). This may have been caused by the presence of non-specific product generated by unclean PCR reactions, or due to the cohort being fairly small (28 samples). Due to the method relying on comparisons between individual samples to detect and isolate variants, false positives are less likely the larger the sample size, because negligible differences in WT melting curves would be less prominent.

Overall, Hi-Res Melting proved to be a useful tool in analysing ATM exon sequences quickly, but problems with PCR reaction optimisation were also encountered (see section 3.1). Due to time constraints, it was not possible to continue the optimisation process and complete the analysis of the cohort, and the overall aim of identifying any loss of function ATM mutants that could then be used in primary tumour cell cytotoxicity assays was not achieved. It was therefore decided that experiments to assess the synergic potential of PARPis and HDACis in ATM-deficient B-CLL would be carried out on isogenic B-CLL tumour cell lines treated with ATM shRNA to induce ATM knockdown, rather than ATM-null primary tumour samples.

4.2 PARP inhibition did not have a significant cytotoxic effect on CII and MEC-1 cells regardless of ATM status

Firstly, no significant difference in sensitivity to the PARP inhibitor olaparib was observed in cells of differing ATM status. This was in contrast with previous studies, and it was expected that ATM deficient tumour cells would show an increased sensitivity to PARP inhibition (Weston et al., 2010). In the CII cell line, olaparib treatment in both WT and ATM cells rarely produced a statistically significant cytotoxic effect at any dose, although a general trend of 10 μM olaparib having a slight killing effect was observed. However, at this high dose, off-target effects are not unlikely.

A possible explanation for this perceived resistance to olaparib was that the ATM knockdown of CII cells was shown to be incomplete; residual levels of ATM protein were detected via western blot staining (fig. 9B). Rad51 foci analysis also suggested that HR was still active in ATM shRNA treated CII cells (fig. 13C), also providing a possible explanation. However, MEC-1 cells displayed highly efficient ATM knockdown, with no ATM protein band visible (fig. 9B), and MEC-1 cells responded to olaparib even more unexpectedly than CII cells. In MEC-1 cells, olaparib had no cytotoxic effect at any concentration tested, and even produced a marginally positive effect on cell proliferation at higher concentrations. The fact that MEC-1 cells were p53 mutant could counter-intuitively contribute to this - there has been evidence of PARP1 inhibition causing medullablastomas in p53 $^{-/-}$ mice, implicating a tumour suppressive role for PARP1 in that particular cancer (Tong et al., 2003), thus it is not out of the question that this could happen in p53 mutant B-CLL. Indeed, disruption of DNA repair mechanisms leads to increased genomic instability, which is a leading cause of cancer in the first instance (Shaheen et al., 2011), and thus may lead to further oncogenic mutations and increased aggressiveness if DNA damage levels are not sufficient to lead to mitotic catastrophe. However, this is highly unlikely and has not been reported in progressive B-CLL. If cell viability loss was indeed through the accumulation of unrepaired DNA damage, p53 loss would have been expected to increase the cytotoxic effect of olaparib rather than oppose it due to further loss of cell cycle arrest mediators, especially because ATM and p53 have convergent roles (Stankovic et al., 2002b). Thus, more studies are required to clarify the underlying mechanisms of this apparent resistance to olaparib in p53 mutant cells.

4.3 ATM wild-type cells exhibited increased sensitivity to HDAC inhibitors

Both CII and MEC-1 cell lines were sensitive to the higher concentrations of HDAC inhibitors used. Unexpectedly however, in both cell lines, ATM wild type cells appeared to be more sensitive to HDACis than ATM knockdown cells. This effect was very unlikely to have been caused by the GFP shRNA negative control, because preliminary dose response optimisation experiments in untreated CII and MEC-1 cells showed almost identical patterns. There is evidence to suggest that HDAC inhibition can lead to p53 mediated apoptosis through DNA damage caused by reactive oxygen species (ROS) (Petruccelli et al., 2011; Wang et al., 2012) or p53 hyperacetylation (Oh et al., 2012). Thus, the ATM/p53 pathway may be responsible for HDAC induced killing through apoptotic mechanisms, and HDACis may induce more cell killing in WT cells with intact ATM/p53 pathways through apoptosis than in ATM deficient cells though the proposed theory of unrepaired DNA damage accumulation or autophagy - hence why WT CII cells displayed more sensitivity to HDAC inhibitors than ATM knockdown cells. This cannot explain the same phenomenon in the p53-mutant MEC-1 cells, however, which were also more sensitive overall to lower doses of HDACis to the point at which lower doses had to be used. Perhaps the loss of p53 function resulted in an even further loss of cell cycle regulation and DNA repair, thus more capacity to accumulate lethal levels of unrepaired DSBs. Since p53 and ATM have convergent roles (Stankovic et al., 2002b), this may also explain why MEC-1 ATM mutant cells were not preferentially sensitive to HDACis – the p53/ATM pathway was already impaired - although if this was the case, it would have been expected that MEC-1 cells would respond to olaparib treatment.

In CII cells, as the concentration of HDACi increased, the surviving fraction fell as was expected – HDAC inhibitors have been shown to decrease proliferation, and induce apoptosis and/or differentiation, as well as mediate the DNA damage response. Contrastingly, MEC-1 cells often showed dramatic increases in viable cell levels relative to the untreated controls, before sharply dropping off at marginally higher HDAC doses. This effect occurred regardless of ATM status, and was consistently observed throughout the experiments. The reasons as to why this occurred are unknown. One speculation might be that sublethal levels of HDAC inhibitor promotes euchromatin which is conducible to gene transcription and more accessible to transcription factors (Federico and Bagella, 2011), therefore possibly leading to upregulation of oncogenic cell proliferation genes in MEC-1 cells.

4.4 PARPi and HDACis did not selectively synergise in ATM knockdown CII cells

Based on recent findings (Weston et al., 2010), It was hypothesised that the PARP inhibitor olaparib would induce sensitivity to HDAC inhibitors in ATM mutant cells, through the accumulation of unrepaired SSBs that are converted to DSBs upon DNA replication, resulting in cell death through the accumulation of critical levels of unrepaired DSBs. However, it was not conclusively observed that ATM deficient cells were selectively sensitive to PARP and HDAC inhibition. Although WT cells were more sensitive to HDACi, both WT and ATM knockdown CII cells exhibited some PARPi and HDACi synergy at certain doses. PARPi and HDACi have been shown to induce apoptosis through DNA damage, and synergise accordingly in colon cancer cell lines (Adimoolam et al., 2007). ATM deficient cells are likely to have defective apoptotic responses to DNA damage due to an impaired p53/ATM pathway, a key reason as to why ATM or p53 null B-CLL is resistant to common therapies (Stankovic et al., 2004; Weston et al., 2010). It is therefore possible that PARPi and HDACi were indeed causing unrepaired DNA damage in both cell lines, but WT cells were being lost through apoptosis while the ATM-deficient cells were lost through other mechanisms such as mitotic catastrophe or autophagy-induced cell death, but to a lesser extent. More detailed studies into the mechanisms by which cell viability was being lost are required to either confirm or reject this speculation. However, the continued presence of Rad51 positive cells, as revealed by immunofluorescence, suggested against HR being fully compromised and indicated that DSB repair was still occurring, as is next explained.

4.5 Homologous recombination was still active in ATM KD CII cells

The addition of 3 μM vorinostat to WT cells lowered the amount of Rad51 positive cells across 24 hours, with a particularly prominent effect up to 1 hour after DSB occurrence. This is consistent with HDACs being required for HR (Robert et al., 2011). HDACs 9 and 10 are particularly important in HR (Kotian et al., 2011), which are targets of the pan-HDAC inhibitor vorinostat used in the experiment. The effects of vorinostat on ATM WT cells was very similar to the characteristics of untreated ATM KD cells, but was even more prominent. HDACs may be directly involved in HR (Robert et al., 2011) as previously discussed in section 1.9, explaining why HDAC inhibition resulted in a net reduction of Rad51-positive cells seen at early timepoints in WT cells. Vorinostat treated ATM deficient cells also showed a further loss of Rad51 positive cells across all timepoints relative to ATM deficient untreated cells. However, there was still a relatively high level of Rad51 positive cells even in ATM shRNA and HDACi treated samples, meaning that HR was impaired but still functional. This may explain why ATM deficient cells were less susceptible to HDAC inhibition – HR was still active and the cells were therefore not vulnerable to the inhibition of parallel DNA repair pathways.

4.6 Experimental shortfalls

There were a number of shortcomings to the cytotoxicity experiments. The main limitation to the study was that B-CLL cell lines were used rather than primary B-CLL tumour samples, and that stable ATM knockdowns were used rather than ATM mutants. The unavailability of ATM mutant primary tumour samples was unfortunate, as they constitute the best models for B-CLL cytotoxicity experiments *in vitro* and have been used in preceding studies (Weston et al., 2010). The experimental approach may have been compromised for a number of reasons:

a). Cell lines are known to acclimatise to specific cell culture conditions over time and behave differently to primary cells, thus, cell lines are not always an authentic representation of how primary tumours would be affected by cytotoxic drugs.

b). More specifically, the genes involved in the DDR are complex, involve much cross-talk and are often convergent and pleiotropic (Shaheen et al., 2011). Stably transfected ATM knockdown cells may have undergone the upregulation of redundant parallel pathways other than PARP and HDAC mediated mechanisms to compensate for the loss of ATM. The occurrence of this phenomenon becomes increasingly likely with time, as the cells undergo increasing rounds of replication and are passaged multiple times. This could have occurred in both CII and MEC-1 cells, explaining a lack of response to PARP and HDAC inhibition in ATM knockdown cells.

c). In CII cells, the ATM knockdown was incomplete and the residual ATM protein still present may have been enough for ATM-mediated HR. Indeed, knockdowns are not always the best approach for studying gene loss – it is not possible to achieve total knockout of the gene, and ATM$^{-/-}$ knockout cells may have been more suitable.

If cell lines are to be used again, the knockdown must be efficient. Inducible ATM knockdown systems might also be a better approach, because this would allow the comparison of the presence and absence of ATM in the same cells, maintaining exactly the same culture conditions. It would also restrict the potential ability of the cells to adapt to the loss of ATM and restore HR mechanisms through other mediators.

Another problem may lie with the fact that poly(ADP-ribosyl)ation and acetylation are such ubiquitous processes throughout cells (Smith and Workman, 2009). Thus, off-target effects independent of the DDR could not be discounted. For PARP activity, this was addressed by using only up to 10 μM olaparib because concentrations higher than 10 μM are significantly more likely to induce off-target effects (Weston et al., 2010). In this instance however, higher doses may have been suitable to use due to the lack of response to PARP inhibition, even if only to confirm that PARP inhibition could indeed cause a significant cytotoxic effect in the cell lines or not. As far as HDACis are concerned, around 85% of proteins are acetylated (Su et al., 2008), thus higher doses of HDAC inhibitor may have caused off-target effects that contributed to the cytotoxicity. From a clinical perspective, off-target effects are undesirable and lower drug tolerances. Detailed analysis of acetylome changes would be required to establish if off-target effects caused by HDAC inhibition were impacting on cell viability, as well as *in vivo* experiments to assess any potential side effects.

The cell viability assay that was used was also limiting in that it lysed the cells and only quantified the levels of ATP present as a measure of viable cells - no detailed information could be obtained as to the mechanisms of cytotoxicity, such as any cell cycle blocks, through induction of apoptosis, senescence, mitotic catastrophe or autophagy-related cell death. Thus, more detailed studies are required to establish the molecular mechanisms responsible for the results that were obtained. Additionally, the method of ATP quantification is not a completely faithful representation of viable cells, as cells will naturally vary in ATP levels, as well as between samples due to varying culture conditions. Additional cell viability quantification assays should therefore be carried out before any final conclusions are made, such as a manual cell counting method.

The immunofluorescence experiments also had a number of shortfalls. Due to time constraints, it was only possible to assess Rad51 mediated HR in one cell type, and more repeats of the same experiment would have to be performed to increase the reliability of the data obtained. Due to the aberrant responses to the drugs seen in MEC-1 cells, CII cells were used, but as aforementioned the ATM knockdown was not complete which may have impacted on the results. Had the time been available, HR in cells of differing treatment and ATM status would have been analysed in more detail, along with the impact of p53 loss on HR. Firstly, different variations of HDAC inhibitors and dose levels would have enabled a broader picture of the effects on HR. Assessing the effects of combined PARPis and HDACis on HR would also have provided useful information. It would have also been beneficial to visualise the effects of PARP inhibition on NHEJ mediators such as DNA-PKcs, which like Rad51 form foci at sites of DNA damage and thus their induction is quantifiable (Lou et al., 2004). Assessing the prevalence of Rad51/ γH2AX positive cells for longer times than 24 hours after IR might also be a viable study, because ATM has been implicated in absolving foci and resuming the cell cycle after HR is complete (Battu et al., 2011). Thus, loss of ATM could result in cellular senescence if the foci persist. Detailed cell cycle analysis would also reveal any cell cycle blocks that might be induced by PARP/HDAC inhibition.

4.7 Conclusions and future perspectives

The data observed in this study does not suggest that ATM deficient B-CLL cells are selectively sensitive to combined PARP and HDAC inhibition. Synergy was observed between PARP and HDAC inhibitors in B-CLL cell lines, although not significantly more so in ATM knockdown cells. Future work must be undertaken in primary tumour cells of differing ATM status for the most reliable results *in vitro*. Additionally, *in vivo* experiments are required to further validate the tumour killing effects of PARPi and HDACi combined therapies.

The fact that WT cells were seen to be more susceptible to HDAC inhibitors than ATM knockdown cells is not necessarily a negative observation from a clinical point of view, as this may indicate that HDAC inhibitors are good potential candidates for treating progressive B-CLL forms that are ATM WT. HDACis are generally well tolerated (Federico and Bagella, 2011), as are PARPis (Audeh et al., 2010; Vasiliou et al., 2009), which is a highly desirable trait for cancer therapeutics, particularly those which are likely to be administered to people of vulnerable age groups as in B-CLL. However, the mechanisms of HDACi cytotoxicity in B-CLL still need to be elucidated, and the observations may have been caused by off-target effects that may cause drug toxicity. Work must be done to establish effective dose tolerance levels, as well as the elimination of any potential off-target effects.

The development of both specific and potent treatments for progressive forms of B-CLL remains important, both to increase overall survival rates and the quality of life of patients, and despite the difficulties encountered during the study, the use of PARP and HDAC inhibitors in treating ATM-deficient B-CLL still remains a promising option. To unlock the potential of these compounds, more detailed studies are required into the tumour-killing effectiveness, the specificity to tumour cells and the specific molecular mechanisms by which the killing is achieved.

List of References

Adimoolam, S., Sirisawad, M., Chen, J., et al. (2007) HDAC inhibitor PCI-24781 decreases RAD51 expression and inhibits homologous recombination. **Proceedings of the National Academy of Sciences of the United States of America,** 104 (49): 19482-19487.

Alvi, A.J., Austen, B., Weston, V.J., et al. (2005) A novel CDK inhibitor, CYC202 (R-roscovitine), overcomes the defect in p53-dependent apoptosis in B-CLL by down-regulation of genes involved in transcription regulation and survival. **Blood,** 105 (11): 4484-4491.

Audeh, M.W., Carmichael, J., Penson, R.T., et al. (2010) Oral poly(ADP-ribose) polymerase inhibitor olaparib in patients with BRCA1 or BRCA2 mutations and recurrent ovarian cancer: a proof-of-concept trial. **Lancet,** 376 (9737): 245-251.

Austen, B., Powell, J., Alvi, A., et al. (2005) Mutations in the ATM gene lead to impaired overall and treatment-free survival that is independent of IGVH mutation status in patients with B-CLL. **Blood,** 106 (9): 3175-3182.

Austen, B., Skowronska, A., Baker, C., et al. (2007) Mutation status of the residual ATM allele is an important determinant of the cellular response to chemotherapy and survival in patients with chronic lymphocytic leukemia containing an 11q deletion. **Journal of Clinical Oncology,** 25 (34): 5448-5457.

Battu, A., Ray, A. and Wani, A.A. (2011) ASF1A and ATM regulate H3K56-mediated cell-cycle checkpoint recovery in response to UV irradiation. **Nucleic acids research,** 39 (18): 7931-7945.

Camphausen, K. and Tofilon, P.J. (2007) Inhibition of histone deacetylation: A strategy for tumor radiosensitization. **Journal of Clinical Oncology,** 25 (26): 4051-4056.

Chen, L.F., Fischle, W., Verdin, E., et al. (2001) Duration of nuclear NF-kappa B action regulated by reversible acetylation. **Science,** 293 (5535): 1653-1657.

Chiarugi, A. (2012) A snapshot of chemoresistance to PARP inhibitors. **Trends in pharmacological sciences,** 33 (1): 42-48.

Chiolo, I., Minoda, A., Colmenares, S.U., et al. (2011) Double-Strand Breaks in Heterochromatin Move Outside of a Dynamic HP1a Domain to Complete Recombinational Repair. **Cell,** 144 (5): 732-744.

Chiorazzi, N., Rai, K. and Ferrarini, M. (2005) Mechanisms of disease: Chronic lymphocytic leukemia. **New England Journal of Medicine,** 352 (8): 804-815.

Chowdhury, S., Howell, G.M., Teggart, C.A., et al. (2011) Histone Deacetylase Inhibitor Belinostat Represses Survivin Expression through Reactivation of Transforming Growth Factor beta (TGF beta) Receptor II Leading to Cancer Cell Death. **Journal of Biological Chemistry,** 286 (35): 30937-30948.

Corpet, A. and Almouzni, G. (2009) A histone code for the DNA damage response in mammalian cells? **Embo Journal,** 28 (13): 1828-1830.

Cortez, D., Wang, Y., Qin, J., et al. (1999) Requirement of ATM-dependent phosphorylation of brca1 in the DNA damage response to double-strand breaks. **Science (New York, N.Y.),** 286 (5442): 1162-1166.

Cramer, P. and Hallek, M. (2011) Prognostic factors in chronic lymphocytic leukemia-what do we need to know? **Nature Reviews Clinical Oncology,** 8 (1): 38-47.

Damle, R., Wasil, T., Fais, F., et al. (1999) Ig V gene mutation status and CD38 expression as novel prognostic indicators in chronic lymphocytic leukemia. **Blood,** 94 (6): 1840-1847.

Dohner, H., Fischer, K., Bentz, M., et al. (1995) P53 Gene Deletion Predicts for Poor Survival and Nonresponse to Therapy with Purine Analogs in Chronic B-Cell Leukemias. **Blood,** 85 (6): 1580-1589.

Dumitriu, I.E., Voll, R.E., Kolowos, W., et al. (2004) UV irradiation inhibits ABC transporters via generation of ADP-ribose by concerted action of poly(ADP-ribose) polymerase-1 and glycohydrolase. **Cell death and differentiation,** 11 (3): 314-320.

Edwards, S.L., Brough, R., Lord, C.J., et al. (2008) Resistance to therapy caused by intragenic deletion in BRCA2. **Nature,** 451 (7182): 1111-1115.

Ellis, L. and Pili, R. (2010) Histone Deacetylase Inhibitors: Advancing Therapeutic Strategies in Hematological and Solid Malignancies. **Pharmaceuticals (Basel, Switzerland),** 3 (8): 2411-2469.

Federico, M. and Bagella, L. (2011) Histone deacetylase inhibitors in the treatment of hematological malignancies and solid tumors. **Journal of biomedicine & biotechnology,** 2011 475641.

Fong, P.C., Yap, T.A., Boss, D.S., et al. (2010) Poly(ADP)-Ribose Polymerase Inhibition: Frequent Durable Responses in BRCA Carrier Ovarian Cancer Correlating With Platinum-Free Interval. **Journal of Clinical Oncology,** 28 (15): 2512-2519.

Friedman, D.F., Moore, J.S., Erikson, J., et al. (1992) Variable Region Gene Analysis of an Isotype-Switched (Iga) Variant of Chronic Lymphocytic-Leukemia. **Blood,** 80 (9): 2287-2297.

Fu, J., Shao, C., Chen, F., et al. (2010) Autophagy induced by valproic acid is associated with oxidative stress in glioma cell lines. **Neuro-oncology,** 12 (4): 328-340.

Groth, A., Rocha, W., Verreault, A., et al. (2007) Chromatin challenges during DNA replication and repair. **Cell,** 128 (4): 721-733.

Gu, W. and Roeder, R.G. (1997) Activation of p53 sequence-specific DNA binding by acetylation of the p53 C-terminal domain. **Cell,** 90 (4): 595-606.

Gumy-Pause, F., Wacker, P., Maillet, P., et al. (2006) ATM variants and predisposition to childhood T-lineage acute lymphoblastic leukaemia. **Leukemia,** 20 (3): 526-527.

Hamblin, T.J., Davis, Z., Gardiner, A., et al. (1999) Unmutated Ig V-H genes are associated with a more aggressive form of chronic lymphocytic leukemia. **Blood,** 94 (6): 1848-1854.

Helleday, T., Petermann, E., Lundin, C., et al. (2008) DNA repair pathways as targets for cancer therapy. **Nature Reviews Cancer,** 8 (3): 193-204.

Jang, E.R., Choi, J.D., Park, M.A., et al. (2010) ATM modulates transcription in response to histone deacetylase inhibition as part of its DNA damage response. **Experimental and Molecular Medicine,** 42 (3): 195-204.

Jurkin, J., Zupkovitz, G., Lagger, S., et al. (2011) Distinct and redundant functions of histone deacetylases HDAC1 and HDAC2 in proliferation and tumorigenesis. **Cell Cycle,** 10 (3): 406-412.

Kotian, S., Liyanarachchi, S., Zelent, A., et al. (2011) Histone Deacetylases 9 and 10 Are Required for Homologous Recombination. **Journal of Biological Chemistry,** 286 (10): 7722-7726.

Lagace, D.C. and Nachtigal, M.W. (2004) Inhibition of histone deacetylase activity by valproic acid blocks adipogenesis. **Journal of Biological Chemistry,** 279 (18): 18851-18860.

Lavin, L. and Khanna, K. (1999) Review: ATM: the protein encoded by the gene mutated in the radiosensitive syndrome ataxia-telangiectasia. **International journal of radiation biology,** 75 (10): 1201-1214.

Lou, Z.K., Chen, B.P.C., Asaithamby, A., et al. (2004) MDC1 regulates DNA-PK autophosphorylation in response to DNA damage. **Journal of Biological Chemistry,** 279 (45): 46359-46362.

Maddocks, K.J. and Lin, T.S. (2009) Update in the management of chronic lymphocytic leukemia. **Journal of Hematology & Oncology,** 2 29.

Marks, P.A., Richon, V.M. and Rifkind, R.A. (2000) Histone deacetylase inhibitors: Inducers of differentiation or apoptosis of transformed cells. **Journal of the National Cancer Institute,** 92 (15): 1210-1216.

Marks, P.A. and Breslow, R. (2007) Dimethyl sulfoxide to vorinostat: Development of this histone deacetylase inhibitor as an anticancer drug. **Nature biotechnology,** 25 (1): 84-90.

Martinez-Balbas, M.A., Bauer, U.M., Nielsen, S.J., et al. (2000) Regulation of E2F1 activity by acetylation. **Embo Journal,** 19 (4): 662-671.

Matsushita, H., Scaglioni, P., Bhaumik, M., et al. (2006) In vivo analysis of the role of aberrant histone deacetylase recruitment and RAR alpha blockade in the pathogenesis of acute promyelocytic leukemia. **Journal of Experimental Medicine,** 203 (4): 821-828.

Meier, M., den Boer, M.L., Hall, A.G., et al. (2006) Reply to 'ATM variants and predisposition to childhood T-lineage acute lymphoblastic leukaemia' by Gumy-Pause et al. **Leukemia,** 20 (3): 527-527.

Miller, K.M., Tjeertes, J.V., Coates, J., et al. (2010) Human HDAC1 and HDAC2 function in the DNA-damage response to promote DNA nonhomologous end-joining. **Nature Structural & Molecular Biology,** 17 (9): 1144-U15.

Nebbioso, A., Clarke, N., Voltz, E., et al. (2005) Tumor-selective action of HDAC inhibitors involves TRAIL induction in acute myeloid leukemia cells. **Nature medicine,** 11 (1): 77-84.

Oh, E., Park, M., Choi, B., et al. (2012) Novel histone deacetylase inhibitor CG200745 induces clonogenic cell death by modulating acetylation of p53 in cancer cells. **Investigational new drugs,** 30 (2): 435-442.

Patel, J.H., Du, Y.P., Ard, P.G., et al. (2004) The c-MYC oncoprotein is a substrate of the acetyltransferases hGCN5/PCAF and TIP60. **Molecular and cellular biology,** 24 (24): 10826-10834.

Pepper, C., Lin, T.T., Pratt, G., et al. (2008) Mcl-1 expression has in vitro and in vivo significance in chronic lymphocytic leukemia and is associated with other poor prognostic markers. **Blood,** 112 (9): 3807-3817.

Petruccelli, L.A., Dupere-Richer, D., Pettersson, F., et al. (2011) Vorinostat Induces Reactive Oxygen Species and DNA Damage in Acute Myeloid Leukemia Cells. **Plos One,** 6 (6): e20987.

Pettitt, A. (2003) Mechanism of action of purine analogues in chronic lymphocytic leukaemia. **British journal of haematology,** 121 (5): 692-702.

Pittner, B.T., Shanafelt, T.D., Kay, N.E., et al. (2005) CD38 expression levels in chronic lymphocytic leukemia B cells are associated with activation marker expression and differential responses to interferon stimulation. **Leukemia,** 19 (12): 2264-2272.

Pratt, G. (2011) **A trial looking at a new drug called olaparib for leukaemia and mantle cell lymphoma that has stopped responding to treatment (PICLLE).** [Online]. Available from: http://cancerhelp.cancerresearchuk.org/trials/a-trial-looking-new-drug-olaparib-leukaemia-mantle-cell-lymphoma-that-has-stopped-responding-treatment-piclle [Accessed February 08 2012].

Riballo, E., Kuhne, M., Rief, N., et al. (2004) A pathway of double-strand break rejoining dependent upon ATM, Artemis, and proteins locating to gamma-H2AX foci. **Molecular cell,** 16 (5): 715-724.

Richon, V., Sandhoff, T., Rifkind, R., et al. (2000) Histone deacetylase inhibitor selectively induces p21(WAF1) expression and gene-associated histone acetylation. **Proceedings of the National Academy of Sciences of the United States of America,** 97 (18): 10014-10019.

Robert, T., Vanoli, F., Chiolo, I., et al. (2011) HDACs link the DNA damage response, processing of double-strand breaks and autophagy. **Nature,** 471 (7336): 74-79.

Rottenberg, S., Jaspers, J.E., Kersbergen, A., et al. (2008) High sensitivity of BRCA1-deficient mammary tumors to the PARP inhibitor AZD2281 alone and in combination with platinum drugs. **Proceedings of the National Academy of Sciences of the United States of America,** 105 (44): 17079-17084.

Savitsky, K., Barshira, A., Gilad, S., et al. (1995) A Single Ataxia-Telangiectasia Gene with a Product Similar to Pi-3 Kinase. **Science,** 268 (5218): 1749-1753.

Shaheen, M., Allen, C., Nickoloff, J.A., et al. (2011) Synthetic lethality: exploiting the addiction of cancer to DNA repair. **Blood,** 117 (23): 6074-6082.

Skowronska, A., Austen, B., Powell, J.E., et al. (2012) ATM germline heterozygosity does not play a role in chronic lymphocytic leukemia initiation but influences rapid disease progression through loss of the remaining ATM allele. **Haematologica,** 97 (1): 142-146.

Smith, K.T. and Workman, J.L. (2009) Introducing the acetylome. **Nature biotechnology,** 27 (10): 917-919.

Stankovic, T., Hubank, M., Cronin, D., et al. (2004) Microarray analysis reveals that *TP53*- and ATM-mutant B-CLLs share a defect in activating proapoptotic responses after DNA damage but are distinguished by major differences in activating prosurvival responses. **Blood,** 103 (1): 291-300.

Stankovic, T., Stewart, G., Byrd, P., et al. (2002a) ATM mutations in sporadic lymphoid tumours. **Leukemia & lymphoma,** 43 (8): 1563-1571.

Stankovic, T., Stewart, G., Fegan, C., et al. (2002b) Ataxia telangiectasia mutated-deficient B-cell chronic lymphocytic leukemia occurs in pregerminal center cells and results in defective damage response and unrepaired chromosome damage. **Blood,** 99 (1): 300-309.

Starczynski, J., Simmons, W., Flavell, J., et al. (2003) Variations in ATM protein expression during normal lymphoid differentiation and among B-cell-derived neoplasias. **American Journal of Pathology,** 163 (2): 423-432.

Su, H., Altucci, L. and You, Q. (2008) Competitive or noncompetitive, that's the question: research toward histone deacetylase inhibitors. **Molecular Cancer Therapeutics,** 7 (5): 1007-1012.

Tan, J., Zhao, Y., Zhuang, L., et al. (2005) C7 inhibitors of histone deacetylases target Rb-E2F1 pathway for apoptosis induction through activation of proapoptotic protein Bim. **Clinical Cancer Research,** 11 (24): 9101S-9101S.

Taylor, A., Harcourt, S., Lehmann, A., et al. (1975) Ataxia Telangiectasia - Human Mutation with Abnormal Radiation Sensitivity. **Nature,** 258 (5534): 427-429.

Tjeertes, J.V., Miller, K.M. and Jackson, S.P. (2009) Screen for DNA-damage-responsive histone modifications identifies H3K9Ac and H3K56Ac in human cells. **Embo Journal,** 28 (13): 1878-1889.

Tong, W.M., Ohgaki, H., Huang, H.T., et al. (2003) Null mutation of DNA strand break-binding molecule poly(ADP-ribose) polymerase causes medulloblastomas in p53(-/-) mice. **American Journal of Pathology,** 162 (1): 343-352.

Ure, U., Ar, M.C., Baslar, Z., et al. (2009) The Effect of ZAP-70 Expression on Disease Progression in Early-Stage (Binet A) B-CLL Patients. **Trakya Universitesi Tip Fakultesi Dergisi,** 26 (4): 317-321.

Vasiliou, S., Castaner, R. and Bolos, J. (2009) Olaparib. PARP-1 and PARP-2 inhibitor, Oncolytic. **Drugs of the Future,** 34 (2): 101-105.

Wang, H.Y., Wang, M.L., Wang, H.C., et al. (2005) Complex H2AX phosphorylation patterns by multiple kinases including ATM and DNA-PK in human cells exposed to ionizing radiation and treated with kinase inhibitors. **Journal of cellular physiology,** 202 (2): 492-502.

Wang, H., Zhou, W., Zheng, Z., et al. (2012) The HDAC inhibitor depsipeptide transactivates the p53/p21 pathway by inducing DNA damage. **DNA repair,** 11 (2): 146-156.

Wang, M., Wu, W., Wu, W., et al. (2006) PARP-1 and Ku compete for repair of DNA double strand breaks by distinct NHEJ pathways. **Nucleic acids research,** 34 (21): 6170-6182.

Weston, V.J., Oldreive, C.E., Skowronska, A., et al. (2010) The PARP inhibitor olaparib induces significant killing of ATM-deficient lymphoid tumor cells in vitro and in vivo. **Blood,** 116 (22): 4578-4587.

Woodhouse, B.C. and Dianov, G.L. (2008) Poly ADP-ribose polymerase-1: An international molecule of mystery. **DNA Repair,** 7 (7): 1077-1086.

Wurzer, G., Herceg, Z. and Wesierska-Gadek, J. (2000) Increased resistance to anticancer therapy of mouse cells lacking the poly(ADP-ribose) polymerase attributable to up-regulation of the multidrug resistance gene product P-glycoprotein. **Cancer research,** 60 (15): 4238-4244.

Yap, T.A., Sandhu, S.K., Carden, C.P., et al. (2011) Poly(ADP-Ribose) Polymerase (PARP) Inhibitors: Exploiting a Synthetic Lethal Strategy in the Clinic. **Ca-a Cancer Journal for Clinicians,** 61 (1): 31-49.

Yuan, J., Pu, M., Zhang, Z., et al. (2009) Histone H3-K56 acetylation is important for genomic stability in mammals. **Cell Cycle,** 8 (11): 1747-1753.

Yuan, S., Chang, H. and Lee, E. (2003) Ionizing radiation-induced Rad51 nuclear focus formation is cell cycle-regulated and defective in both ATM(-/-) and c-Abl(-/-) cells. **Mutation Research-Fundamental and Molecular Mechanisms of Mutagenesis,** 525 (1-2): 85-92.

Zhou, J., Lim, C.U.K., Li, J.J., et al. (2006) The role of NBS1 in the modulation of PIKK family proteins ATM and ATR in the cellular response to DNA damage. **Cancer letters,** 243 (1): 9-15.

Appendix

Exon	Original Primer Sequence (5' - 3')	Original Optimum Tm (^oC)	New Sequence	New Optimum Tm (^oC)
4F	CACACCTCTTTCTCTCTATATATGC	61		
4R	ATTTCAAGGAAAAATTGAATTTAAG		GGAAAAATTGAATTTAAGTAATTTACTAC	
5F	TGATTAGTAACCCATTATTATTTC	61		
5R	GGAAGCAAAGATAAATGTTAAGACTTACAC		AATAAAGACAGTAAAATAAATTTGAATAG	
6F	ATTGGTCTTGTAGGAGTTAGGCCTTG	65		
6R	AAAAACTCACGCGACAGTAATCTG			
7F	TAAATAGTTGCCATTCCAAGTGTC	65		
7R	TGGTGAAGTTTCATTTCATGAGG			
8F	CCTTTTTCTGTATGGGATTATGGA	62		
8R	TACTGAGTCTAAAACATGGTCTTGC			
9F	TTCTTTCAGCATACCACTTCATAAC	60		
9R	TGAATGAAGAAGCAAATTCAAAACAG			
10F	TGGGAGCTAGCAGTGTAAACAGAG	65		
10R	CAGGAAATTTCTAAATGTGACATGAC			
11F	GCTCAAAAAAAAAAAAAAGAAAAAAGTGG	65		
11R	AAATGACTTAGTTCTGGTTGAGATG			
12F	TCCTTTTAGTTTGTTAATGTGATGG	61		
12R	ACTATGAAAATGATCAGGGATATG			
13F	CCTCCAATAGCTTGCTTTTCAC	64	CGAGCTATTTTTTTAATCAAGAATCTTCC	
13R	AAACAGCAGCATGCTAATGAAC		CAATCAGGCATAAAGACACAGATAAC	
14F	GTATTCTTTACATGGCTTTTGGTC	62		
14R	TACTACCCAGCTAAAATTATCATC			
15F	CATATAAGGCCAAAGCATTAGGT	61		
15R	CCTATTTCTCCTTCCTAACAGT			
16F	GAATTTGTTCTTACAAAAGATAGAG	60		
16R	GAATACATTTCATTCAAATTTATCCGA			
17F	GTATGTCCAAGATCAAAGTACACTG	64	CTCTTGGTAGTACTCTGTCACTGGTATG	
17R	GGGTGACAGAGAAAGATCCTATC		GGATATTACCTTTATGTACCATTCAACT	
18F	GTTTTTATTTCTTTGTTGCTTGGTTCT	65	CTCTAAGAAAAGATGTGTTTTTGAAGCAG	60
18R	CAAAATATGATAGCAAAACAGGAAGC		AGAGCTATATGTTGTGAGATGCATCC	

Exon	Original Primer Sequence (5' - 3')	Original Optimum Tm (^{o}C)	New Sequence	New Optimum Tm (^{o}C)
19F	CTCCCAAATTGCTGAGATTACAGATG	65		
19R	ATGAGGCCTCTTATACTGCCAAATC			
20F	ATATATGGCTGTTGTGCCCTTCTC	60	ATTATTTCTTGACAACAGAATCTTGG	62
20R	CATCAGATAAAATCCAAGAGCTTC		AAATTTGCTCACAGCACGTTAAAAGTG	
21F	AAACCTGATTTTTTCCCTCCTAC	60		
21R	TTTATAAGCTTAACAGAACAGAACACATCAGT			
22F	AATAACTGATGTGTTCTGTTAAGC	60		60
22R	AAACTTGCATTCGTATCCACAGAT		GGAAGATCAGAAGAAATCACTGATG	
23F	GTAACTTATAATAACCTTTCAGTGAG	60	AGCACAGAAAGACATATTGGAAG	60
23R	ACTCATTAACAAACAAAGACTGCT		GTAACTTATAATAACCTTTCAGTGAG	
24F	CTATTTCATATTTAACCACAGTTC	60		
24R	TATGTAAGACATTCTACTGCCATC			
25F	TTGTTTGTTTGTTTGCTTGCTTGTTT	60	GTTCTGGAATATGCTTTGGAAG	60
25R	CATATGATAACAGCAAATACATGTTAC		GTCCAATGTTCCCTTAATTAGC	
26F	GTCAAAAAATCTGGAGTTCAGTTG	65		
26R	GGAAGCTTCTAATAAAATACTCATC		ATACTATTTCCAAAAGCCTGGTCAGTC	
27F	GAATGTTGTTTCTAGGTCCTACTC	62		
27R	GTGAGGGGACTTGCTAAGTATTG			
28F	CTTGGAAAAGTTATATATAACCTG	60		
28R	AACTTAAAGGTTATATCTCATATC			
29F	TTTGAGCTGTCTTGACGTTCACAG	61		
29R	TTGAAATAGACATTGAAGGTGTCAAC			
30F	TTTTCATTTTGGAAGTTCACTGGTC	61		
30R	GGAATGTTCTATTATTAAACTCATC			
31F	GTGTATTTATTGTAGCCGAGTATC	65		
31R	GGAAGAACAGGATAGAAAGACTGC			
32F	GACTTCTGAATGAATTTATTTCAGAG	60		
32R	CACTCAAATCCTCTAACAATAC		AAAATCACCAATTATACCAAA	
33F	TTACAGTAAGTTTTGTTGGCTTAC	61		
33R	CAGATTTTTGAAAAGTACTACTATG			
34F	CCAATACGTGTTAAAAGCAAGTTAC	60	GATTAGTAGTAATAGAGACATGAGTCAG	61
34R	AACAGGTAGAAATAGCCCATGTC		CTGAACTAAATGATGAGAGTCTGAAC	
35F	AAACAAAAGTGTTGTCTTCATGCT	64	CTCTGTTGTCACATATTGCTAATCAC	62
35R	TCCTATATGTGATCCGCAGTTGAC		ACTACACACCTAGGCTACAAACCTG	
36F	GTTTTATGTATGATCTCTTACCTATG	60		
36R	GAAGTATCATTCTCCATGAATGTC			

Exon	**Original Primer Sequence (5' - 3')**	**Original Optimum Tm (°C)**	**New Sequence**	**New Optimum Tm (°C)**
37F 37R	CAGTGGAGGTTAACATTCATCAAG ACAGTCATGACCCACAGCAAACAG	65		
38F 38R	AAGGTACAATGATTTCCACTTCTC CAGCACTCTTTAGATAAACAGGTC	65		
39F 39R	AGCAGTATGTTGAGTTTATGGCAG GGATTCCATCTTAAATCCATCTTTC	65		
40F 40R	CCTTATAGCATAGTGGGAGACAG CAAGTTACACTCTAGATCCTAAACG	65		
41F 41R	TAAGCAGTCACTACCATTGTATTC TACCCTTATTGAGACAATGCCAAC	65		
42F 42R	CAGGAGCTTCCAAATAGTATGTTC CACATGGCATCTGTACAGTGTCT	65		
43+44F 43+44R	TAGAGTTGGGAGTTACATATTGGT GCACTACACTAGTGATGGCTTTAC	63		
45F 45R	GGTTTCTGTTGATATCTTTGATTAC GAGAGGCAAAAAAAAAAAAATCAAGTC	62		
46F 46R	GTCCTTTGGTGAAGCTATTTATAC CTCAAGTTTTCAGAAAAGAAGCCA	65		
47F 47R	CCTCTTCTTTATTTTCAGAGTGTC GTCACTATTGGTAACAGAAAAGC	61		
48F 48R	CATTTCTCTTGCTTACATGAACTC TAGAGATCTCTATCTCTTAATGAC	62		
49F 49R	CATGGTAGTAGTATCAGTAGTAAAAG CAGTAAAACACTAATCCAGCCAAT	62	GAGATGTCATGCAGACAGAGAGGTCC GAATCGACCACATGATGGACTGATAG	
50F 50R	AGTTGGGTACAGTCATGGTAATGC CTAAGTAACTATCTTAAGGGTTGCTC	63		
51F 51R	GTGTATTACCTAATTTGAGTGATTC AAGACCAAGTCACTCTTTCTATGC	63		
52F 52R	ATCATGTGTGATTTTGTAGTTCTG TTCAAGCACAGGGTAGAATATTGG	65		
53F 53R	TTGTGCTAATAGAGGAGCACTGTC GTATTTCCATTTCTTAGAGGGAATG	63		
54F 54R	TCTACCCACTGCAGTATCTAGAC CAGCCTTGAACCGATTTTAGATG	65		
55F 55R	TGTTGGGTAGTTCCTTATGTAATG GGATTACGTTTGTGATTTTAAGCAG	64	GAAAGGCACCTAAGTCATTGACGAG CTCTGTAATAAGTATGTATGCCAGAAG	

Exon	Original Primer Sequence (5' - 3')	Original Optimum Tm (°C)	New Sequence	New Optimum Tm (°C)
56F	ACTATTCCTGCTTGACCTTCAATG	61	CTTTGACTCTGAGCTGCATAGT	
56R	GCCAATATTTAACCAATTTTGACC			
57F	TAAGTGCAAATAGTGTATCTGACC	65	GCCTAAAGTTGTAGTTCTTAACCAC	
57R	CATCACTAAAACTCTAAGGGCTAAG		GCATTTCTACTCTACAAATCTTCCTC	
58F	TTGCTATTCTCAGATGACTCTGTG	61		
58R	GCCTCCCAAAGCATTATGAATATG			
59F	CATCAAATGCTCTTTAATGGCCTT	63	GAGCTTTGTCTTCTATGGACAGAG	
59R	CTATAATATCTGACAGCTGTCAGCT		CATTTCTTATCTGACAAGGGTTGAC	
60F	CATCTTTATTGCCCCTATATCTGTC	62		
60R	TGCCAAACAACAAAGTGCTCAATC			
61F	AAGAGATGGAATCAGTGATTTCAG	62		
61R	AGGCAAACAACATTCCATGATGAC			
62F	TTAGCTGTCAAACCTCCTAACTTC	64		
62R	TTGAGTAGCTGGGATTACAGGTG			
63F	AGATATGTTGACAACATGGTGTG	65	GTCTAATGAAAGCCCACTCTGCCA	62
63R	GAGATACACAGTCTACCTGGTAAG		TGTGTGAAAAGGCTAAGTGCACAA	
64F	GATACTGGTTCTACTGTTTCTAAG	64		
64R	AAAGGTTTCAGTGAGGTGAACAG			
65F	GGTGAGCAGTATTTTAAGAAGGTC	64		
65R	TCCCTACTTAAAGTATGTTGGCAG			

Table S1 - All ATM primers used in the study, with re-optimised temperatures included.

Characteristic	**CII**	**MEC-1**
Ig Production	IgM, λ	NT
IGH genes	IGHV1-69UM/IGHD3-10/IGHJ6	IGHV4-59M/IGHD2-21/IGHJ4
IGK/IGL genes	IGLV1-4	NT
FISH data	Trisomy/tetrasomy 12 + tetrasomy 11q/13q/17p	NT
CD38 (% pos. cells)	69	40
CD38 (MFI fold-increase)	12.1	6.8
ZAP70 (% pos. cells)	83	2
ZAP70 (MFI fold-increase)	5, 8	1.1
TCL1 (%pos cells/MFI)	74%/3.6	71%/4.8
TCL1 (Western Blot/RT-PCR)	+	(+)
TP53 Status	Wild Type	Mutant

Table S2 - Characteristics of CII and MEC-1 isogenic B-CLL cell lines. NT = not tested. CD38 and ZAP70 % positive cells were calculated according to a 30% cut-off. Fold increase of MFI was calculated and considered positive at the following limits: >2.5 fold for ZAP70 and >3.5 fold for TCL1.

shRNA Target	**Sequence**
ATM-1 (7218)	5'-GATCCCCCTGGTTAGCAGAAACGTGCTTCAAGAGAGCACGTTTCTGCTAACCAGTTTTTA-3' 3'-GGGGACCAATCGTCTTTGCACGAAGTTCTCTCGTGCAAAGACGATTGGTCAAAAATTCGA-5'
ATM-II (P480)	5'-GATCCCCGATACCAGATCCTTGGAGATTCAAGAGATCTCCAAGGATCTGGTATCTTTTTA-3' 3'-GGGCTATGGTCTAGGAACCTCTAAGTTCTCTAGAGGTTCCTAGACCATAGAAAAATTCGA-5'
GFP shRNA Control	5'-GATCCCCCGTACGCGGAATACTTCGATTCAAGAGATCGAAGTATTCCGCGTACGTTTTTA-3' 3'-GGGGCATGCGCCTTATGAAGCTAAGTTCTCTAGCTTCATAAGGCGCATGCAAAAATCGA-5'

Table S3 - shRNA oligonucleotides used for stable ATM and GFP negative control knockdowns. Two ATM shRNA oligonucleotides were transfected simultaneously to increase the efficiency of the knockdown. Note that the knockdown experiments were performed prior to this study and the sequences are included for completeness.

University of Birmingham

School of Biosciences

Optimisation of Multiple Marker Imaging of Immunological Tissue Using Confocal Laser Scanning Fluorescence Microscopy

A research project report submitted by

David Michael Cartwright

as part of the requirement for the

degree of MRes in Molecular and Cellular Biology

This project was carried out at: Biosciences Building, University of Birmingham

Under the supervision of: Dr. Joshua Z. Rappoport/Prof. Christopher M. Bunce

Date: 23rd July 2012

Abstract

The simultaneous imaging of multiple biomarkers within tissues is of high value to both experimental and diagnostic histopathology, because it allows for analysis of the spatial and temporal relationships of specific molecules, cell populations and tissue components. Immunofluorescence (IF) is a highly applicable technique for sample multilabelling, but intrinsic pitfalls such as low fluorophore brightness and photostability, tissue autofluorescence and spectral bleedthrough can limit the viability of IF in a histopathological context. This study has optimised a multiple marker imaging method using indirect IF and confocal laser scanning microscopy (CLSM) to simultaneously image three separate B-lymphocyte markers of CD19, κ- and λ- immunoglobulin light chain antigens alongside a nuclear counterstain in reactive lymph node cryosections. Building on preliminary experiments which used older generation fluorophores, a staining and imaging protocol utilising the more photostable Alexa fluorophores was optimised. Secondary antibody dilutions of Alexa 488, 568 and 647 which produced maximum signal and minimum nonspecific fluorophore binding were determined. In addition, microscope imaging settings were established that minimised tissue autofluorescence, spectral bleedthrough and an optimal signal/noise ratio. This imaging method could be applied in a clinical context for immunophenotyping and identifying B-lymphocyte populations with abnormally skewed κ/λ ratios within lymph nodes, an indicator of monoclonality and potential neoplasia. Future studies will continually develop this imaging method for different immunological antigens for potential use in diagnostic and prognostic histopathology of lymphomas and lymphatic leukaemias, and for research towards cancer therapies targeting the specific molecular mechanisms of tumourigenesis.

List of Abbreviations

CLSM	Confocal laser-scanning microscopy
DAPI	4',6-diamidino-2-phenylindole
FFPE	Formalin-fixed paraffin embedded
FITC	Fluorescein isothiocyanate
IF	Immunofluorescence
Ig	Immunoglobulin
IHC	Immunohistochemistry
PBS	Phosphate buffered saline
PMT	Photomultiplier tube
TRITC	Tetramethyl rhodamine iso-thiocyanate

1.0 Introduction

1.1 The importance of monitoring specific markers in histology

Histology is defined as the study of tissues, and is an essential tool in many areas of biomedical research and medicine. In medicine, histology is often used for the acquisition of diagnostic and prognostic information through the study of diseased tissues, a field defined as histopathology. Traditional histological methodology commonly involves light or electron microscopy in combination with biological staining methods to resolve morphological and cytological details (Mahon, 2011). However, as more progress is made on elucidating the molecular mechanisms of disease, it is often necessary to visualise and/or quantify the expression of specific proteins within tissues (Mahon, 2011). Using cancer as an example, patients diagnosed with the same form of cancer and the same histopathologically defined disease stage often have largely differing prognoses due to differing underlying molecular mechanisms of the disease. Some examples of surface markers implicated as indicators of poor disease prognosis include the presence of CD44 in colorectal cancer (Belov et al., 2011), CD38 and CD49d in chronic lymphocytic leukaemia (CLL) (Del Poeta et al., 2001) or HER2 in breast cancer (Qui Wen-sheng et al., 2009). The treatment of certain molecularly defined cancer forms must often take alternative approaches, such as early surgery or more aggressive courses of chemotherapy and radiotherapy, to ensure the best possible chance of remission and patient survival (Li et al., 2010).

As the understanding of the molecular mechanisms of cancer increases, the identification of such markers may also open up new more effective and less toxic personalised treatment options that specifically target the marker molecule itself, or downstream effectors of the signalling pathways it mediates (Sawyers, 2004). Thus, the monitoring of specific markers is important for both biomedical research to develop such drugs, and from a clinical histopathology context to identify forms of disease eligible for such treatment.

The most common histological methods to identify specific molecules involve immunophenotyping via immunohistochemistry (IHC). IHC is defined as the process of detecting antigens in tissues via the use of antibodies specific to the antigen of interest (Key, 2009; Renshaw, 2005). The two most widely used IHC methods are enzyme-based IHC and immunofluorescence (IF) (Renshaw, 2005).

1.2 Commonly used histological methods for analysing expression of specific markers

Enzyme/substrate based IHC is the most common method used in both research and diagnostic histopathology, the basis of which is to produce staining localised to areas of tissue expressing a specific antigen via the catalysis of a reaction involving a subsequently added colourless chromogenic substrate, which produces a dye compound (Key, 2009; Renshaw, 2005). As an example, avidin/biotin methods are the most common approaches (fig. 1) (Key, 2009). IHC stained tissue sections are analysed under a brightfield microscope, and the level and localisation of the chromogenic compound gives information as to the level of expression as well as the spatial localisation of the antigen of interest (Key, 2009; Robertson et al., 2008).

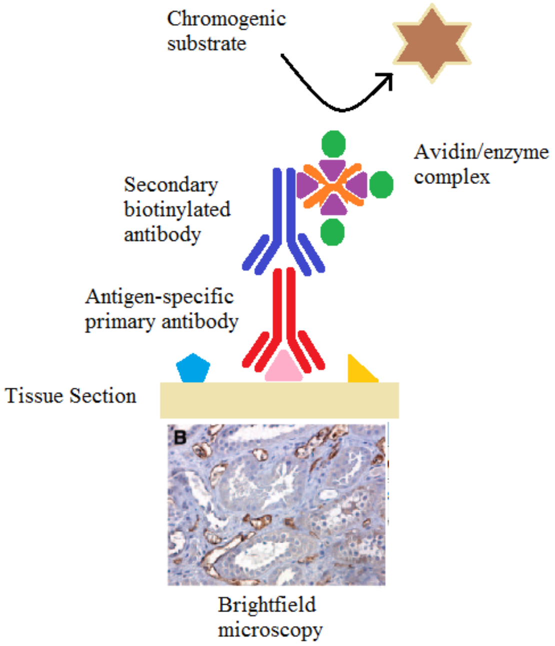

Figure 1 - Diagrammatic representation of indirect avidin/biotin immunohistochemistry. Avidin has a high affinity for biotin, thus the avidin/enzyme complex binds to the secondary bitinylated antibody and catalyses the reaction of the substrate into a chromogenic compound. The image below depicts streptavidin/horseradish peroxidase IHC labelling against C4d antigen in renal peritubular capillaries (brown = positive) (Troxell et al., 2006).

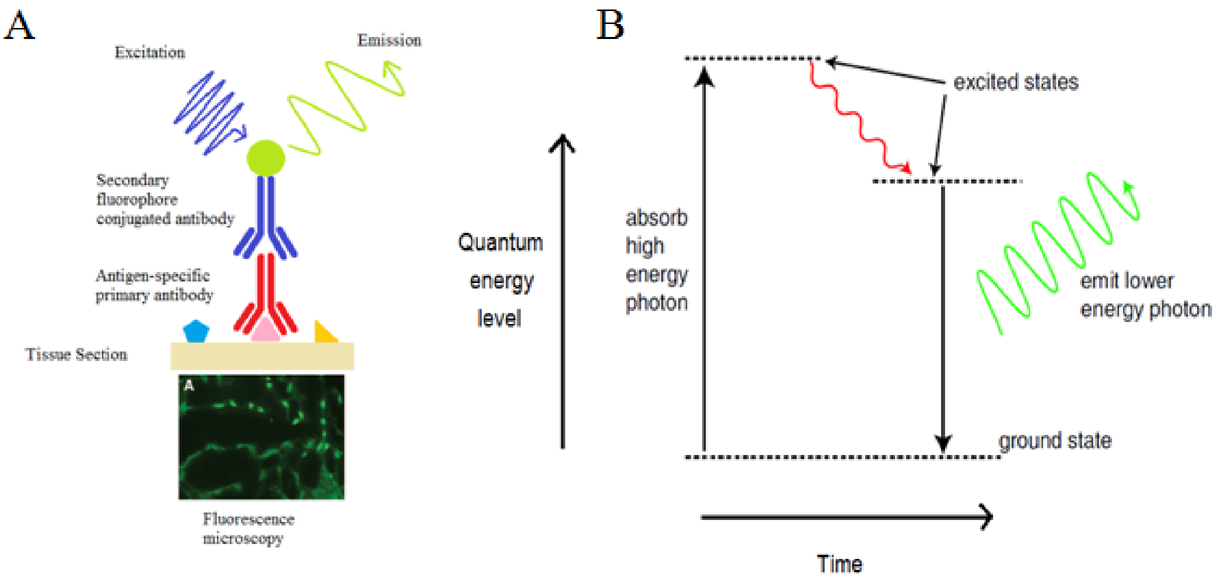

Figure 2 - **A**. Diagrammatic representation of indirect immunofluorescence. Image below = renal peritubular capillaries stained against C4d antigen. Green = positive. (Troxell et al., 2006). **B**. Diagram illustrating physical mechanism of fluorescence. A high energy photon raises the fluorophore to an excited energy state. Some energy is lost to surrounding molecules before the rest of the energy is lost as an emitted lower energy photon, and the fluorophore returns to ground state (Semwogerere and Weeks, 2005).

Alternatively, IF is based on the physical phenomenon of fluorescence, whereby a given molecule may absorb a photon of a specific wavelength, causing an electron to jump to a discrete singlet higher energy state (Semwogerere and Weeks, 2005). Provided no molecules around it can absorb the energy through collisions to return it to ground state, the excited molecule may spontaneously emit a photon of longer wavelength and thus lower energy than that of the exciting photon (Semwogerere and Weeks, 2005) (Fig. 2A,B). Immunofluorescence takes advantage of this phenomenon via the conjugation of fluorophores to antibodies (fig. 2A depicts the indirect immunofluorescence mechanism). Light of a specific wavelength is used to excite fluorophores that are conjugated to antibodies, and the emitted photons are collected and observed by eye through an eyepiece (if the emission wavelength is visible) or detected electronically and a digital image formed (Semwogerere and Weeks, 2005). The applications of fluorescence microscopy in molecular biology are widespread, but this study is primarily concerned with the applications of immunofluorescence in histology.

1.3 Enzyme IHC vs. IF for multiple marker imaging

Enzyme based IHC is the most popular method for visualising specific markers in histology because the protocol is simple to perform, and little specialised equipment is required (Arzt et al., 2009). However, image resolution is limited by the optical restrictions of light microscopy as well as the precipitation of the chromogenic substrate (Robertson et al., 2008). Chromogenic compounds are also prone to signal saturation, which prevents semi-quantitative analysis of the level of expression of such markers (Robertson et al., 2008). Most importantly, imaging multiple markers on the same tissue section is difficult and impractical with enzyme IHC, because any detection systems must be highly sensitive and the chromogenic compounds used must contrast highly to accurately define individually stained areas (Robertson et al., 2008). Double and sometimes even triple antigen staining is still possible using highly contrasting chromogenic compounds, but the requirement of highly visually contrasting compounds often requires the use of a diffuse and less specific chromogen (Vanderloos, 2008). If instead similar colours are used, the analysis of such stains may require novel imaging techniques to separate two visual similar compounds, such as spectral unmixing (Vanderloos, 2008). Generally, the protocols become increasingly more specialised and difficult to perform as more antigens are probed (Krenacs et al., 1990; Robertson et al., 2008; Vanderloos et al., 1988; Vanderloos et al., 1989).

Due to the availability of fluorophores with distinct spectral profiles, it is relatively simple to resolve more than two markers simultaneously using IF in better resolution. This is a highly beneficial and desirable trait for both biomedical research and diagnostic histopathology, as it allows for the visualisation of spatial and temporal relationships between antigens (Brelje et al., 2002; Demandolx and Davoust, 1997; Ma et al., 2007; Robertson et al., 2008).Therefore, for imaging multiple markers in high resolution simultaneously, IF is a more suitable option than enzyme based IHC. However, although this is the case, IF also has its downsides and pitfalls that must be overcome.

1.4 IF imaging pitfalls

The concept of immunofluorescence staining against multiple markers for histological purposes has been around for a relatively long time (Coons et al., 1942; Ferri et al., 1997; Kupper and Storz, 1986; Robertson et al., 2008). However, although IF is precise and high resolution, there are several fundamental obstacles that can reduce the effectiveness of IF for use in research and diagnostic histopathology.

Firstly, constant exposure to excitation wavelengths causes fluorophores to permanently lose brightness, a process termed photobleaching. This is a problem for clinical histological applications, as tissue sections may often require imaging on multiple occasions. Secondly, long-term storage of IF stained material also results in fluorophore degradation (Eggeling et al., 1998), and feasibility of long-term storage is an important prerequisite for diagnostic pathology for documentation purposes and verification of diagnoses (Ermert et al., 2001). The quality of fluorophores widely available around the time of initial studies, such as fluorescein isothiocyanate (FITC), tetramethyl rhodamine iso-thiocyanate (TRITC) and cyanine based dyes such as Cy5, could not address these problems because they photobleach relatively quickly and do not store well (Berlier et al., 2003; Entwistle and Noble, 1992; Ferri et al., 1997; Panchuk-Voloshina et al., 1999; Robertson et al., 2008). In comparison, IHC stained tissue sections can be viewed an almost unlimited amount of times without the chromogenic precipitate deteriorating, and can be stored for many years without requiring darkness or refrigeration (Key, 2009; Renshaw, 2005).

Two other major issues with IF that can limit its viability and application are tissue autofluorescence and spectral bleedthrough. Some tissue types possess natural fluorophores that fluoresce over a broad range of wavelengths and therefore disrupt the interpretation of IF stained tissues, as fluorophore staining may become confused with endogenous tissue autofluorescence (Robertson et al., 2008). For example, vascular and connective tissues strongly autofluoresce because elastin and collagen possesses natural fluorophores (Rigacci et al., 2000).

Spectral bleedthrough is a large problem for multifluorescence imaging, which refers to incidences whereby the emission of one fluorophore is detected through a photomultiplier channel or filter set intended for a second fluorophore (Brown, 2007). This occurs because some fluorophores, FITC and TRITC for example, have broad emission and absorption spectra that largely overlap. Crosstalk between fluorophores can also be an issue if the two fluorophore-labelled biomarkers are in close molecular proximity, whereby the emission wavelength spectrum of one fluorophore overlaps with the excitation spectrum of a second, resulting in subsequent emission of the second fluorophore (Brown, 2007). These imaging artefacts can incorrectly alter the interpretation of images due to the presence of false positive features in certain detector channels (Brown, 2007). Using epifluorescence microscopy, these experimental pitfalls are relatively difficult to avoid unless fluorophores with highly distinct emission and absorption wavelength spectra are used, which limits the amount of markers that can simultaneously be imaged, further reducing the feasibility of IF labelling (Robertson et al., 2008).

For these reasons, such studies have not been widely accepted by the scientific community (Ferri et al., 1997; Robertson et al., 2008). However, more recent studies have opted for new generation Alexa fluorophores, which generally have higher quantum yields (the ratio at which a photon is emitted for every photon absorbed) and/or extinction coefficients (the efficiency of the fluorophore at absorbing light of a given wavelength), and are therefore brighter than older generation dyes (Panchuk-Voloshina et al., 1999, Table S1). In addition, Alexa dyes are more photostable compared to more photolabile older dyes of corresponding spectral profiles (Benchaib et al., 1996), meaning that low-abundance biological structures within tissues can be imaged with great sensitivity and selectivity, and tissue samples can be imaged and re-imaged for extended time periods (Panchuk-Voloshina et al., 1999; Robertson et al., 2008). Fluorescein and rhodamine based dyes, such as FITC and TRITC respectively, as well as sulfonated indocyanine dyes such as Cy5 also have a tendency to quench (reversibly lose fluorescence brightness) upon conjugation to other molecules such as proteins, due to dye molecule interactions, aggregation and formation of non-fluorescent derivatives (Berlier et al., 2003; Panchuk-Voloshina et al., 1999; Ravdin and Axelrod, 1977; Valdesaguilera and Neckers, 1989). This is a problem for indirect IF, as IF utilises fluorophore-conjugated immunoglobulin molecules. Alexa dyes are also insensitive to pH between 4 and 10 compared to these older fluorophores (Panchuk-Voloshina et al., 1999).

In addition to the use of modern dyes, confocal fluorescence laser scanning microscopy (CLSM) has been implicated as a better option to traditional epifluorescence approaches. Such improvements to IF methodology have increased the viability of IF in both experimental and diagnostic histopathology. The principles of CLSM are explained in the following section.

1.5 Principles of CLSM

CLSM differs to standard fluorescence microscopy in a number of ways. The most prominent difference is that a pinhole aperture is incorporated into the optical mechanism, which serves to eliminate photons emitted from fluorophores that do not originate from the focal plane (Paddock, 2000; Semwogerere and Weeks, 2005) (fig. 3).This allows for a visualisation method termed optical sectioning, where thin sections along the z axis of thick samples can be imaged non-invasively and in high resolution by eliminating out of focus light (Finkpuches et al., 1995; Paddock, 2000; Semwogerere and Weeks, 2005). Widefield fluorescence microscopes generally visualise around 2-3 µm thick z sections, while confocal microscopes visualise around 0.5 µm sections, the width of which can be adjusted to suit the sample (Paddock, 2000; Semwogerere and Weeks, 2005). This feature means that is it also possible to resolve separate but stacked features within the z-plane, which otherwise would appear as one blurry entity in widefield imaging. Additionally, due to high axial resolution (Sheppard, 1989), sharp 3D images of samples can be produced by sequentially scanning different focal planes and subsequently stacking the images, a process termed z-stacking (Semwogerere and Weeks, 2005).

Another major difference is the excitation light source. Rather than standard mercury or xenon arc lamps, CLSM illuminates samples using high-powered monochromatic lasers (Paddock, 2000; Semwogerere and Weeks, 2005). Intense, bundled laser light sources are preferentially used because pinhole apertures generate optical sections by blocking out defocused light emitted from fluorophores, and therefore cause a loss of signal strength reaching the detector (Semwogerere and Weeks, 2005). Thus, conventional lamps do not provide light of a high enough intensity for enough emitted photons to be collected for good quality imaging. CLSM systems acquire images through the sequential scanning of laser lines across a sample, and images are digitally rebuilt from recorded point intensities according to x-y coordinates (Semwogerere and Weeks, 2005). Although CLSM systems are usually more expensive and require additional training for proficient use, CLSM has many benefits over regular fluorescence microscopy which increase the applicability of a multilabelling IF method to histopathology.

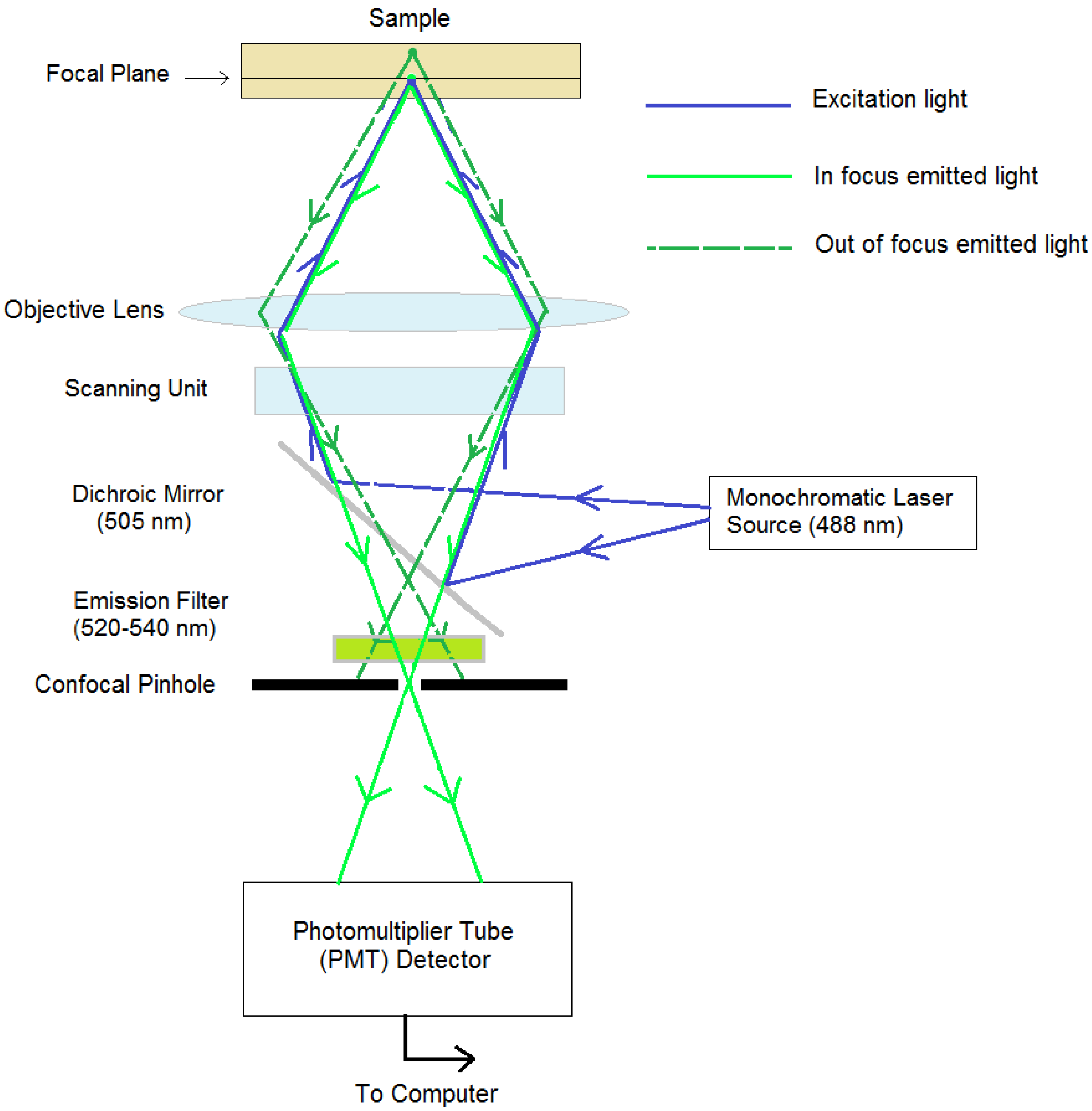

Figure 3 - Schematic diagram of a confocal laser scanning fluorescence microscope. An inverted setup is depicted, similar to the primary instrument used for this study. Excitation wavelengths are reflected by the dichroic mirror through the objective lens and onto the sample, while returning emitted light wavelengths pass through it. The scanning unit sequentially alters the path of the excitation beam to scan across the x and y axis and build an image of the sample. The pinhole restricts light reaching the detector to only in-focus light, from which an image is digitally rebuilt. The wavelength values depicted are typical values used for imaging fluorescein isothiocyanate (FITC) or Alexa 488 fluorophores.

1.6 Advantages of CLSM in histology

As well as the benefits of being able to obtain high-resolution images of thin optical sections, the features of CLSM can reduce some common imaging problems often encountered during regular fluorescence microscopy when used in a histological context.

Many features of CLSM act to reduce autofluorescence and spectral bleedthrough, and thus CLSM constitutes a better option for imaging multiple markers via IF. Firstly, thin optical sections reduce the volume of tissue that can contribute to autofluorescence (Ma et al., 2006; Robertson et al., 2008). Secondly, the monochromatic excitation lasers are of much narrower wavelength (<5 nm) in comparison to standard fluorescence mercury vapour lamps (250-800 nm) (Robertson et al., 2008). This has two benefits, in that much of the spectrum that can cause autofluorescence is removed, and also that spectral bleedthrough is less likely to occur due to the decreased potential of simultaneously exciting two separate fluorophores with one excitation line. More precise, numerically defined emission collection windows are also available on confocal systems, further reducing the potential for autofluorescence and spectral bleedthrough (Paddock, 2000; Robertson et al., 2008). In addition, CLSM systems have the added option of alternately scanning each laser line across the sample, so that only one fluorophore species at a time is excited but an image comprised of multiple fluorophores is obtained (Brown, 2007; Robertson et al., 2008). This further reduces the chance of spectral bleedthrough, because at any given time during collection only one laser line is active and only one emission collection window is open (Robertson et al., 2008). Some confocal systems can rapidly oscillate laser lines sequentially either electronically or through the use of acousto-optic tuneable filters (AOTF), and can therefore achieve this sequential excitation and emission collection with only millisecond delays between laser lines (Brown, 2007).

These features, combined with the rejection of out of focus blur, also mean that more accurate quantitative comparison of multifluorescence signals is possible (Demandolx and Davoust, 1997; Sandison and Webb, 1994), and CLSM is a highly viable approach for the spatial and temporal resolution of specific antigens in histopathology.

However, the use of new generation fluorophores is of even greater importance than when using standard fluorescence microscopy. Increased fluorophore photostability is an essential attribute in CLSM for a number of reasons. Firstly, the high intensity laser light source means that photobleaching occurs faster (Paddock, 2000). Secondly, although the pinhole blocks emitted light originating from the focal plane, the surrounding areas of the tissue along the z-axis are still exposed to excitation wavelengths and therefore will also photobleach (Brown, 2007; Paddock, 2000). Thirdly, the production of 3D images of tissues requires repeated exposure of the same area to excitation wavelengths (Paddock, 2000; Semwogerere and Weeks, 2005). The higher quantum yield of the new fluorophores is also beneficial (Panchuk-Voloshina et al., 1999), particularly because the pinhole blocks out much of the signal reaching the detector to generate optical sections (Semwogerere and Weeks, 2005). One further advantage of these next generation fluorophores, especially for clinical histopathology, is that they have been shown to store more effectively, and studies have found that tissues stained with Alexa secondaries can be stored at -20 ^{o}C for at least nine months without a detectable loss of staining quality (Robertson et al., 2008).

1.7 Recent advances of imaging multiple markers using confocal microscopy in histology

Multiple antigens have been successfully imaged via IF and confocal microscopy for a wide range of tissues and tissue processing methods. For example, cytokeratin 8/18, vimentin and oestrogen receptors have been simultaneously imaged in both malignant and normal breast tissue for a comparison of spatial expression and distribution of markers (Robertson et al., 2008). Similarly, the prognostic significance of caveolin 2 in breast cancer has been analysed via simultaneously imaging caveolin 1, caveolin 2 and p63 (Savage et al., 2008). An additional study investigated correlations between insulin-like growth factor I receptor and oestrogen receptor beta expression in colorectal cancer tumourigenesis (Papaxoinis et al., 2007), highlighting the use of the method for monitoring multiple markers simultaneously. Also, such studies highlight the applicability of such a method for oncogenic biomedical research purposes.

Other successful applications of multiple immunostaining and imaging via CLSM include imaging mesenchymal stromal cells (MSCs) in cryosections of colonic tissue via immunostaining of the MSC marker CD146 alongside other non-MSC markers such as von Willebrand factor (vWF) and actin (Signore et al., 2012). Markers such as E-cadherin, Ksp-cadherin and collagen IV have been visualised in FFPE sections of kidney (Robertson et al., 2008). In addition, whole mounts of human and murine bone marrow have been imaged via IF and CLSM against markers such as CD3, CD45R and Ter119 in order to visualise haematopoiesis in three dimensions (Takaku et al., 2010). Another study optimised a multiple immunolabelling CLSM method to simultaneously visualise viral antigens and tissue antigens to identify the foot and mouth disease virus in a wide range of animal tissues (Arzt et al., 2009).

The wide range of tissues and markers that have been successfully imaged highlights the wide applicability of the method as a histological and pathological research tool. However, relatively few studies have been undertaken using similar methods to image multiple markers within immunological tissues. This constitutes the primary aim of this study.

1.8 IF CLSM for imaging immunological tissues

Based on these recent successes of multiple marker imaging via IF and CLSM in many tissue types, the ability to simultaneously visualise multiple biomarkers within secondary lymphoid tissues would be highly beneficial to immunological histology and histopathology. This is because the immunophenotypes of immunological cells are complex and often require the identification of more than one marker for accurate identification of specific cell types (Ma et al., 2006). In addition, cancers that manifest themselves within lymph nodes, such as lymphatic leukaemias and lymphomas, have complex immunophenotypes that can confer diagnostic and prognostic information of the disease (Hayden et al., 2012; Sathiya and Muthuchelian, 2009).

From a methodological perspective, lymphoid tissues are ideal for the optimisation of an IF/CLSM tissue imaging method, because they possess histologically distinct areas that contain high densities of immunological cells which have well defined immunophenotypes, such as primary and secondary follicles that contain high levels of B-lymphocytes (Cesta, 2006; Willard-Mack, 2006). Thus, many different antigens can be chosen from, many of which will provide robust staining of target cells. In addition, immunological markers such as CD3, CD4 and B220 have already been imaged via IF and CLSM on lymphoid tissues such as mouse spleen with robust results (Ma et al., 2006).

1.9 Aims and objectives

Preliminary experiments performed on lymph node cryosections had yielded promising results in markers such as the CD4 and CD8 T cell subset markers, the B cell markers CD19 and CD20 and κ and λ immunoglobulin light chain antigens (data not published). These studies were, however, performed using the older generation fluorophores FITC, TRITC and Cy5. Therefore, based on these preliminary studies and the literature discussed, the aims of this study were to further refine and modernise the multiple immunostaining protocol on immunological tissues, and optimise the microscope imaging settings to obtain the best images possible. In doing this, the study will develop this method as a research tool as well as increase its potential for routine use in clinical histopathology. The specific study objectives were to:

- Establish an effective immunological tissue type upon which to optimise secondary antibody dilutions.
- Optimise the immunostaining protocol for use with new generation Alexa fluorophores.
- Optimise the secondary antibody dilutions and confocal laser-scanning microscope settings to produce images with the best possible resolution and signal/noise ratio.

1.10 Experimental procedure

For the purposes of this optimisation study, it was decided that staining against B-lymphocyte surface markers within fixed tissue samples would be a suitable approach, because B cells are abundant within secondary lymphoid organs and tissues such as the spleen and lymph nodes (Cesta, 2006; Willard-Mack, 2006). Specifically, the B-lymphocyte antigens that were selected were the B-cell surface marker CD19, and kappa (κ) and lambda (λ) immunoglobulin light chains. These three antigens were chosen for a number of reasons as follows:

- CD19 is expressed by all recognisable B-lineage cells independent of developmental stage and maturity, with the exception of fully differentiated plasma cells (Del Nagro et al., 2005). B-lymphocytes also express surface immunoglobulin, which is expressed by all B lineage cells except for those at very early stages of development, or terminally differentiated plasma cells (Thiel, 1985). In secondary lymphoid organs, affinity maturation of B lymphocytes in response to foreign antigen takes place within secondary follicles (Cesta, 2006; Vandervalk and Meijer, 1987; Willard-Mack, 2006), and therefore dense regions of CD19, and surface immunoglobulin expressing cells should be present, providing excellent regions to image for optimisation purposes.

- All B cells produce antibodies with κ or λ immunoglobulin light chain forms, which are also expressed on the cell surface within IgM and IgD isotypes. Individual B cells exclusively express either κ or λ immunoglobulin light chain forms (Takeda et al., 1993). Therefore, any given CD19 positive cell should also be positive for either κ or λ antigen. This expectation aids the optimisation process in that a general idea of the resulting staining pattern is known, and it is therefore easier to discern genuine antigen staining from imaging artefacts.
- Previous preliminary experiments performed on other confocal microscopy systems and with original fluorophores had reported that the available anti-CD19, κ and λ antibodies were effective. The staining was relatively bright and abundant in relation to other markers imaged, and therefore ideal for optimisation experiments.

2.0 Materials and Methods

2.1 Acquisition and fixation of tissue samples

All tissue samples used in the study were obtained from the Human Biomaterials Resource Centre at the University of Birmingham, observing all ethical guidelines. Human spleen and reactive lymph node tissue sections of 5 µm thickness were independently pre-prepared via cryosectioning and affixed to glass slides. Mounted tissue sections were fixed in acetone for 10 minutes at 4 ^{o}C and stored at -20 ^{o}C in the presence of silica gel to prevent condensation and ice crystal formation within the tissue samples.

2.2 Jenner/Giemsa staining and imaging

Jenner/Giemsa phosphate buffer was diluted 1:25 in distilled water. Jenner stain (Raymond A. Lamb Ltd) was diluted 1:3 in the diluted buffer, and Giemsa stain (VWR) was diluted 1:20 in the diluted buffer. 50 µl diluted Jenner stain was pipetted onto the tissue sections and incubated for 5 minutes at room temperature (RT). The tissue was carefully washed with distilled water, and 50 µl diluted Giemsa stain was pipetted onto the tissue section and incubated for 10 minutes at RT. The dH_2O wash was repeated and the tissue section left to dry thoroughly before mounting with DePeX mounting medium (VWR) and a 1.5 mm thick glass coverslip. The stained sections were imaged at 10x magnification using an Olympus BX-40 light microscope, an Olympus 10x Plan objective with a numerical aperture of 0.25 and an Olympus C-5050 Zoom Digital Camera.

2.3 Indirect immunofluorescence staining protocol

Glass slides with tissue sections were removed from -20 ^{o}C storage and left to equilibrate to room temperature (RT) for 10 minutes. Tissue sections were outlined using a slide marker pen (Dako) to keep tissue sections covered with antibody solution. To block endogenous Fc receptors and prevent non-specific antibody binding to immune cells, 50 µl FcR Blocker

(Innovex Biosciences) was pipetted onto the tissue sections and incubated for 30 minutes at RT within a light excluding moist chamber. Excess fluid was removed from the tissue sections and 50 µl primary antibody diluted in FcR Blocker was added to the tissue sections and incubated for 60 minutes at RT in a moist chamber. Excess solution was removed and the slides washed in a phosphate-buffered saline (PBS) bath for 20 minutes at RT in the dark and on a magnetic stirrer at low speed. Secondary antibody dilutions were prepared as stated for primary antibodies, but the solution was also microfuged for 2 minutes at 14,000 RPM. Excess PBS was removed and 50 µl secondary antibody diluted in FcR blocker was pipetted carefully from the top of the solution and onto the tissue sections, and incubated in the same manner as the primary antibody. A PBS wash was repeated as before, and excess PBS removed. To avoid problems with pipetting error and avoid pipetting centrifuged secondary antibody aggregates at the base of the eppendorf tubes, all antibody solutions were made up to volumes of at least 50 µl excess. Stains against multiple antigens were performed by diluting all primary antibodies of individual IgG subclass within one mixture, followed by the same process with secondary antibodies. To control for non-specific binding of fluorophore-conjugated secondary antibodies, the staining procedure was carried out twice for each variation of staining, but for the second stain the primary antibody was omitted.

2.4 Nuclear counterstaining and slide mounting

Two mounting and counterstaining methods were used within the study. For slides mounted with VECTAShield with 4',6-diamidino-2-phenylindole (DAPI, Vector Laboratories), slides were mounted and counterstained by pipetting 10 µl VECTAShield with DAPI onto the tissue section and placing a glass coverslip onto the section. The slides were then inverted on tissue paper to remove excess mountant. Coverslips were sealed around the edges with clear nail varnish. Alternatively, tissue sections were counterstained by incubation in a PBS solution with Hoechst bis-benzimide dye 33258 at 20 µg/ml for 1 minute at RT, followed by a 1 minute PBS wash. Slides were then mounted by pipetting 10 µl glycerol-based antifade mounting medium (INOVA Diagnostics), and inverted on tissue paper to remove excess mountant and sealed with clear nail varnish. Prior to imaging, the slides were then stored at -20 °C in the dark.

2.5 Primary and secondary antibody tables

Due to issues of cross-reactivity, it can be potentially difficult to image multiple markers simultaneously using multiple primary antibodies raised in the same animal. One solution is to use monoclonal primary antibodies of differing antibody subclass, and corresponding monoclonal secondary antibodies highly specific to these subclasses (Buchwalow et al., 2005; Ma et al., 2006), which was used for this study.

The following antibodies were used throughout the study. All primary and original secondary antibodies were supplied by Santa Cruz Biotechnology, and all Alexa secondary antibodies were supplied by Invitrogen:

Primary Antibodies			
Isotype Subclass	**Affinity**	**Stock Concentration**	**Dilution Used**
IgGγ1	mouse anti-human κ Immunoglobulin light chain	100 µg/ml	1:100 (1 µg/ml)
IgGγ2a	mouse anti-human λ Immunoglobulin light chain	100 µg/ml	1:50 (2 µg/ml)
IgGγ2b	mouse anti-human CD19	100 µg/ml	1:100 (1 µg/ml)

Original fluorophore - conjugated secondary antibodies			
Subclass Affinity	**Fluorophore, affinity and isotype**	**Stock Concentration**	**Dilution Used**
γ1	FITC conjugated goat anti-mouse IgG γ1	1 mg/ml	1:100 (10 µg/ml)
γ2a	TRITC conjugated goat anti-mouse IgGγ2a	1 mg/ml	1:50 (20 µg/ml)
γ2b	Cy5 conjugated goat-anti mouse IgG γ2b	1 mg/ml	1:100 (10 µg/ml)

The primary and first generation secondary antibodies were used at fixed dilutions determined as optimum concentrations by preliminary experiments. However, Alexa secondary antibodies were used at different dilutions depending on the experiment, as detailed in the results section.

Alexa fluorophore - conjugated secondary antibodies			
Subclass Affinity	**Fluorophore, affinity and isotype**	**Stock Concentration**	**Dilution Used**
γ1	Alexa488 conjugated goat anti-mouse IgG γ1	2 mg/ml	See results
γ2a	Alexa568 conjugated goat anti-mouse IgG γ2a	2 mg/ml	See results
γ2b	Alexa647 conjugated goat anti-mouse IgG γ2b	2 mg/ml	See results

For the dilutions stated in the following results sections, the corresponding final concentrations for the Alexa secondaries were as follows (table over page):

Dilution	**Concentration**
1:50	40 µg/ml
1:100	20 µg/ml
1:200	10 µg/ml
1:400	5 µg/ml

For additional information regarding the molecular and spectral properties of each fluorophore used within this study, see table S1.

2.6 Confocal laser scanning fluorescence microscopy imaging

For all experiments, a Nikon A1R^{+} Eclipse Ti Inverted Microscope System (Nikon Instruments) was used, and images were digitally acquired through photomultiplier tubes via Galvanometric one-way laser scanning at a speed of 1 frame per second and a resolution of 512x512 pixels. Images were acquired at 40x magnification, for which an oil immersion 40x Plan Fluor differential interference contrast (DIC) H N2 objective with a numerical aperture of 1.3 was used (Nikon). Fluorescence images for up to 4 colours were simultaneously captured, with electronic sequential laser scanning enabled to aid elimination of spectral bleedthrough. Confocal Pinhole diameter was preset to 1 Airy Unit. Laser excitation and emission filter settings are detailed in the following table:

Photomultiplier Channel	**Laser Excitation Wavelength (nm)**	**Emission Collection Window (nm)**
DAPI/Hoechst 33258	402.1	425-475
FITC/Alexa 488	488	500-550
TRITC/Alexa 568	561.1	570-620
Cy5/ Alexa 647	637	662-737

Areas of high B lymphocyte levels with strong CD19 positivity were preferentially imaged, and for each individual tissue section the corresponding region or a highly similar region was imaged and analysed for continuity.

2.7 Image analysis

Images were analysed using NIS-Elements v3.2 (Nikon). The linear contrast was adjusted on the final images to emphasise stained areas and remove background noise. This value differed per image and tissue section, but corresponding secondary only controls were always examined under the same look-up table (LUT) settings to confirm that no background or autofluorescence was emphasised, or indeed at all present.

2.8 Quantification of CD19 and κ/λ positive cells

Three images of suspected B-lymphocyte rich regions were taken at 40x magnification from lymph node cryosections stained with differing secondary antibody panels. For consistency, areas that were imaged contained CD19 positive cells throughout the entire image field. All cells that were CD19 and κ-antigen positive were counted, as were CD19 and λ-positive cells. The numbers were averaged for each differing antibody panel, and the standard deviation and standard error of the values were obtained using Microsoft Excel 2007.

2.9 Statistical analysis

Two-tailed T tests were performed between each variation of secondary antibody staining panel using Microsoft Excel 2007.

3.0 Results

3.1 Selection of suitable tissue and mounting method

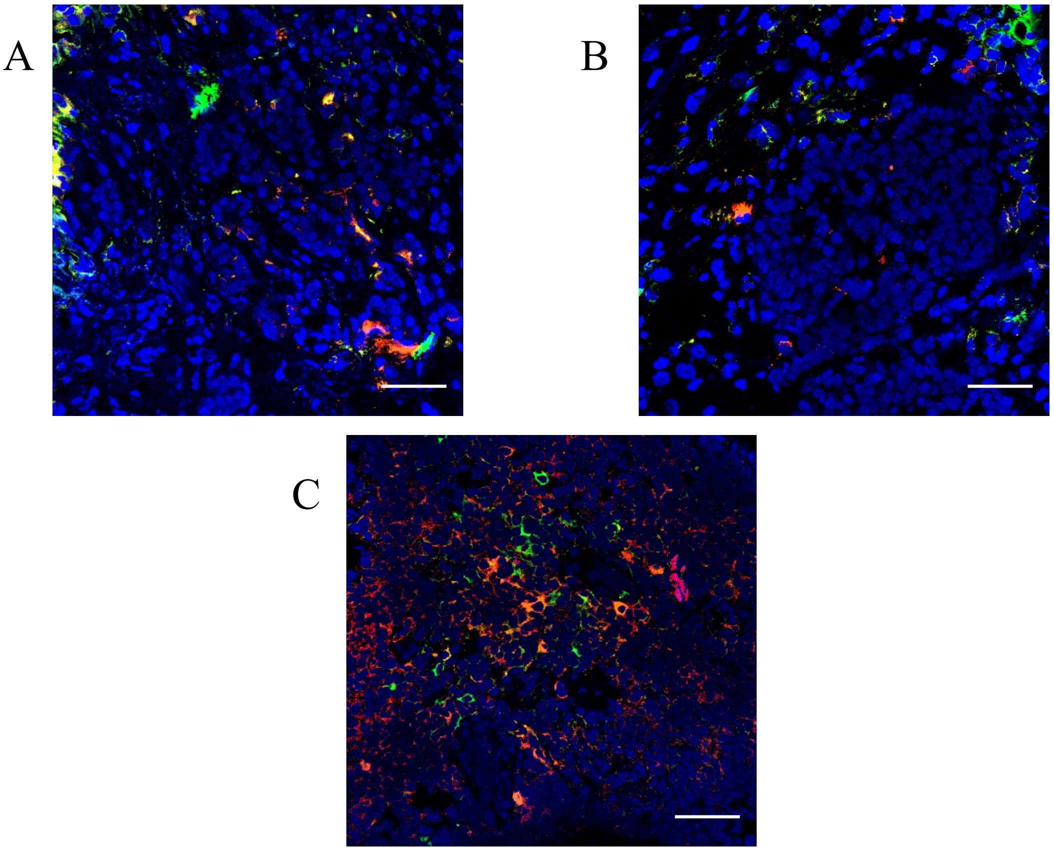

Figure 4 – Example images of staining quality across immunological tissue samples. **A**. Healthy spleen cryosection. **B**. Healthy spleen cryosection from a different individual. **C**. Reactive Lymph node cryosection. Images were obtained at 40x magnification and scale bars represent 50 μm. Pseudocolours – Blue = Nuclear counterstain, Green = κ/FITC, orange = λ /TRITC, red = CD19/Cy5.

Firstly, the primary tissue samples for which to perform the optimisation experiments on had to be determined. To establish this, tissues were simultaneously stained with pre-determined concentrations of previously used original secondary fluorophore conjugates, because they were known to be effective (See section 2.5). Initially, the experiments were performed on spleen biopsy samples from healthy subjects. However, the first spleen sample analysed did not produce good quality staining, and it was difficult to positively identify stained cells (fig.4

A). In addition, the sample contained relatively few B-lymphocyte rich follicular regions or germinal centres. The staining protocol was therefore repeated with cryosections from a new spleen sample, which also showed poor staining quality (fig. 4B), and it was therefore decided to test the protocol on cryosections derived from hyperplasic reactive lymph nodes. Reactive lymph nodes are enlarged and generally richer in B-lymphocytes as they are actively responding to antigen stimulation (Bain and Bain, 1985). The quality of staining was observed to be superior to either spleen sample tested, and positively stained cells were far easier to identify and more abundant (fig. 4 C). Jenner-Giemsa stains were also performed on the tissues to examine the histological differences between the lymph node cryosections and reactive lymph node cryosections (fig. 5). Within the reactive lymph node cryosections, it proved difficult to identify any well defined histological features that are known to contain a high proportion of CD19 positive B-lymphocytes such as germinal centres. However, darkly stained regions as seen in fig. 5B corresponded with CD19 positive areas when imaged with the confocal microscope suggesting that these regions were rich in B lymphocytes. These areas were abundant throughout the tissue, and it was therefore decided that all subsequent experiments were to be carried out on reactive lymph node cryosections.

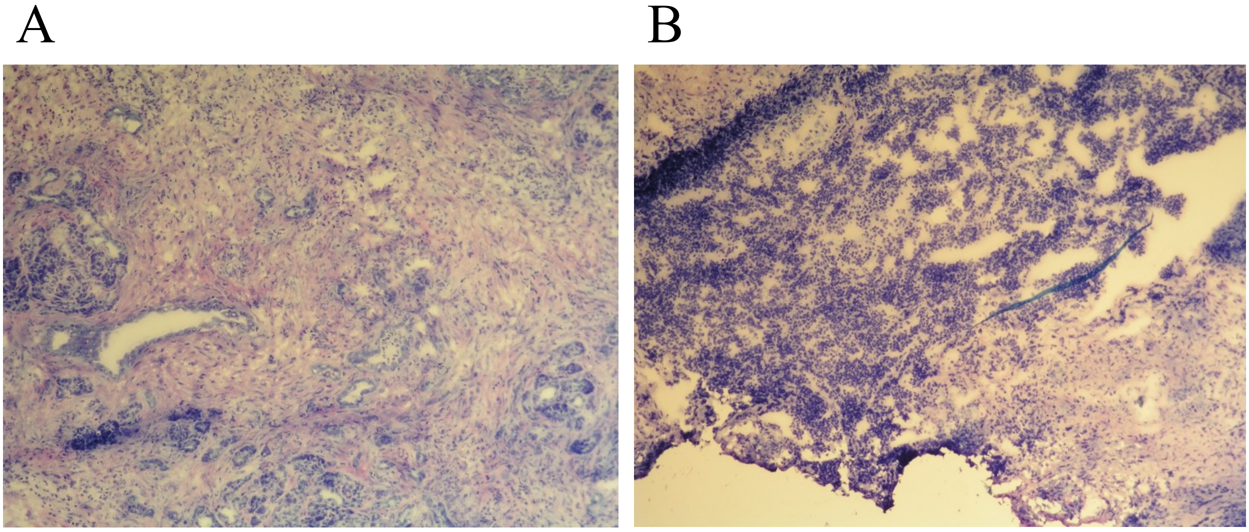

Figure 5 - Jenner/Giemsa stains of healthy spleen (**A**) and reactive lymph node (**B**) cryosections at 10x magnification. Nuclei stain blue, while eosinophils stain in varying shades of pink. The densely packed darker regions visible on the reactive lymph node stained strongly for CD19 and κ/λ antigen, suggesting that they were B-lymphocyte rich regions, while it was difficult to identify B-lymphocyte rich regions in the spleen samples.

Another potential issue was the quality of the nuclear counterstain. It was observed that the relative brightness of the Hoechst nuclear counterstain was faint, meaning that the laser power and PMT gain of the Hoechst channel had to be set high to obtain quality images. A different counterstaining and mounting method was therefore tested. VECTAShield with DAPI is another glycerol based mountant that remains fluid after mounting, but unlike the previously used mountant it also contains the counterstain dye (DAPI), removing the requirement for the Hoechst staining step. However, there was little difference in counterstaining brightness between both methods (fig. 6). Furthermore, the brightness of Cy5 staining was markedly diminished when the slides were mounted with VECTAShield. The original Hoechst counterstaining method was therefore used for all subsequent experiments rather than VECTAShield with DAPI.

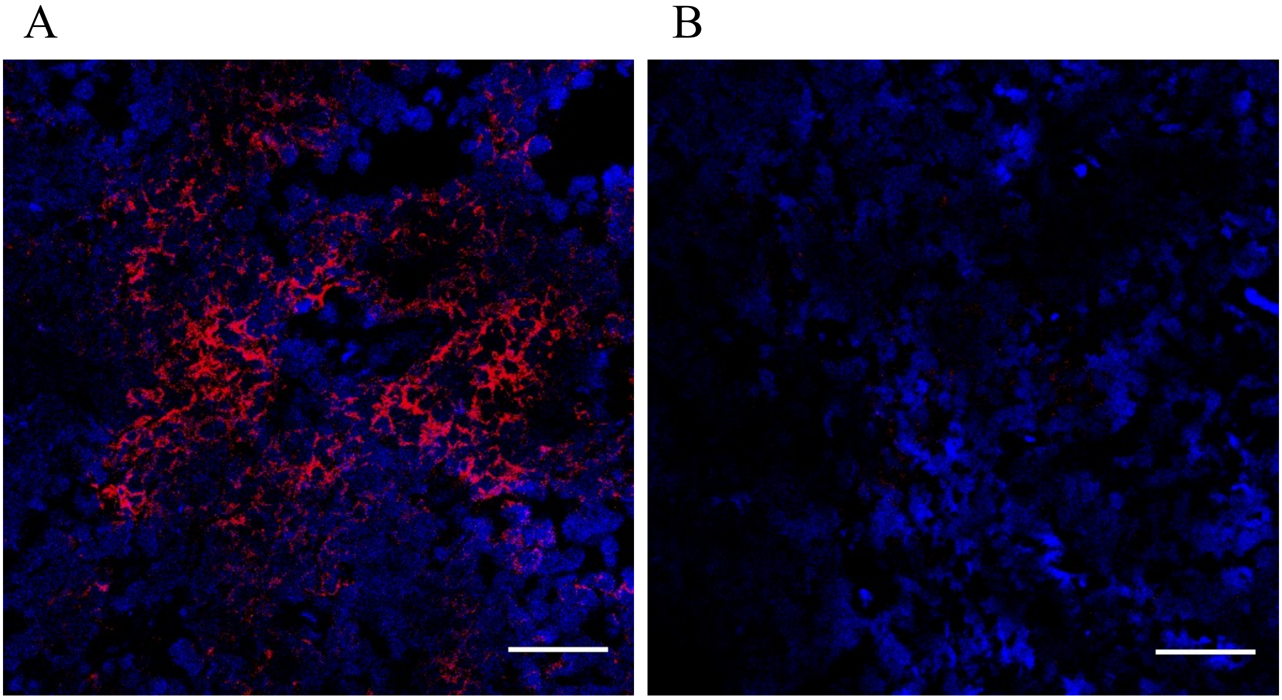

Figure 6 – Comparison of Cy5 signal strength between tissue sections mounted with INOVA antifade mounting medium and counterstained with Hoechst 33258 (**A**) and VECTAShield with DAPI (**B**). Cy5 signal strength was much stronger in the first instance, which was therefore used for all subsequent experiments. Images were obtained at 40x magnification and scale bars represent 50 µm. Pseudocolours - Blue = nuclear counterstain, red = CD19/Cy5.

3.2 Acquisition of microscope settings and single colour controls

The next stage of the study was to identify the optimal laser power and photomultiplier tube (PMT) gain settings for maximum signal strength, and to determine that no spectral bleedthrough was occurring between the lasers lines used to visualise each different fluorophore. As previously discussed, this can potentially manifest as a problem where multiple fluorophores are used simultaneously, thus it was essential to confirm that this was not occurring.

When acquiring the images, it was also important to avoid fluorophore and detector saturation. Fluorophore saturation can occur if the laser power is set too high, causing all fluorophores to excite throughout the z-plane, resulting in unnecessary photobleaching and poorer z-axis resolution (Brown, 2007) . Alternatively, detector saturation can occur if the PMT gain is set too high, leading to a loss of features within the sample and false interpretation of images (Brown, 2007). To avoid either of these scenarios, a saturation detector feature was enabled during these experiments, which highlights fully saturated pixels within the image, thereby allowing for the adjustment of microscope settings accordingly.

To establish these settings, and if spectral bleedthrough was present, individual lymph node cryosections were stained with one primary and a fluorophore-conjugated secondary antibody of corresponding isotype subclass specificity, and imaged in turn. The following laser power and PMT gain settings at which the images were collected were chosen on the basis of giving the strongest signal on positively labelled samples without saturation, whilst having no observable signal present in the corresponding channel for the control tissue sections stained with secondary antibody only (table over page):

Spectral Channel	**Laser Power**	**PMT Gain**
Hoechst/DAPI	50%	110
FITC/A488	30%	70
TRITC/A568	30%	70
Cy5/A647	50%	95

Images were obtained for all four collection windows, and if no spectral bleedthrough was occurring, all channels were expected to be free of signal except for the intended channel of the fluorophore the sample was stained with. Some residual signal was occasionally present in the Hoechst channel (fig. 7), but this was due to the fact that the Hoechst counterstain was relatively faint and it was therefore necessary to set PMT gain and laser power relatively high. This was therefore most likely to be tissue autofluorescence as the signal covered all tissue present in the image and did not resemble staining observed in any other channel. Because this tissue autofluorescence was present in the Hoechst channel, this did not pose a problem for the analysis of the fluorophore-conjugated secondary antibodies and was therefore not an overbearing concern.

Aside from the Hoechst imaging channel, all secondaries produced signal in the correct imaging channel, and no signal was observed across multiple channels (fig. 7). The PMT gain and laser power settings at which these images were obtained could therefore be used for all other experiments with the assurance that spectral bleedthrough was not disrupting the interpretation of the images. To be confident of this throughout future experiments, these settings were treated as maximum and not exceeded.

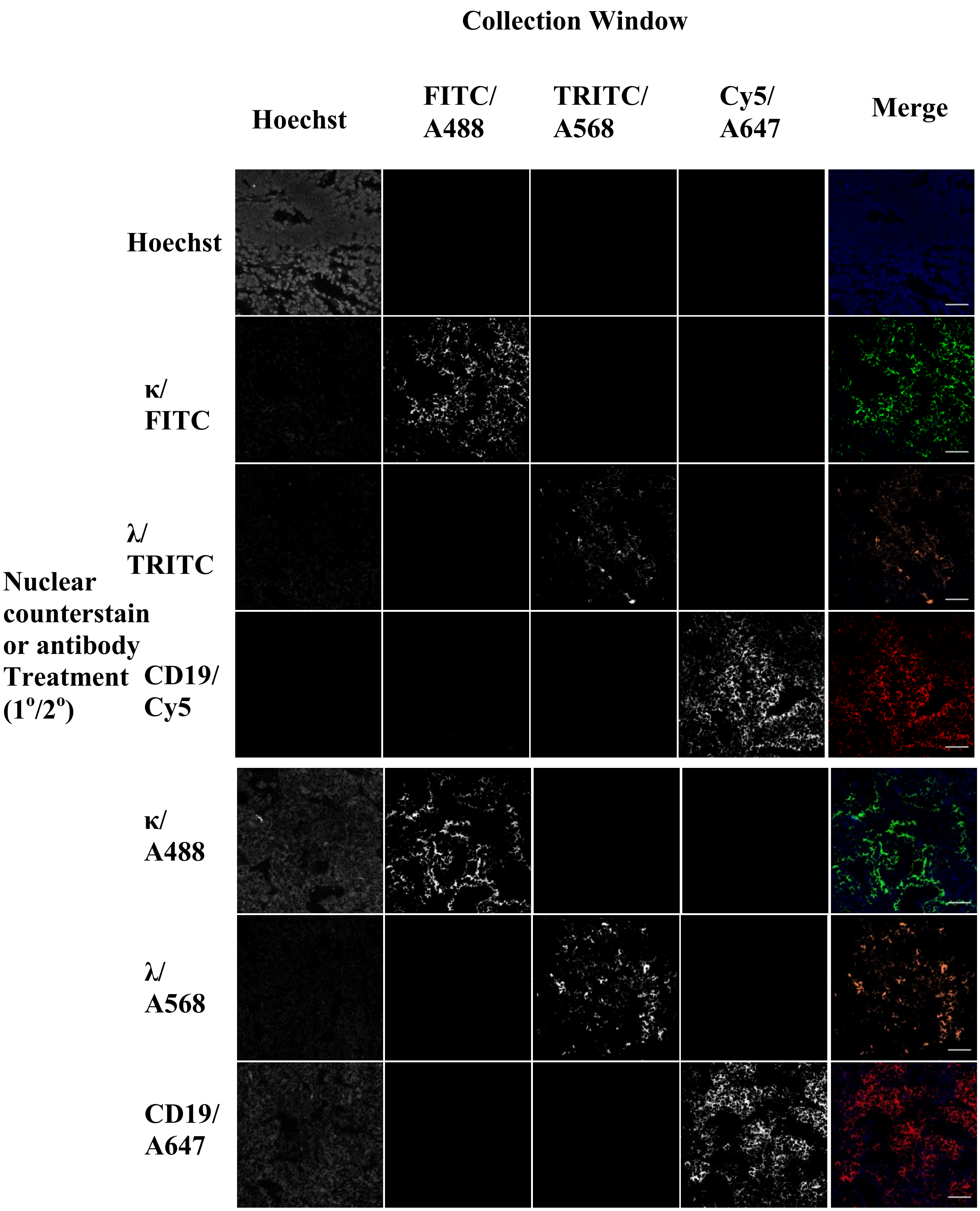

Figure 7 – Single colour controls for all fluorophores used in the study performed on reactive lymph node cryosections. Aside from tissue autofluorescence detected in the Hoechst channel, no detectable signal was observed in channels other than those for which the corresponding primary antibody was added. Images were obtained at 40x magnification and scale bars represent 50 µm. Pseudocolours - Blue = nuclear counterstain, Green = κ /FITC or A488, orange = λ /TRITC or A568, red = CD19/Cy5 or A647.

3.3 Titration of Alexa-conjugated secondary antibodies

It was established that no spectral bleedthrough was occurring across laser lines for any fluorophore type used in this study when used at the highest concentrations, and imaged with the highest laser power and PMT gain settings possible without saturation. The next phase of the study was to identify the optimum dilutions at which to use the Alexa secondaries along with the full cohort of primary antibodies. This was achieved via titration of the secondary antibodies through 1:2 serial dilutions, ranging from overall dilutions of 1:50 to 1:400, and qualitatively assessing the brightness and signal/noise ratio in relation to the original secondaries. In addition, negative controls treated with secondary antibody only were performed for each dilution to assess the levels of nonspecific flourophore binding to the tissue and adjust the microscope settings accordingly.

Alexa488 was most effective at a dilution of 1:200, because at 1:50 and 1:100, a large amount of non-specific signal was present within the secondary only control. The laser power and gain levels were therefore reduced so that this signal was no longer visible, but this had the effect of reducing the overall brightness of the staining to unacceptable levels (fig. 8). At 1:400, the staining appeared fainter than that of 1:200 using the settings described in section 3.2 for visualising A488, and these settings were not exceeded because:

a) tissue autofluorescence was visible at laser power and PMT gain settings that were slightly higher than optimum levels.

b) the single colour controls had indicated an absence of spectral bleedthrough at these settings, and this was no longer a reliable observation should the laser power or PMT gain be increased.

Alexa568 produced high quality staining at dilutions of 1:50, 1:100 and 1:200, while the signal was slightly fainter at 1:400 (fig. 8). Although 1:100 and 1:200 were effective, 1:50

was deemed to be the optimum concentration due to very little nonspecific signal detected in the secondary only control and slightly superior signal strength.

Alexa647 was deemed to be most effective at 1:400 because at levels of 1:50, 1:100 and 1:200 there were high levels of background noise in the secondary only controls, suggesting a high level of nonspecific fluorophore binding. However, at 1:400, A647 was faint compared with Cy5 at 1:100 and the linear contrast had to be enhanced more to reveal the staining (fig. 8). As the contrast was enhanced, the same alterations were performed on the secondary only controls to ensure that no tissue autofluorescence or nonspecific fluorophore binding was enhanced.

Overall, it was qualitatively determined that A488 at 1:200 and A568 at 1:50 provided brighter staining than FITC at 1:100 and TRITC at 1:50. However, due to high levels of nonspecific noise at higher concentrations, the optimum dilution of A647 was 1:400 at which the signal levels were relatively low, and the most effective far-red emitting fluorophore was therefore less apparent. Thus, the next stage of the study was to perform triplet stains of CD19, κ and λ antigens, using the Alexa secondaries at the optimally defined dilutions and directly comparing the staining quality to the optimal original secondary antibody panel.

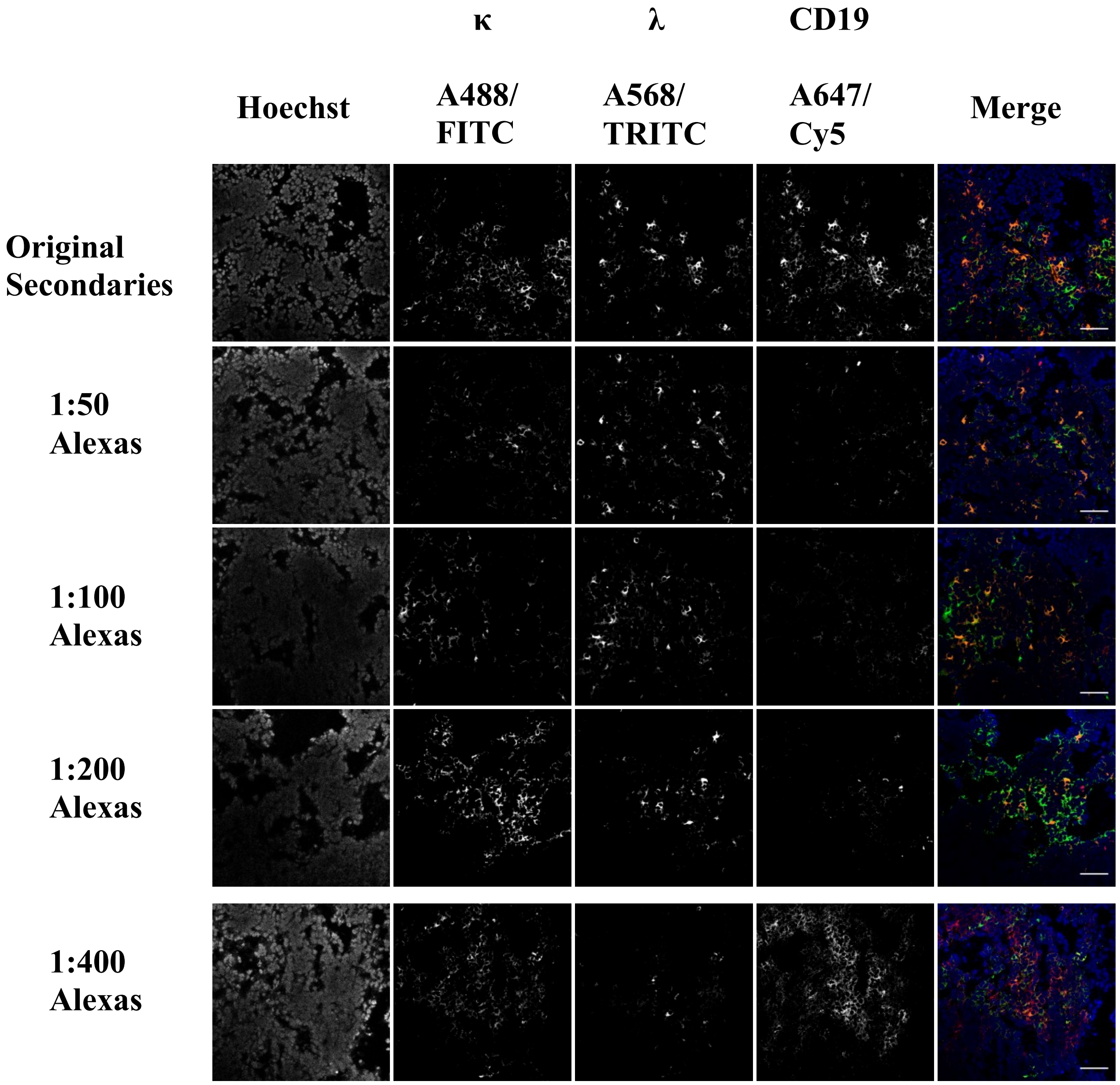

Figure 8 – Reactive lymph node cryosections stained with the full cohort of primary antibodies and subsequent serial titrations of Alexa fluorophore conjugated secondary antibodies performed to obtain optimum dilutions. Images were obtained at 40x magnification and scale bars represent 50 µm. Pseudocolours – Blue = nuclear counterstain, Green = κ /A488, orange = λ / A568, red = CD19/ A647.

3.4 Identification of optimum secondary antibody concentrations

Due to a shortage of tissue sections, the following experiments were carried out on reactive lymph node sections sourced from a different patient. However, highly similar staining characteristics were observed, and thus the information obtained from the previous optimisation experiments could be confidently applied to these subsequent experiments performed on reactive lymph node tissue obtained from another individual. This reproducibility of staining quality between individuals was also in itself an important observation as this is an essential quality should the method be routinely used in histopathology.

The next stage of the study was to obtain images of lymph node cryosections stained against CD19, κ-antigen and λ-antigen using previously determined optimum dilutions of Alexa conjugated secondary antibodies (fig. 9C). Additionally, staining was performed using 1:100 Cy5 rather than 1:400 A647 for a direct comparison between the two fluorophores when used alongside the optimal dilutions of the other Alexa fluorophores (fig. 9B). A stain was also performed using the original secondary antibody panel for direct comparison (fig. 9A).

As expected, when both optimum concentrations of antibody sets were directly compared, A488 and A568 were brighter than FITC and TRITC respectively (fig. 9). 1:100 Cy5 was brighter than A647 overall, and the contrast had to be adjusted for A647 to be observable. To evaluate the effectiveness of the staining, the levels of CD19 and κ-positive cells were compared against CD19 and λ-positive cells. The values obtained were generally consistent across all three staining methods, and two-tailed T tests performed between each secondary antibody set indicated no statistically significant differences (A vs. B P = 0.69, A vs. C P = 0.97, B vs. C P= 0.54, fig. 9 D/E). The average κ/λ ratio across all stains was 1.65 (SEM =

±0.81, range = 1.3-1.98, fig.9 E) suggesting that all of the secondaries used were accurately representing the B cell κ/λ ratio present in the sample.

The evidence that these concentrations of A488 and A568 were more effective than the optimal concentrations of the corresponding original fluorophores was fairly conclusive, but Cy5 was observed to be brighter than A647 at their corresponding optimal dilutions. However, upon adjustment of linear contrast, the signal strength of A647 could be made more pronounced, and making the same adjustments to images of secondary only controls made sure that no autofluorescence or background staining was also being emphasised. When this was performed, similar staining patterns were observed using each fluorophore (Fig 9 D, E), implying that A647 still produced adequate staining brightness for the resolution of CD19 positive cells, albeit not as bright as Cy5. Thus, the optimum secondaries were determined as follows:

Corresponding primary antibody antigen specificity	**Optimum original secondary conjugate**	**Optimum Alexa secondary conjugate**
κ	1:100 FITC	1:200 A488
λ	1:50 TRITC	1:50 A568
CD19	1:100 Cy5	1:400 A647

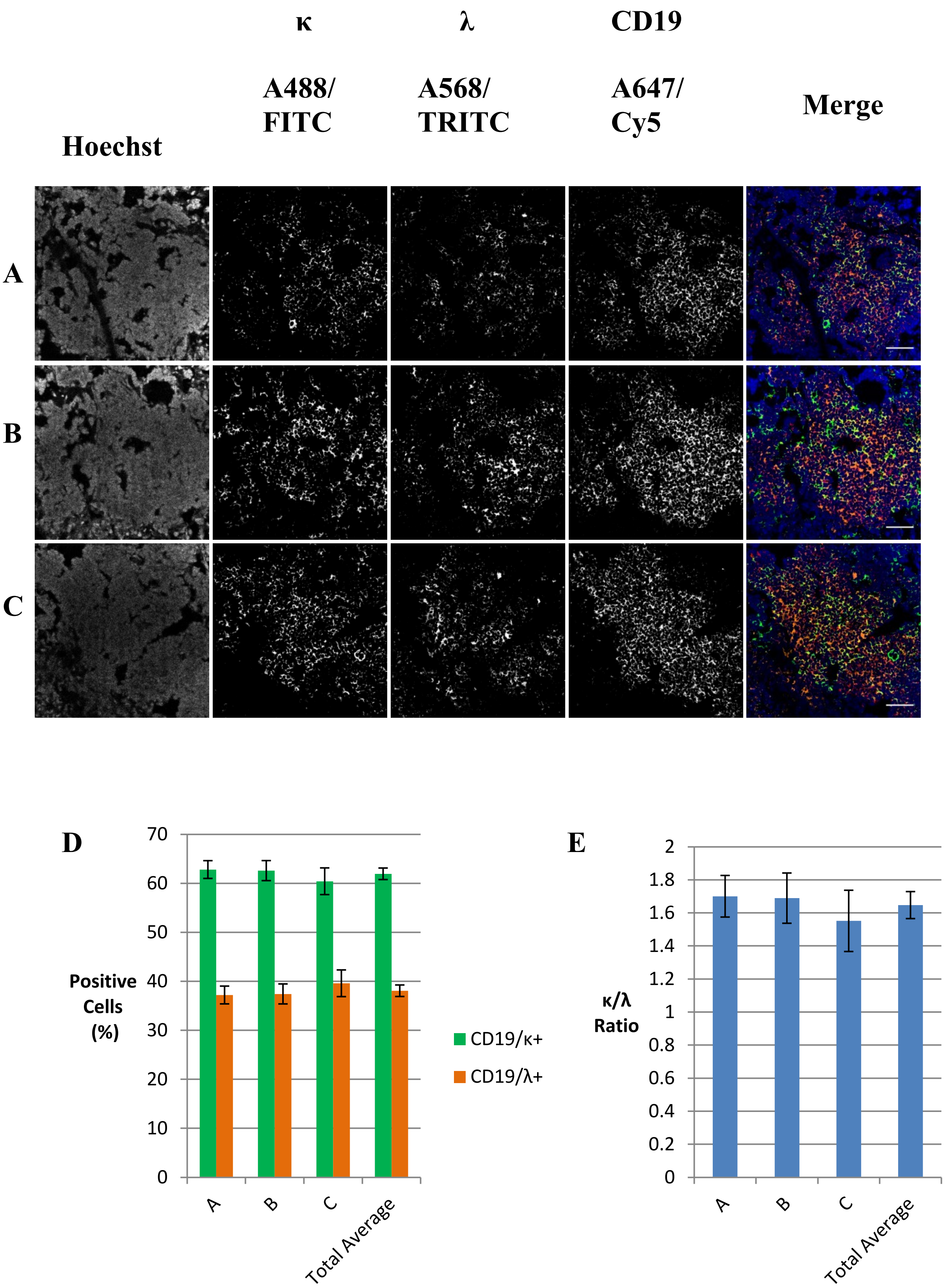

Figure 9 – Optimised staining panels. **A**. 1:100 FITC, 1:50 TRITC, 1:100 Cy5. **B**. 1:200 A488, 1:50 A568, 1:100 Cy5. **C.** 1:200 A488, 1:50 A568, 1:400 A647. Images were obtained at 40x magnification and scale bars represent 50 µm. **D**. Relative levels of CD19 and κ-light chain positive cells vs. CD19 and λ-light chain positive cells across the three differing secondary antibody panels. **E**. Relative κ/λ Ratios of CD19 positive cells across the three differing secondary antibody panels. For both graphs, three images were analysed per antibody panel for a total of nine images for the total average, and error bars represent the standard error of the mean. Pseudocolours – Blue = nuclear counterstain, Green = κ /FITC or A488, orange = λ /TRITC or A568, red = CD19/Cy5 or A647.

4.0 Discussion

This study has developed and optimised a method for the simultaneous visualisation of CD19, κ and λ immunoglobulin light chain antigens in reactive lymph node cryosections using a combination of immunofluorescence and confocal laser scanning microscopy. The images obtainable with this method are of high quality and resolution, and allow for the visualisation of three specific biomarkers alongside a nuclear counterstain. The study developed on preliminary experiments that used older generation fluorophores and optimised the method for use with new generation Alexa fluorophores. The increase in photostability, and in the case of A488 and A568 signal brightness, gained from using these fluorophores increases the viability of the staining method to imaging via CLSM (Berlier et al., 2003; Panchuk-Voloshina et al., 1999; Robertson et al., 2008), as well as increases the clinical applicability of the method due to greater re-imaging and long-term storage capabilities (Robertson et al., 2008). The method also provides superior multiple marker imaging capability in comparison to widely used enzyme-based immunohistochemical methods (Robertson et al., 2008).

4.1 The establishment of effective tissues and mounting methods

This study originally intended to carry out the optimisation experiments on healthy splenic tissue rather than reactive lymph node. However, staining was of poor quality and sparse. This could have been due to antigen epitope deterioration, but cryosectioning and acetone fixation generally preserves antigens to a high standard (Hofman, 2009; Ripper et al., 2008), and reactive lymph nodes were processed in the same manner. Alternatively, the tissue sections may simply have been low in B-lymphocyte rich regions. Regardless of the cause, this setback further highlighted the importance of good quality tissue sections for imaging.

In addition, locating these apparently sparse regions of tissue that should be rich in B lymphocytes, such as primary and secondary follicles (Cesta, 2006), was difficult due to some technical aspects of the microscope used for the study. The microscope was equipped with a 10x air immersion objective, unlike the 40x objective which was oil immersion, causing a number of problems. Firstly, the light collection capability of this objective was sub-standard in comparison with the oil immersion objective, causing difficulty in resolving any fluorescent signal at 10x magnification. Secondly, as the 10x objective was air immersion and the 40x objective was oil immersion, the differing refractive indices of the two mediums meant that it would have been difficult to optimise multiple microscope settings and antibody dilutions that would produce high quality images for each objective type. All in all, the splenic tissue was not conducible to experiments where high levels of staining were required to evaluate the effectiveness of secondary antibody dilutions and microscope settings. The reactive lymph node samples produced high quality staining of CD19, κ and/or λ light chain antigen positive cell regions which were abundant throughout the tissue, allowing for relatively simple location at 40x magnification. A higher number of images per tissue section could also be obtained. Future experiments could involve both 10x and 40x oil immersion objectives, avoiding these problems, as 10x images are also highly useful for obtaining a more general overview of the distribution of biomarkers within the tissue.

The Hoechst nuclear counterstaining dye was relatively faint, but mounting slides using VECTAShield with DAPI resulted in Cy5 signal amelioration. VECTAShield was initially an attractive option because it was more time effective - the inclusion of DAPI within the mounting medium removed the necessity for a counterstaining step. The loss of Cy5 signal was unexpected, but may have been caused by the fact that VECTAShield contains the antifade compound p-phenylenediamine (PPD). As stated by the VECTAShield data sheet, PPD cleaves the cyanine molecules in Cy2 fluorophores and thus ameliorates the fluorescent signal, which may also have occurred with the Cy5 fluorophores used in this study. Any future studies featuring cyanine dyes should therefore avoid mounting mediums that contain

PPD. Overall, the low signal strength of the Hoechst counterstain was a minor inconvenience rather than a major problem because the laser power and PMT gain could be increased in compensation. This did result in some tissue autofluorescence in the Hoechst/DAPI channel, but not sufficiently to hinder the interpretation of the images.

4.2 The value of experimental controls

The single colour control experiments were essential to assume that any signal observed in a given emission collection channel was not caused by spectral bleedthrough across channels. In addition, performing secondary only stains alongside all experiments allowed for the determination of the concentration at which non-specific fluorophore binding was minimal while true staining was strong. Together, these controls greatly increased the viability of the images and allowed for the determination of optimum antibody dilutions and microscope settings.

Although the controls employed in this study were deemed adequate, an antibody isotype subclass control may also have granted even further confidence in the images obtained. Antibody isotype subclass controls confirm that the secondary antibodies are exclusively recognising the primary antibody isotype subclass intended. This is achieved by sequentially replacing primary antibodies with the same concentration of a nonspecific isotype control antibody of the same species and isotype subclass (Robertson et al., 2008). However, this was deemed as unnecessary for this study, mainly because each individual fluorescent secondary used produced staining patterns against their corresponding anti- CD19, κ or λ primary antibodies as would be expected for these antigens.

4.3 Optimum antibody dilutions

Based on signal/noise observations, it was eventually established that the optimum dilutions of Alexa conjugated secondary antibodies were 1:200 for A488, 1:50 for A568 and 1:400 for

A647. However, 1:100 Cy5 was qualitatively observed to produce better signal than 1:400 A647, the highest concentration determined to be viable due to high background signal. Nevertheless, it was decided that A647 was a superior choice to Cy5 for a number of reasons:

a) A647 signal strength could be amplified by adjusting the linear contrast within ranges that did not exaggerate background staining levels, producing statistically indifferent CD19 staining patterns to Cy5.

b) Cy5 was shown to destabilise when mounted with VECTAShield, meaning that it is less adaptable to methodological variations.

c) Like Alexa488 compared with FITC and Alexa568 compared with TRITC, Alexa647 has been shown to be more photostable in comparison to Cy5, and is therefore more conducive to the high intensity laser excitation methods of CLSM and sample storage and reimaging capability (Berlier et al., 2003; Panchuk-Voloshina et al., 1999; Robertson et al., 2008).

However, while Alexa fluorophores are reportedly more photostable, it may be beneficial for future experiments to quantify the photostability of the dyes when used in this histological context for staining immunological tissues. For example, Alexa-stained tissues could be exposed to set laser intensities for set time periods, and the change in signal intensity quantified and compared with those of the original dye-conjugated secondaries exposed to the same conditions. Fluorophore stability during storage of immunological tissue cryosections could also be assessed by imaging immediately after staining and mounting and comparing fluorescence signal strength after storage for set time periods, as this is likely to differ between tissue processing methods and tissue types.

Overall, images obtained from these optimum dilutions of Alexa conjugated secondaries were qualitatively determined as sharp and showing a good signal/noise ratio for each fluorophore.

Cells that were CD19 positive were also either κ or λ-light chain positive, and there was very little colocalisation of κ-antigen and λ-antigen signal, as would be expected (Takeda et al., 1993). The use of Alexa fluorophores is also beneficial from an economic perspective - while Alexa conjugated secondary antibodies can be slightly more expensive than older generation fluorophore conjugates, this study demonstrates that higher dilutions of Alexa secondaries can be used in comparison with the original secondaries. In the case of A488 and A568, a better signal/noise ratio was observed, and although the final working dilution of A568 was 1:50, only a very slight drop in staining quality was observed in dilutions up to 1:200 suggesting that A568 could be reliably used at these lower dilutions. Had there been no time constraints, certain parameters of the staining protocol could also have been adjusted to obtain the best possible signal/noise ratios, such as the incubation times of the primary and secondary antibodies, or adding gentle movement/vibration to the incubation steps, which has been shown to improve signal/noise ratio in other IF applications (Jacobsen and Staines, 2004). It was however relatively simple to distinguish and remove background noise from true staining, and the incubation methods used were therefore adequate for the purposes of this study.

Quantitative analysis revealed that the ratio of CD19/κ-positive cells against CD19/λ-positive cells was highly similar for all secondary antibodies assessed. This was an important observation, as firstly it indicated that the staining patterns observed were likely to represent the true B-lymphocyte κ/λ light chain ratios of the tissue. Secondly, the fact that all combinations of fluorophores generated the same pattern of staining was further evidence that all secondaries were binding to the correct primary antibody isotype subclasses. In addition, the observed average κ/λ ratio of 1.65 was fairly normal for a non-diseased reactive lymph node - one study into the κ/λ ratio of B-lymphocytes within reactive lymph nodes recorded an average κ/λ ratio of 1.78 in germinal centre cells and 1.56 in mantle cells (Reichard et al., 2003). Although the markers imaged in this study could not distinguish germinal centre cells from mantle cells, both values are similar, further implying that the staining was correct. If more time had been available, flow cytometric analysis could have been performed on the tissue samples used to further support these observations. Additionally, although the standard error values were relatively small and staining characteristics were reproducible throughout the study, the quantification experiments could have been repeated for increased confidence in the results obtained.

4.4 Potential future applications of IF multilabelling and CLSM imaging for immunological tissues

This study has optimised a relatively simple method of simultaneous spatial resolution of multiple antigens within lymphatic tissue. Not only is this tool valuable for research into the molecular mechanisms of normal immunological processes as well as disease, but it could potentially be applied in a clinical setting to diagnose and establish prognoses and suitable treatment courses of cancers based on their individual molecular profiles determined through immunophenotyping. In comparison to flow cytometry, CLSM immunophenotyping is lower throughput, but information concerning the spatial distribution of multiple markers within the tissue is obtainable within two or three dimensions, which is not possible with flow cytometry (Demandolx and Davoust, 1997; Robertson et al., 2008; Takaku et al., 2010).

The main reason for using primary antibodies specific to CD19, κ and λ antigens was that such staining should follow an expected pattern and the primary antibodies were known to be effective. However, the simultaneous imaging of these markers in a lymph node cryosection may still assist in the diagnosis of many B cell neoplasms. An abnormal κ/λ light chain ratio that is heavily skewed towards one subtype is often indicative of mature B-cell neoplasms, because this indicates the presence of a monoclonal population of cells (Reichard et al., 2003;

Stahlberg et al., 2003). However, aside from these direct benefits, the true potential of the method will be realised as it is optimised for visualising more antigens within both healthy and diseased tissues.

4.5 The potential of CLSM imaging in diagnostic and prognostic immunohistopathology

Potential applications of the method include clinical immunophenotyping of lymphomas and lymphatic leukaemias for diagnostic and prognostic reasons, as well as for personalised treatment options. For example, B-cell chronic lymphocytic leukaemia (B-CLL) tumour cells resemble small, mature, monoclonal B-lymphocytes. Distinct tumour biomarkers include a high expression of CD5 and CD23, and forms that express CD38 and/or CD49d correlate with an aggressive disease course and a poor prognosis (Del Poeta et al., 2001; Hamblin et al., 1999; Hayden et al., 2012; Pittner et al., 2005). Thus, using this IF imaging method against these antigens, diagnostic and prognostic markers could theoretically be identified simultaneously, and treatment courses could be planned based on the outcome of such analysis. Non-Hodgkin lymphomas are also excellent disease candidates that may benefit from this method. Many different forms of lymphoma exist, all of which have different disease courses, prognoses and treatment regimens. The histological features of lymphomas are well defined, but many different forms are histomorphologically similar, as well as appearing similar to reactive rather than diseased lymph node tissue. Thus, other such markers that may be beneficial to image include CD20, as 95% of malignant lymphomas as well as B-CLL express CD20 (Sathiya and Muthuchelian, 2009). Another example includes CD134, a marker that can differentiate similar T-cell lymphoma types, as tumours consisting of activated CD41 T cells express this marker while other forms such as small T cell lymphomas do not, aiding in the subclassification of peripheral T-cell lymphomas (Jones et al., 1999).

The markers discussed in this section are but a few examples, and theoretically any combination of cell surface markers can be imaged simultaneously to diagnose specific variants of many immunological disorders. Furthermore, as well as the identification of such markers, the method itself could also be very important in the study of the molecular mechanisms that constitute the underlying cause of such markers featuring in disease.

4.6 The potential of CLSM imaging in cancer research

The method could also greatly benefit biomedical research into lymphomas and lymphatic leukaemias, through investigating the molecular mechanisms of cancers and thereby developing novel, personalised and targeted therapies. Such therapies target the specific molecular processes that cause oncogenicity, and are therefore highly effective at tumour killing whilst less toxic to non-neoplastic cells in comparison to methods such as traditional radiotherapy and chemotherapy. Cancer cells survive and proliferate due to specific mutations to oncogenes and/or tumour suppressor genes, which result in disrupted regulatory networks, aberrant responses to stress signals, and signals from the microenvironment. Resulting effects may include deregulated cell cycle progression and hence increased proliferation, a lack of response to DNA damage signals and further accumulation of mutations, and defective apoptotic responses and thus increased tumour survival (Sawyers, 2004).

For several lymphatic leukaemias and lymphomas, the focus in developing such therapies has recently been on targeting the tumour microenvironment, or niche. B-CLL, for example, has no outright cure, and current therapies induce transitory remission by periodically reducing the load of peripherally circulating quiescent tumour cells (Chiorazzi et al., 2005; Damle et al., 1999). B-CLL cells that are present in tumour microenvironments within bone marrow and lymph node pseudofollicles are thought to be major causes of relapse due to their resistance to treatments and subsequent ability to restore tumour load levels, and therefore specific therapies are required for targeting these cells within the tumour microenvironment (Hayden et al., 2012).

As is true for normal B-cell development, $CD4^+$ T helper cell interaction is thought to be heavily involved in B-CLL, for providing protection against apoptotic signals and promoting cell survival through molecular processes such as CD40-CD40 ligand interactions (Ghia et al., 2002; Hayden et al., 2012). Stromal cell interaction could also be important, preventing apoptosis through modulation of the PI3K/PTEN signalling cascade (Shehata et al., 2010) and molecules such as VCAM-1, the cell adhesion molecule, and VLA-4 are thought to play large roles in the trafficking of B-CLL tumour cells to these microenvironments (Hartmann et al., 2009). The CD38 molecule is also thought to be an important mediator of such processes, which correlates with the fact that it is a negative prognostic indicator for B-CLL (Deaglio et al., 2006). These examples are but a few of the many cell types and molecules thought to contribute to this highly complex niche system, and similar mechanisms of niche involvement are thought to be highly important in many other lymphatic diseases, such as follicular lymphoma (Pangault et al., 2010). These examples therefore underlines the value of an imaging method that can simultaneously visualise multiple markers and provide information on the complex network of interactions of such cells and molecules, with the eventual goal of producing specific therapies that may target such molecular processes.

To analyse these inferred specific molecular interactions in more detail, the imaging method could also be further developed for novel experimental applications such as Förster Resonance Energy Transfer (FRET). This requires the use of two fluorophores with overlapping emission and excitation spectra, so a photon emitted from an excited donor fluorophore can subsequently excite an acceptor fluorophore to emit a photon (Jiang et al., 2008; Li et al., 2000). Fluorophore crosstalk is usually undesired for multiple marker imaging, but in the case of FRET it can signify molecular interactions. The sample is illuminated with the excitation wavelength of the donor fluorophore only, and if photons emitted from the acceptor fluorophore are detected, FRET has occurred. The detection of this quantum physical phenomenon can indicate molecular interactions because the energy transfer can only occur within close molecular proximity (<100 Å) (Li et al, 2000).

4.7 Conclusions and future perspectives

The examples of potential applications of this multiple marker imaging method via IF and CLSM presented in this section are but a small fraction of the overall potential of this method in biology and medicine. Future experiments should broaden the range of markers that can be imaged by optimising staining protocols for many biomarkers that have significant roles in immunology and immunopathology. Further continuations of this study could also involve optimisation for many different tissues, immunological or otherwise, as this method offers much for many histological applications other than immunology and immunopathology. Furthermore, future studies could also look to broaden the number of markers that can be simultaneously imaged, as has been previously accomplished by novel immunolabelling methods, although this can be limited by the availability of spectrally distinct fluorophores (Ma et al., 2006). Novel image analysis methods have been employed in an attempt to work around this, however such as colour addition (Ma et al., 2006; Ma et al., 2007). It may also be beneficial to future optimisation studies to devise quantification methods for signal/noise ratio rather than qualitative visual analysis as performed in this study, such as calculating the signal/noise ratio by comparing average gray levels of stained areas against background areas, or direct comparisons of pixel intensity values (Jacobsen and Staines, 2004).

By optimising staining and imaging methods for the visualisation of CD19, κ and λ antigen in reactive lymph node tissue, this study has provided a basis upon which to further develop and refine IF imaging via CLSM in immunological tissues as well as others, so that it may be applied to many diseases in both clinical histopathology and biomedical research.

List of References

Arzt, J., Gregg, D.A., Clavijo, A., et al. (2009) Optimization of immunohistochemical and fluorescent antibody techniques for localization of Foot-and-mouth disease virus in animal tissues. **Journal of Veterinary Diagnostic Investigation,** 21 (6): 779-792.

Bain, V.G. and Bain, G.O. (1985) Lymphocyte Populations with Abnormal Kappa-Lambda Ratios in Reactive Lymphoid Hyperplasia. **Journal of surgical oncology,** 29 (4): 227-230.

Belov, L., Zhou, J. and Christopherson, R.I. (2011) Cell Surface Markers in Colorectal Cancer Prognosis. **International Journal of Molecular Sciences,** 12 (1): 78-113.

Benchaib, M., Delorme, R., Pluvinage, M., et al. (1996) Evaluation of five green fluorescence-emitting streptavidin-conjugated fluorochromes for use in immunofluorescence microscopy. **Histochemistry and cell biology,** 106 (2): 253-256.

Berlier, J.E., Rothe, A., Buller, G., et al. (2003) Quantitative comparison of long-wavelength Alexa Fluor dyes to Cy dyes: Fluorescence of the dyes and their bioconjugates. **Journal of Histochemistry & Cytochemistry,** 51 (12): 1699-1712.

Brelje, T.C., Wessendorf, M.W. and Sorenson, R.L. (2002) Multicolor laser scanning confocal immunofluorescence microscopy: Practical application and limitations. **Cell Biological Applications of Confocal Microscopy, Second Edition,** 70 165-244.

Brown, C.M. (2007) Fluorescence microscopy - avoiding the pitfalls. **Journal of cell science,** 120 (10): 1703-1705.

Buchwalow, I.B., Minin, E.A. and Boecker, W. (2005) A multicolor fluorescence immunostaining technique for simultaneous antigen targeting. **Acta Histochemica,** 107 (2): 143-148.

Cesta, M.F. (2006) Normal structure, function, and histology of the spleen. **Toxicologic pathology,** 34 (5): 455-465.

Chin, P.T.K., Beekman, C.A.C., Buckle, T., et al. (2012) Multispectral visualization of surgical safety-margins using fluorescent marker seeds. **American Journal of Nuclear Medicine and Molecular Imaging,** 2 (2): 151-162.

Chiorazzi, N., Rai, K. and Ferrarini, M. (2005) Mechanisms of disease: Chronic lymphocytic leukemia. **New England Journal of Medicine,** 352 (8): 804-815.

Coons, A.H., Creech, H.J., Jones, R.N., et al. (1942) The demonstration of pneumococcal antigen in tissues by the use of fluorescent antibody. **Journal of Immunology,** 45 (3): 159-170.

Damle, R., Wasil, T., Fais, F., et al. (1999) Ig V gene mutation status and CD38 expression as novel prognostic indicators in chronic lymphocytic leukemia. **Blood,** 94 (6): 1840-1847.

Deaglio, S., Vaisitti, T., Aydin, S., et al. (2006) In-tandem insight from basic science combined with clinical research: CD38 as both marker and key component of the pathogenetic network underlying chronic lymphocytic leukemia. **Blood,** 108 (4): 1135-1144.

Del Nagro, C., Otero, D., Anzelon, A., et al. (2005) CD19 function in central and peripheral B-cell development. **Immunologic research,** 31 (2): 119-131.

Del Poeta, G., Maurillo, L., Venditti, A., et al. (2001) Clinical significance of CD38 expression in chronic lymphocytic leukemia. **Blood,** 98 (9): 2633-2639.

Demandolx, D. and Davoust, J. (1997) Multicolour analysis and local image correlation in confocal microscopy. **Journal of Microscopy-Oxford,** 185 21-36.

Eggeling, C., Widengren, J., Rigler, R., et al. (1998) Photobleaching of fluorescent dyes under conditions used for single-molecule detection: Evidence of two-step photolysis. **Analytical Chemistry,** 70 (13): 2651-2659.

Entwistle, A. and Noble, M. (1992) The use of Lucifer Yellow, Bodipy, Fitc, Tritc, Ritc and Texas Red for Dual Immunofluorescence Visualized with a Confocal Scanning Laser Microscope. **Journal of Microscopy-Oxford,** 168 219-238.

Ermert, L., Hocke, A.C., Duncker, H.R., et al. (2001) Comparison of different detection methods in quantitative microdensitometry. **American Journal of Pathology,** 158 (2): 407-417.

Ferri, G.L., Gaudio, R.M., Castello, I.F., et al. (1997) Quadruple immunofluorescence: A direct visualization method. **Journal of Histochemistry & Cytochemistry,** 45 (2): 155-158.

Finkpuches, R., Hofmannwellenhof, R., Smolle, J., et al. (1995) Confocal Laser-Scanning Microscopy - a New Optical Microscopic Technique for Applications in Pathology and Dermatology. **Journal of cutaneous pathology,** 22 (3): 252-259.

Ghia, P., Strola, G., Granziero, L., et al. (2002) Chronic lymphocytic leukemia B cells are endowed with the capacity to attract CD4(+), CD40L(+) T cells by producing CCL22. **European journal of immunology,** 32 (5): 1403-1413.

Hamblin, T.J., Davis, Z., Gardiner, A., et al. (1999) Unmutated Ig V-H genes are associated with a more aggressive form of chronic lymphocytic leukemia. **Blood,** 94 (6): 1848-1854.

Hartmann, T.N., Grabovsky, V., Wang, W., et al. (2009) Circulating B-Cell Chronic Lymphocytic Leukemia Cells Display Impaired Migration to Lymph Nodes and Bone Marrow. **Cancer research,** 69 (7): 3121-3130.

Hayden, R.E., Pratt, G., Roberts, C., et al. (2012) Treatment of chronic lymphocytic leukemia requires targeting of the protective lymph node environment with novel therapeutic approaches. **Leukemia & lymphoma,** 53 (4): 537-549.

Hofman, F. (2009) **Immunohistochemistry of Frozen Tissue Sections.** [Online]. Available from:

http://molecularinnovations.helpserve.com/index.php?_m=knowledgebase&_a=viewarticle&kbarticleid=13 [Accessed 07/15 2012].

Jacobsen, K.X. and Staines, W.A. (2004) Vibration enhancement of slide-mounted immunofluorescence staining. **Journal of neuroscience methods,** 137 (1): 71-77.

Jiang, T., Xing, B. and Rao, J. (2008) Recent Developments of Biological Reporter Technology for Detecting Gene Expression. **Biotechnology and Genetic Engineering Reviews, Vol 25,** 25 41-75.

Jones, D., Fletcher, C.D.M., Pulford, K., et al. (1999) The T-cell activation markers CD30 and OX40/CD134 are expressed in nonoverlapping subsets of peripheral T-cell lymphoma. **Blood,** 93 (10): 3487-3493.

Key, M. (2009) "Chapter 9: Immunohistochemical Staining Methods" In Kumar, G.L. and Rudbeck, L. (eds.) **IHC Staining Methods** 5th ed. Carpinteria, California, USA: Dako North America. pp. 57-60.

Krenacs, T., Krenacs, L., Bozoky, B., et al. (1990) Double and Triple Immunocytochemical Labeling at the Light-Microscope Level in Histopathology. **Histochemical Journal,** 22 (10): 530-536.

Kupper, H. and Storz, H. (1986) Double Staining Technique using a Combination of Indirect and Direct Immunofluorescence with Monoclonal-Antibodies. **Acta Histochemica,** 78 (2): 185-188.

Li, H.Y., Ng, E.K.O., Lee, S.M.Y., et al. (2000) Protein-protein interaction of FHL3 with FHL2 and visualization of their interaction by green fluorescent proteins (GFP) two-fusion fluorescence resonance energy transfer (FRET). **Journal of cellular biochemistry,** 80 (3): 293-303.

Li, J., Lenferink, A.E.G., Deng, Y., et al. (2010) Identification of high-quality cancer prognostic markers and metastasis network modules. **Nature Communications,** 1 34.

Ma, B., He, F., Jablonska, J., et al. (2007) Six-color segmentation of multicolor images in the infection studies of Listeria monocytogenes. **Microscopy research and technique,** 70 (2): 171-178.

Ma, B., Winketbach, S., Lindenmaier, W., et al. (2006) Six-colour fluorescent imaging of lymphoid tissue based on colour addition theory. **Acta Histochemica,** 108 (4): 243-257.

Mahon, M. (2011) **Histology.info.** [Online]. Available from: http://histology.info/ [Accessed 6/15 2012].

Mujumdar, R.B., Ernst, L.A., Mujumdar, S.R., et al. (1993) Cyanine Dye Labeling Reagents - Sulfoindocyanine Succinimidyl Esters. **Bioconjugate chemistry,** 4 (2): 105-111.

Paddock, S.W. (2000) Principles and practices of laser scanning confocal microscopy. **Molecular biotechnology,** 16 (2): 127-149.

Panchuk-Voloshina, N., Haugland, R.P., Bishop-Stewart, J., et al. (1999) Alexa dyes, a series of new fluorescent dyes that yield exceptionally bright, photostable conjugates. **Journal of Histochemistry & Cytochemistry,** 47 (9): 1179-1188.

Pangault, C., Ame-Thomas, P., Ruminy, P., et al. (2010) Follicular lymphoma cell niche: identification of a preeminent IL-4-dependent T-FH-B cell axis. **Leukemia,** 24 (12): 2080-2089.

Papaxoinis, K., Patsouris, E., Kittas, C., et al. (2007) Insulinlike growth factor I receptor and estrogen receptor beta expressions are inversely correlated in colorectal neoplasms and affected by the insulin resistance syndrome. **Human pathology,** 38 (7): 1037-1046.

Pittner, B.T., Shanafelt, T.D., Kay, N.E., et al. (2005) CD38 expression levels in chronic lymphocytic leukemia B cells are associated with activation marker expression and differential responses to interferon stimulation. **Leukemia,** 19 (12): 2264-2272.

Qui Wen-sheng, Yue Lu, Ding Ai-ping, et al. (2009) Co-expression of ER-beta and HER2 associated with poorer prognosis in primary breast cancer. **Clinical and Investigative Medicine,** 32 (3): E250-E260.

Ravdin, P. and Axelrod, D. (1977) Fluorescent tetramethyl rhodamine derivatives of alpha-bungarotoxin: preparation, separation, and characterization. **Analytical Biochemistry,** 80 (2): 585-592.

Reichard, K.K., McKenna, R.W. and Kroft, S.H. (2003) Comparative analysis of light chain expression in germinal center cells and mantle cells of reactive lymphoid tissues - A four-color flow cytometric study. **American Journal of Clinical Pathology,** 119 (1): 130-136.

Renshaw, S. (2005) "**Chapter 4: Immunochemical Staining Techniques**" In Renshaw, S. (ed.) **Immunohistochemistry: Methods Express Series** 1st ed. Bloxham, UK: Scion Publishing Ltd. pp. 45-96.

Rigacci, L., Alterini, R., Bernabei, P., et al. (2000) Multispectral imaging autofluorescence microscopy for the analysis of lymph-node tissues. **Photochemistry and photobiology,** 71 (6): 737-742.

Ripper, D., Schwarz, H. and Stierhof, Y. (2008) Cryo-section immunolabelling of difficult to preserve specimens: advantages of cryofixation, freeze-substitution and rehydration. **Biology of the Cell,** 100 (2): 109-123.

Robertson, D., Savage, K., Reis-Filho, J.S., et al. (2008) Multiple immunofluorescence labelling of formalin-fixed paraffin-embedded (FFPE) tissue. **Bmc Cell Biology,** 9 13.

Sandison, D.R. and Webb, W.W. (1994) Background Rejection and Signal-To-Noise Optimization in Confocal and Alternative Fluorescence Microscopes. **Applied Optics,** 33 (4): 603-615.

Sathiya, M. and Muthuchelian, K. (2009) Significance of Immunologic Markers in the Diagnosis of Lymphoma. **Academic Journal of Cancer Research,** 2 (1): 40-50.

Savage, K., Leung, S., Todd, S.K., et al. (2008) Distribution and significance of caveolin 2 expression in normal breast and invasive breast cancer: an immunofluorescence and immunohistochemical analysis. **Breast cancer research and treatment,** 110 (2): 245-256.

Sawyers, C. (2004) Targeted cancer therapy. **Nature,** 432 (7015): 294-297.

Semwogerere, D. and Weeks, E.R. (2005) "Confocal Microscopy" In Bowlin, G.L. and Wnek, G.E. (eds.) **Encyclopedia of Biomaterials and Biomedical Engineering** 1st ed. USA: Taylor and Francis. pp. 1-10.

Shehata, M., Schnabl, S., Demirtas, D., et al. (2010) Reconstitution of PTEN activity by CK2 inhibitors and interference with the PI3-K/Akt cascade counteract the antiapoptotic effect of human stromal cells in chronic lymphocytic leukemia. **Blood,** 116 (14): 2513-2521.

Sheppard, C.J.R. (1989) Axial Resolution of Confocal Fluorescence Microscopy. **Journal of Microscopy-Oxford,** 154 237-241.

Signore, M., Cerio, A.M., Boe, A., et al. (2012) Identity and ranking of colonic mesenchymal stromal cells. **Journal of cellular physiology,** 227 (9): 3291-3300.

Stahlberg, A., Aman, P., Ridell, B., et al. (2003) Quantitative real-time PCR method for detection of B-lymphocyte monoclonality by comparison of kappa and lambda immunoglobulin light chain expression. **Clinical chemistry,** 49 (1): 51-59.

Takaku, T., Malide, D., Chen, J., et al. (2010) Hematopoiesis in 3 dimensions: human and murine bone marrow architecture visualized by confocal microscopy. **Blood,** 116 (15): E41-E55.

Takeda, S., Zou, Y.R., Bluethmann, H., et al. (1993) Deletion of the immunoglobulin kappa chain intron enhancer abolishes kappa chain gene rearrangement in cis but not lambda chain gene rearrangement in trans. **The EMBO journal,** 12 (6): 2329-2336.

Thiel, E. (1985) Cell-Surface Markers in Leukemia - Biological and Clinical Correlations. **Crc Critical Reviews in Oncology/hematology,** 2 (3): 209-260.

Troxell, M.L., Weintraub, L.A., Higgins, J.P., et al. (2006) Comparison of C4d immunostaining methods in renal allograft biopsies. **Clinical Journal of the American Society of Nephrology,** 1 (3): 583-591.

Valdesaguilera, O. and Neckers, D.C. (1989) Aggregation Phenomena in Xanthene Dyes. **Accounts of Chemical Research,** 22 (5): 171-177.

Vanderloos, C.M., Das, P.K., Vandenoord, J.J., et al. (1989) Multiple Immunoenzyme Staining Techniques - use of Fluoresceinated, Biotinylated and Unlabeled Monoclonal-Antibodies. **Journal of immunological methods,** 117 (1): 45-52.

Vanderloos, C.M., Vandenoord, J.J., Das, P.K., et al. (1988) Use of Commercially Available Monoclonal-Antibodies for Immunoenzyme Double Staining. **Histochemical Journal,** 20 (8): 409-413.

Vanderloos, C.M. (2008) Multiple immunoenzyme staining: Methods and visualizations for the observation with spectral imaging. **Journal of Histochemistry & Cytochemistry,** 56 (4): 313-328.

Vandervalk, P. and Meijer, C.J.L.M. (1987) The Histology of Reactive Lymph-Nodes. **American Journal of Surgical Pathology,** 11 (11): 866-882.

Willard-Mack, C.L. (2006) Normal structure, function, and histology of lymph nodes. **Toxicologic pathology,** 34 (5): 409-424.

Appendix

Fluorophore	**Molecular Weight**	**Absorption/Emission Maxima (nm)**	**Extinction Coefficient (L mol^{-1} cm^{-1})**	**Quantum Yield**
FITC	389	494/518	78,000	~0.9*
TRITC	479	541/572	100,000	~0.35*
Cy5	792	650/670	250,000†	0.27†
Alexa488	643	495/519	71,000	0.92
Alexa568	792	578/603	91,300	0.69
Alexa647	~1300	650/665	237,000	0.33

Table S1 - Relevant spectral information of all fluorophores used in the study. Alexa fluorophore information was obtained from Invitrogen product data sheets, and other information was obtained from Thermo Scientific product data sheets unless otherwise stated. These values are provided for guidance only. It is important to note that the quantum yield of fluorophores can be reduced upon conjugation to other molecules due to fluorophore quenching or pH conditions, although Alexa fluorophores are less susceptible to this compared with original fluorophores as explained in the text.

These measurements were obtained from dye molecules in aqueous solutions (PBS). Alexa measurements were obtained on free succinimidyl ester derivatives in PBS.

* = values obtained from Chin et al., 2012.

† = values obtained from Mujumdar et al., 1993.